A study and interpretation of the distribution and kinematics of the 2001 Taupō Fault Belt seismic swarm using relative relocation techniques

By

Ross Findlay D'estampes McGregor

A thesis submitted to Victoria University of Wellington
in fulfilment of the requirements for the degree of
Master of Science in Geology

Te Herenga Waka – Victoria University of Wellington

2022

Abstract

The Taupō Volcanic Zone (TVZ) is the southern extent of the Tonga-Kermadec volcanic arc, forming a rifted arc due to its interaction with the nearby Hikurangi Subduction Zone. The TVZ aligns closely with the Taupō Rift, with the two structures accommodating extension in the region via magmatic and tectonic processes. Rates of seismicity are high in this area, especially around Taupō Volcano in the central TVZ. A swarm of earthquakes occurring between January and June 2001 contrasts with other periods of increased seismicity, occurring slightly north of the volcano within the Taupō Fault Belt. We have analysed this swarm of earthquakes to investigate potential interaction between the tectonic and magmatic systems at Taupō.

We obtained data from two temporary seismic arrays deployed at the time of the swarm and processed the data using non-linear location, matched-filter detection and differential relocation to yield over 2000 more earthquakes than initially detected by GeoNet. The relocated events indicated that earthquakes occurring within the fault belt formed vertical clusters near small, unidentified faults. Prior to seismicity within the Taupō Fault Belt, a large earthquake cluster was located beneath Lake Taupō's Western Bay, previously thought to be aseismic. Focal mechanisms calculated for six of the eight largest magnitude earthquakes within the swarm are consistent with a rotation of the maximum compressive stress axes to horizontal during the swarm.

We interpret the earthquakes detected beneath the Western Bay as signalling unrest from an intruding, possibly mafic, magma body, such as have been identified at numerous other calderas. Fluids and increased horizontal stress from this intrusion triggered the resulting seismicity in the Taupō Fault Belt, which display vertical clustering and small-scale propagation to support this. Increased horizontal pressure from the intrusion rotated the axis of maximum compressive stress, indicated by strike-slip focal mechanisms and mirroring the same process in other caldera settings. This is a further example of volcano-tectonic interactions in the central TVZ, involving a previously unexplored area beneath Lake Taupō's Western Bay.

Acknowledgements

Firstly, I would like to express my gratitude to my supervisors Finn Illsley-Kemp and John Townend for their constant support over the course of this thesis. Finn, thank you for introducing me to this project and the Taupō Volcanic Zone, this region is of great interest to me now and I am sure it always will be. Thanks for the regular catch ups, both in person and on zoom, which helped keep me on track in the constant uncertainty COVID has caused. Thank you for making me feel at home during this time, whether by indoor football or cat-sitting. John, thank you for the incredible opportunity to be part of the team deploying the SALSA seismometer array. This is undoubtedly one of the best experiences of my life and I think it's unlikely I will get to work in such incredible scenery again any time soon. Thank you for your comprehensive advice and notes, which I know has pushed me to produce the best piece of work I am capable of.

This project could not have happened without a number of financial supporting partners. I would like to thank the Evison Family, the Earthquake Commission, GNS Science, the New Zealand Geophysical Society and the other private donors who contribute to the Frank Evison Research Scholarship. I would like to additionally thank the Earthquake Commission for their support via a scholarship awarded under the auspices of the EQC Programme in Earthquake Seismology and Tectonic Geodesy. Without these two scholarships, this research would not have been possible. Additionally, I would like to thank the ECLIPSE program team for their support. The expertise and funding provided by this group went a long way in helping me complete my research objectives.

Besides my supervisors, I would like to thank Eleanor Mestel and Calum Chamberlain, who helped me significantly during the strenuous processing of my data. Without your help navigating the different Python packages used for matched-filter detection and earthquake relocation, I would likely still be manually picking events today.

To all the people I've shared workspaces with: Callum, Theo, Greta, Henriette, Adrija, Kristian, Libby, Olivia, Jessie, Nicola, Ash, Kees, Sam, Olivia and Carmen. Thanks

for making this an incredible year: the crosswords were a particular highlight. I am sad to leave but I wish all of you the best moving forward.

Thanks to my family, who have supported me from distance through three separate lockdowns. Finally, a special thanks to my partner Olivia, who has provided incredible support for me throughout this research. You have helped me carry on through some trying times, especially coming down to the finish line, and have been a constant source of inspiration to me.

Statement of authorship

For the purposes of formulating my interpretation of the 2001 seismicity occurring in the Taupō Fault Belt, I will be utilising the personal pronouns ‘we’ and ‘our’. This is to show that this was a collaboration with my supervisors Finn Illsley-Kemp and John Townend. However, the work produced is solely my own.

Contents

List of Figures

List of Tables

Chapter 1

Introduction

1.1 Research objectives and motivation

1.1.1 Why Taupō?

Lake Taupō occupies the caldera of Taupō Volcano (Figure 1.1), which dominates the southern portion of the central Taupō Volcanic Zone in New Zealand. Taupō Volcano is one of two currently active volcanic calderas in the central Taupō Volcanic Zone, along with Okataina Volcano, and has erupted 25 times in the last 12,000 years (Barker et al., 2015, 2021). The eruption deposits from these events show little correlation between their size and the time separating them, highlighting the unpredictable nature of the volcano (Wilson, 1993).

The lack of correlation is likely due to the proposed interplay of three independent factors: the rhyolitic magma reservoir beneath Lake Taupō, the mafic magma feeder system, and tectonic stresses around Taupō (Rowland et al., 2010). Understanding this complex three-way coupling mechanism is key to eruption hazard forecasting at Taupō. This important considering its close proximity to Taupō and Kinloch townships (Figure 1.1) as well as several geothermal power plants. Recent geophysical studies, such as seismic imaging and relocation of earthquakes beneath Lake Taupō have provided insight into subduction-related flux melting and how it is fuelling the current silicic magma reservoir beneath Taupō (Stern & Benson, 2011; Barker et al., 2021; Illsley-Kemp et al., 2021). The presence of a shallow magma reservoir was further indicated by seismic anisotropy analysis, which highlighted a zone of stress deviation around the lake (Illsley-Kemp et al., 2019).

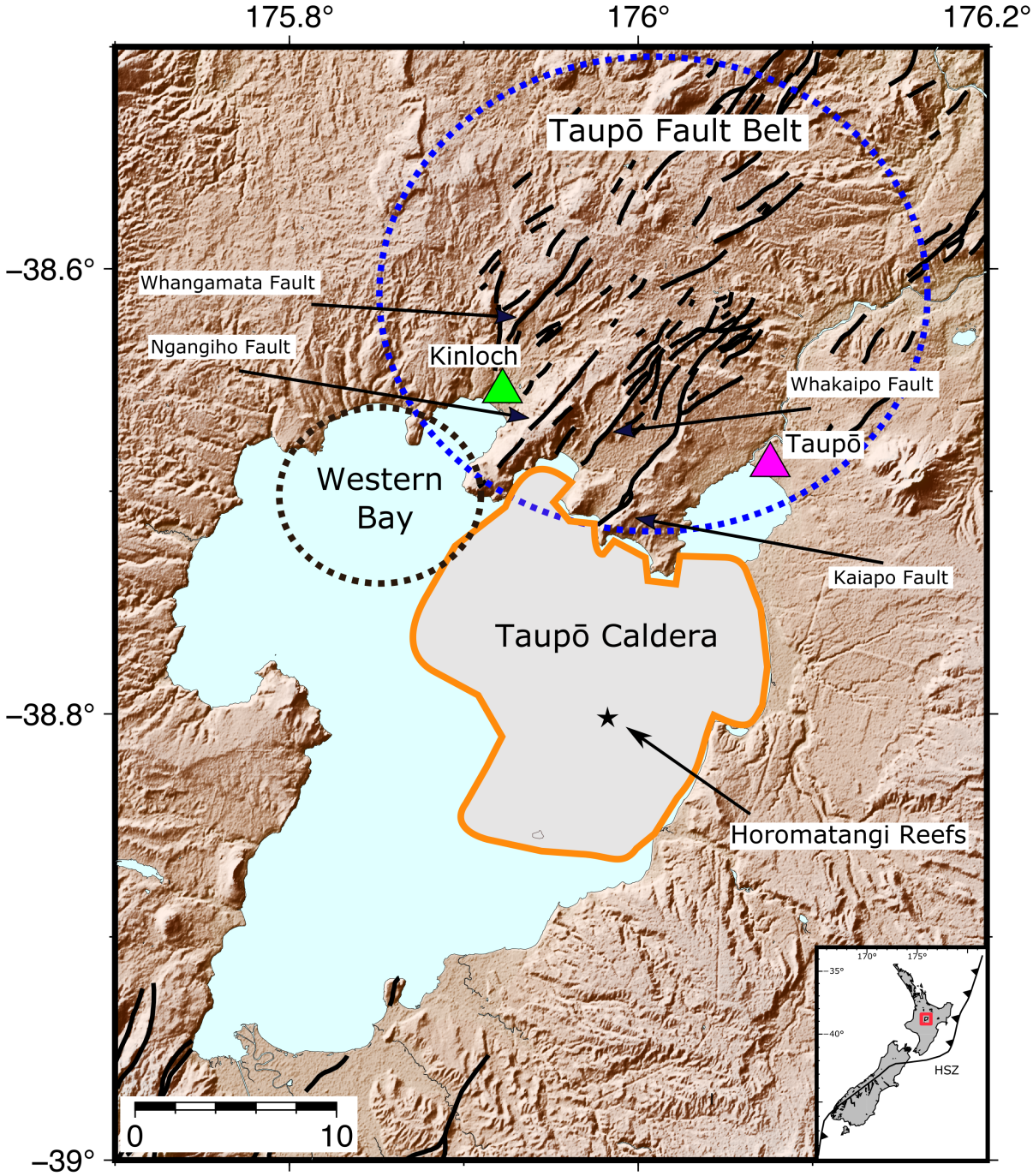

Figure 1.1: Map of Taupō area, showing the locations of the Taupō caldera and the Taupō Fault Belt to the north. The western bay of Lake Taupō has been identified as it is relevant. Four major faults within the fault belt have been labelled. The black star represents the Horomatangi Reefs volcanic vent site. The two triangles designate local townships (green: Kinloch, purple: Taupō).

Taupō Volcano is closely aligned with the Taupō Rift, prominently expressed as the Taupō Fault Belt (Rowland et al., 2010) on Lake Taupō's northern shore (Figure 1.1). The Taupō Fault Belt is comprised of multiple northeast-striking faults, including four prominent ones controlling the topography of the belt. These are the Kaiapo, Whakaipo, Ngangiho and Whangamata faults (Figure 1.1), which have all been associated with either confirmed or inferred surface cracking during documented unrest periods (Hull & Grindley, 1984; Otway et al., 1984; Potter et al., 2015). Differentiating earthquakes of tectonic and magmatic origin around Taupō can be extremely challenging, but determining whether there is unrest within the magma reservoir is important for eruption forecasting in addition to government and private business forward planning (Charlton et al., 2020). Furthermore, seismicity is a valuable tool for aiding the understanding of factors influencing Taupō Volcano, with numerous periods of unrest within the caldera being used to demarcate possible future eruption sites and the extent of the modern magma reservoir (Potter et al., 2015; Illsley-Kemp et al., 2021).

Understanding of Taupō's magma reservoir has improved in recent years, in large part due to the work of the ECLIPSE (Eruption or Catastrophe: Learning to Implement Preparedness for future Supervolcano Eruptions) research program. The ECLIPSE program is aiming to further understand what causes switches between dormancy, unrest and eruption at New Zealand volcanoes, while also determining mitigation strategies for future eruptions. At Taupō, ECLIPSE is aiming to improve earthquake detection and location while also producing direct seismic imaging of the Taupō magmatic system (Barker et al., 2021). However, quantifying how this reservoir interacts with the Taupō Rift is less clear. There is evidence that tectonic processes are responsible for triggering past eruptions at Taupō and the tectonic stress state around the volcano is inferred to be a key factor in whether an eruptible melt body can form (Rowland et al., 2010; Allan et al., 2012).

The primary objective of this thesis is to investigate the interaction between Taupō's magma reservoir and the local tectonic system, specifically the Taupō Fault Belt. Studying the potential interaction between these structures on a refined scale will help to build on the current understanding of the factors influencing Taupō Volcano's activity. Ideally, this research can be further used to inform hazard management planning, for both seismic and volcanic hazards, around Taupō.

1.1.2 Why Focus on 2001?

To investigate the potential effects of the tectonic system upon Taupō's magma reservoir, and vice versa, we will be utilising earthquakes occurring in the region. A period of unrest occurs when seismicity rises above a constant low threshold exhibited by many volcanoes (Potter et al., 2014; Potter et al., 2015). This threshold will vary relative to each volcano. Utilising the "Volcanic Unrest Index" (VUI) Potter et al. (2015) have defined moderate unrest at Taupō Volcano as having the following characteristics: earthquakes swarms lasting between 90 days and 6 months, earthquakes occurring between 4–8 km depth within the caldera, more than 30 magnitude > 4 earthquakes per month and/or a ground deformation rate of more than 100 mm/year from a source at 4–8 km depth. Four of these 'moderate' unrest periods were identified in 1887, 1922, 1964 and 1983 (Potter et al., 2015), although these were all prior to the deployment of seismometers around the lake in 1985. Instead we are focused on the four periods of minor unrest which have occurred since instrument deployment. These periods are as follows: 1996-99, 2001, 2008 and 2019 (Peltier et al., 2009; Potter et al., 2015; Illsley-Kemp et al., 2021). The accuracy of earthquake locations within these periods increases with time, however there are clear parallels between the 1996-99, 2008 and 2019 swarms. In all, seismicity occurred beneath the lake, within the bounds of the Taupō caldera and show little evidence of fluid motion or slip on any surrounding faults (Potter et al., 2015; Barker et al., 2021). While some of these unrest periods provide valuable information about the magma reservoir (Illsley-Kemp et al., 2021), they tell us little about the local tectonic system.

This leaves the minor unrest which occurred in 2001, primarily within the Taupō Fault Belt. The initial location of this seismic swarm and the apparent linear distribution of earthquakes are in stark contrast to other seismic swarms recorded around Taupō. The GeoNet locations for these events constrain them outside the bounds of Taupō caldera and align them with the prominent Kaiapo Fault. Given unrest beneath the caldera has been attributed to the underlying magma reservoir (Illsley-Kemp et al., 2021), this suggests the 2001 swarm may be the result of slip on faults within the belt.

This thesis will focus on analysing the temporal and spatial distributions of the relocated events that occurred during the 2001 swarm, aiming to interpret patterns in these distributions. This approach will uncover any interaction between the faults within the Taupō Fault Belt, as well as the direction in which earthquakes are propagating. Further understanding the dynamics of the Taupō Fault Belt and any interaction it may have with the underlying magmatic system will help shed light on the large-scale

magma-tectonic processes at play in the central Taupō Volcanic Zone.

Given the 2001 earthquake swarm's contrasting distribution to others in the area, it is imperative to utilise the recorded earthquake data and process it to achieve increased resolution. Analysing these events will help interpret the faults within the Taupō Fault Belt and the wider tectonic system at Taupō. Determining the state of any interaction these faults may have with Taupō Volcano may also be critical for future hazard modelling in the region.

1.1.3 Research objectives

The research objectives of this thesis can be summarised as below:

1. To identify and accurately locate earthquakes that occurred during the 2001 unrest period in the Taupō Fault Belt.
2. To determine, through the distribution of earthquakes and by calculating focal mechanisms, whether these events are the result of tectonic or magmatic processes.
3. To analyse the spatial and temporal distribution of the located events, with the goal of identifying fault planes and propagation patterns
4. To investigate any interaction between the faults in the Taupō Fault Belt and Taupō Volcano. This will serve a broader objective of furthering understanding of the interplay between the tectonic and magmatic regimes in the central Taupō Volcanic Zone
5. To identify possible hazards that further motion on the accommodating faults in the Taupō Fault Belt may pose. This will encompass both the fault related hazards and the potential for any volcanic hazards that may result from interaction between the Taupō Fault Belt and Taupō Volcano.

1.2 Geological background

1.2.1 The Taupō Volcanic Zone

The Taupō Volcanic Zone (TVZ) is the southernmost stretch of the ∼2800 km Tonga-Kermadec volcanic arc (Figure 1.2), with its ∼300 km continental extension dominating New Zealand's central North Island (Cole & Lewis, 1981). However the TVZ does not share the typical front to back-arc configuration of the Kermadec arc and is instead defined as a rifted arc (Wilson et al., 1995, 2009). This is because the TVZ is the onshore product of the adjacent Hikurangi Subduction Zone (Figure 1.2), where the Pacific plate is being obliquely subducted west beneath the Australian plate (Wright & Ballance, 1993; Parson & Wright, 1996; Wallace et al., 2007; Villamor et al., 2017). This convergent margin ultimately drives heat flow in the TVZ, with volcanism fuelled by basaltic magma originating from partial melt on the subducted mantle wedge (Eberhart-Phillips et al., 2020). These basaltic intrusions act to recharge the shallow silicic system in the central TVZ through a complex mechanism of sills and crystal mush zones (Barker et al., 2020). The TVZ shows strong segmentation based on magmatic composition, with andesitic volcanism dominating its southern and northern regions (Wilson et al., 1995, 2009). The central TVZ is rhyolitic in composition and houses as many as eight caldera systems (Wilson et al., 2009). Present-day heat flow is an order of magnitude less and the average magma eruption rates are significantly lower in both the northern and southern TVZ when compared to its central segment (Cole et al., 2000).

The central TVZ is broadly analogous to other large caldera systems such as Yellowstone in Wyoming, leaving a similar geographic footprint with even higher eruption rates (Wilson et al., 1984, 2009; Wilson & Charlier, 2016). These calderas each have prominent hydrothermal systems and regular unrest despite not producing any eruptions on a human timescale (Acocella et al., 2015). Felsic calderas (e.g. Rabual caldera in Papua New Guinea) are more complex than their mafic counterparts (e.g. Taal caldera in the Philippines), which are characterised by repeated cycles of unrest and inflation, typically followed by eruption (Acocella et al., 2015). By contrast, felsic calderas experience numerous unrest periods without an ensuing eruption, with magmatic injections possibly buffered by large magma chambers or hydrothermal systems (Acocella et al., 2015). In addition, calderas analogous to those in the central TVZ are judged to have semi-plugged conduits, with magmatic intrusions resulting in resurgence in the surrounding area. This semi-plugged state allows larger magmatic systems to sufficiently de-gas to stave off eruption, accommodating magmatic intrusions as melt

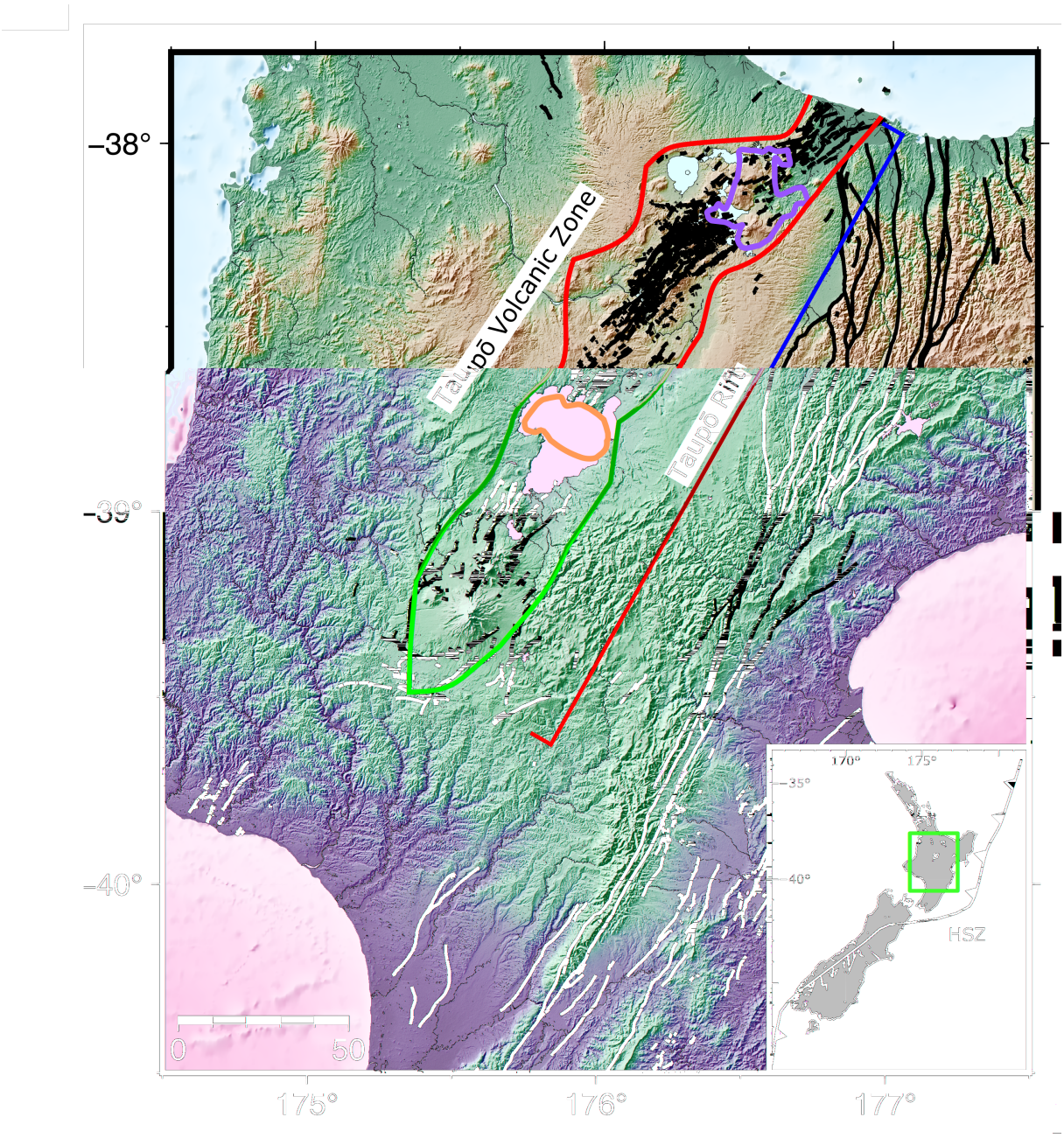

Figure 1.2: A map view of New Zealand's central North Island. The modern Taupō Volcanic Zone (red) has been adapted from Rowland et al. (2010). The two active caldera systems are Taupō and Okataina (purple outlines). The axis of the Taupō Rift, which aligns closely with the Taupō Volcanic Zone, is shown with a dark blue line. Active faults are shown in black. The wider tectonic setting, outlining the Hikurangi Subduction Zone (HSZ) and the opposing senses of subduction, is inset bottom-right.

bodies (Acocella et al., 2015).

There are currently two active caldera volcanoes in the TVZ (Figures 1.2 & 1.3). The first is Taupō, which last erupted in ∼232CE (Hogg et al., 2012, 2019) and which defines the southern portion of the central TVZ with its overlying Lake Taupō (Wilson & Walker, 1985; Davy & Caldwell, 1998). The Oruanui super-eruption, which occurred ∼25.5 ka, and collapse of the resulting caldera also contributed significantly to the structure of Lake Taupō (Davy & Caldwell, 1998). The southern terminus of Taupō Volcano is marked by the Maunganamu and Kuharua rhyodacite domes (Wilson et al., 1986; Sutton et al., 1995).

The second caldera currently active is Okataina Volcano, which sits at the northern end of the central TVZ (Wilson et al., 1995, 2009). Okataina Volcano is situated within the Okatain Caldera Complex (Cole et al., 2005; Cole & Spinks, 2009). The most recent rhyolitic and basaltic eruptions at Okataina occurred in 1314AD and 1886AD respectively (Nairn et al., 2001; Sable et al., 2006). These two caldera volcanoes have produced more than 770 km^3 of rhyolitic magma combined over the past 60 kyrs (Wilson et al., 2009).

1.2.2 Evolution of the Taupō Volcanic Zone

The chronology of the TVZ can be separated into three phases: Old, Young and Modern. The Old TVZ spans from 2 Ma to 350 ka (Wilson & Rowland, 2016). During this phase, the TVZ is believed to have begun with andesitic volcanism before being overridden by large volumes of rhyolitic volcanism around 1.6 Ma, which has persisted since (Houghton et al., 1995; Briggs et al., 2005). A detailed stratigraphic and chronological record is yet to be defined for the Old TVZ, as most early eruption deposits were lost to erosion or burial (Wilson & Rowland, 2016). However, some information has been recovered using a combination of drill-core data (Gravley et al., 2006) and outcropping in coeval sedimentary basins (Shane & Froggatt, 1991).

The transition from the Old to Young TVZ is marked by widespread fall and ignimbrite deposits from the Whakamaru super eruption (Leonard et al., 2010). This acts as a marker for the base of the Young TVZ, which spans from ∼350 ka until the Rotoiti eruption at ∼55 ka (Barker et al., 2021). During this phase, the major structural controls of the TVZ were established, controlling the position and nature of heat sources and geothermal systems in the area (Wilson & Rowland, 2016). While this period was dominated by silicic magma, there were some instances of basaltic volcanism from

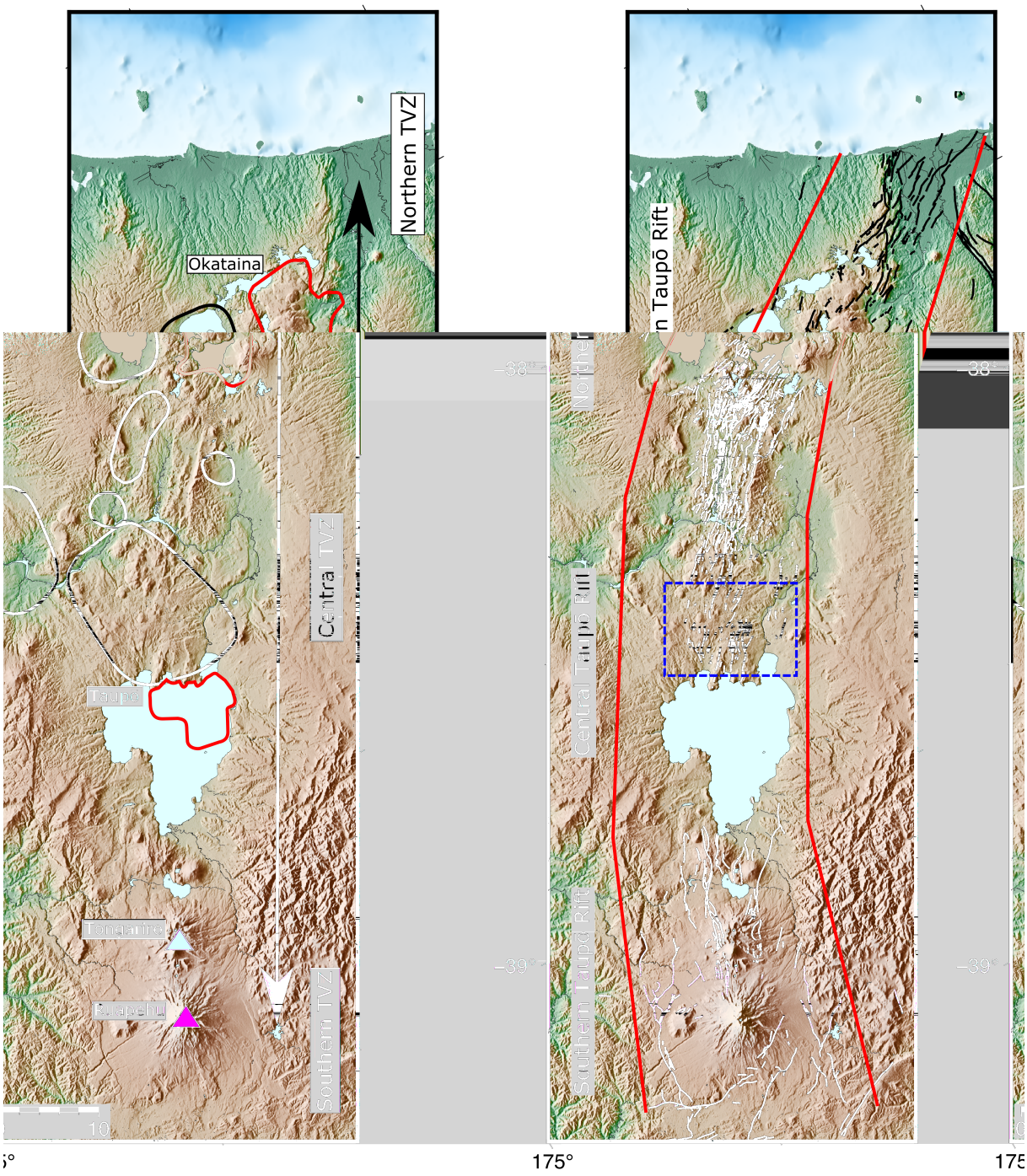

Figure 1.3: This figure consists of a two-panel plot, showing high resolution maps of the Taupō Volcanic Zone (TVZ, left) and Taupō Rift (right) separately. The TVZ subplot has active caldera systems labelled and outlined in red, with inactive calderas outlined in black. Andesite volcanoes in the southern TVZ were designated with purple triangles and labelled. The Taupō Rift plot outlines the changing axis of the rift in red lines and active faults in black.The Taupō Fault Belt is outlined with a blue box.

200 ka onwards (Houghton et al., 1987). The alignment of these basaltic deposits with NNE-SSW faults suggests they resulted from dike intrusions, originating from the mafic feeder zone beneath the TVZ. Constructing a complete record of the Young TVZ is challenging (Wilson & Rowland, 2016). The eruption record for this period is more complete than the Old TVZ, especially for large eruptions, but smaller events remain obscured (Manning, 1996; Wilson et al., 2009). This provides a good idea of general volcanism, but leaves more nuanced trends unclear.

The Modern TVZ is defined as encompassing all deposits following the tephra deposits from the Rotoiti eruption, dated at 54 ka based on argon dating and marine terrace chronology (Berryman, 1992; Barker et al., 2016; Wilson & Rowland, 2016). This eruption occurred from the Okataina caldera and its deposits are regionally extensive, making it an effective marker deposit (Nairn, 1972). The Rotoiti eruption also marked the onset of increased explosive activity from Taupō Volcano, which is a hallmark of the Modern TVZ (Nairn, 1972). The Young and Modern TVZ are separated based on the quality of their stratigraphic and chronological record. Following the Rotoiti event, the eruption record for the central TVZ is considered complete (Vucetich & Howorth, 1976). The Modern TVZ can be further subdivided based on multiple large scale rhyolitic eruptions within this stage.

In the 20 kyrs following the Rotoiti eruption, volcanism was characterised by a wide spread of eruption vents and a mixture of effusive and explosive styles (Barker et al., 2021). These eruptions were typically separated by long periods of quiescence, with a thick layer of undisturbed paleosoil around Lake Taupō suggesting up to 12 kyrs without an eruption (Barker et al., 2021). The eruptive deposits produced during this 20 kyr stretch are categorised into 'Oruanui Type' and 'NE-dome Type' magmas (Sutton et al., 1995; Wilson & Charlier, 2009). The 'Oruanui Type' magmas primarily erupted from vents in Lake Taupō and share overlapping major and trace element compositions with magmas from the more recent Oruanui super-eruption (Wilson & Charlier, 2009). In contrast, the 'NE-dome Type' magmas generally erupted northeast of Lake Taupō (Sutton et al., 1995). Geographic separation in addition to contrasting composition and zircon age spectra indicates two independent magmatic systems were operating in the TVZ between the Rotoiti and Oruanui events (Charlier et al., 2005; Wilson & Charlier, 2009).

The Oruanui super-eruption (∼25.5 ka) erupted over 1100 km^3 of pyroclastic material including 530 km^3 of rhyolitic magma through ten phases (Allan et al., 2012, 2013). This event was not only the largest phreatomagmatic eruption globally documented, but also the youngest known supereruption (Self, 1983; Wilson & Walker, 1985). The

dominant magma produced during the Oruanui eruption was a high-SiO_2 rhyolite (Wilson et al., 2006; Allan et al., 2017). Two minor magma types also erupted, a low-SiO_2 rhyolite magma and a biotite bearing rhyolitic magma (Allan et al., 2012; Myers et al., 2019). The low-SiO_2 magma was inferred as the less evolved magma feeding the high-SiO_2 magma, while the biotite rich magma was believed to feed into the Oruanui chamber from the independent 'NE-Dome' system (Allan et al., 2012). This hints at the complex interplay between the tectonic and magmatic processes occurring in the TVZ.

Despite the size of the Oruanui eruption, only 5000 years passed before the next event occurred at Taupō (Barker et al., 2021). This indicates the speed of recharge in the reservoir beneath Taupō, reiterated by the 28 different eruptions which followed (Wilson, 1993). While some of the earlier eruptions were dacitic in composition, the remaining 25 events, occurring solely in the last 12 kyrs were rhyolitic (Wilson & Charlier, 2009). This 12 kyr period at Taupō displayed wide varieties in eruptive volume, repose time and vent locations (Wilson, 1993). This variation in eruptive behaviour is inferred to have not occurred prior to Oruanui, with the addition of dacitic deposits especially notable (Barker et al., 2014, 2015). This heterogeneous composition of deposits suggests the TVZ magma system was reset post-Oruanui, with a deeper mafic source reinvigorating the shallower silicic system responsible for volcanism (Charlier et al., 2010; Barker et al., 2015).

The Taupō eruption in 232CE marks the most recent development in the evolution of the TVZ, with one eruption phase described as the most powerful Plinian outburst yet documented (Wilson & Walker, 1985). This eruption occurred in the north-eastern corner of the caldera created by the Oruanui super-eruption (Figure 1.4) and formed the present shape of Lake Taupō (Davy & Caldwell, 1998). Similarly to Oruanui, the Taupō eruption can be divided into seven distinct phases based on eruption intensity, the amount of magma-water interaction and the location of the erupting vents. The erupting vents migrated parallel to the strike of the TVZ (Healy, 1964; Froggatt, 1981). This event is considered unique to the other post-Oruanui eruptions, given it produced five times the amount of eruptive material (Davy & Caldwell, 1998). The pyroclastic density current devastated approximately 20,000 km^2, indicating the power present in the current magmatic system (Wilson, 1985).

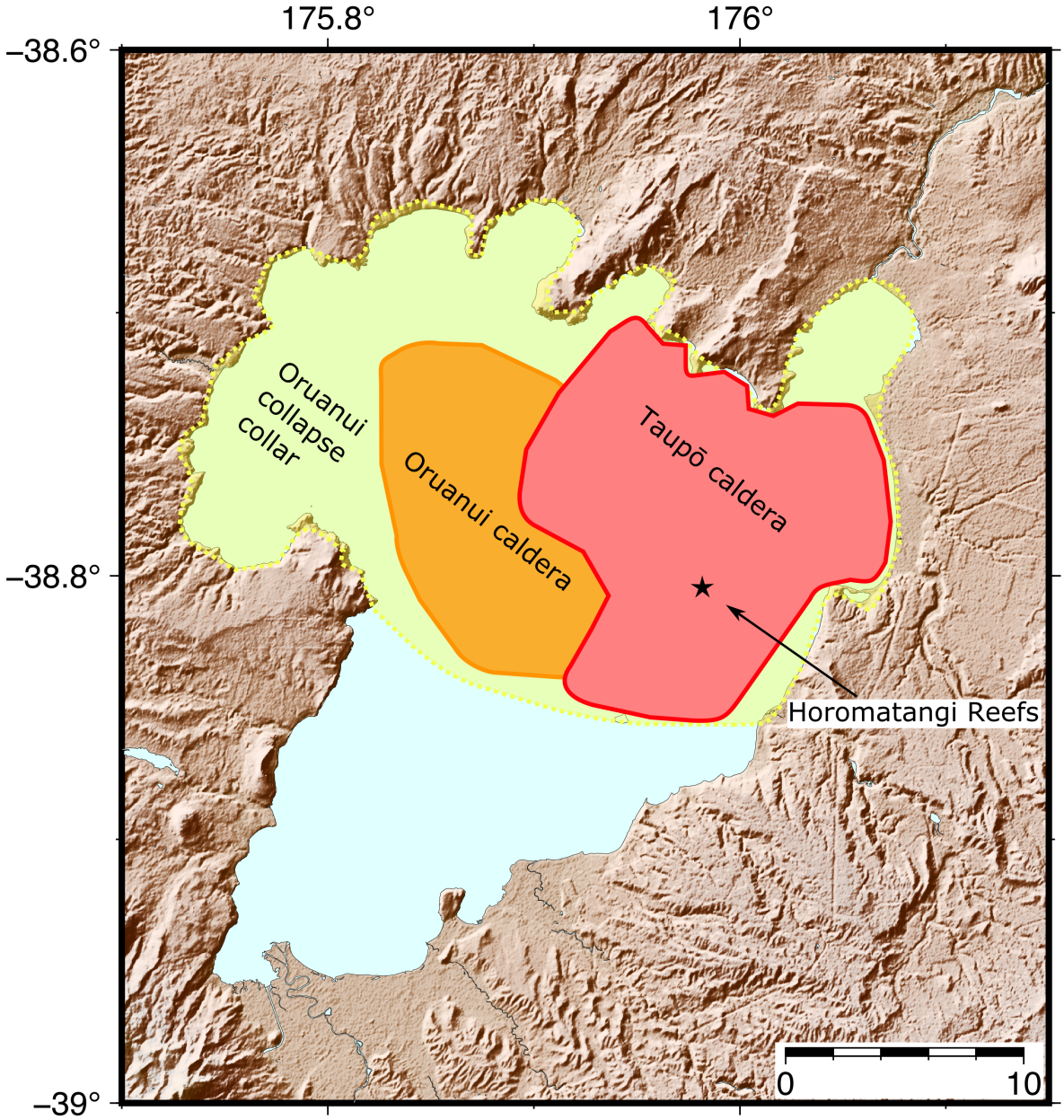

Figure 1.4: Map of the Taupō region, outlining the different calderas beneath Lake Taupō. The Taupō caldera is shown in red, the Oruanui structural caldera in orange and the Oruanui collapse collar is depicted as a yellow region with a dashed border. Horomatangi Reefs is represented with a black star. Figure adapted from Illsley-Kemp et al. (2021).

1.2.3 The Taupō Rift

The Taupō Rift is closely associated with the TVZ, currently widening at rates of 7 mm/yr in its southern region and 15 mm/yr to the north (Wilson & Rowland, 2016). Rifting commonly occurs at divergent and intra-continental settings, such as the Afar and Main Ethiopian Rifts (Ayele et al., 2007; Villamor et al., 2017). The Taupō Rift is a product of the Hikurangi Subduction Zone, with variation in the angle of the subducting slab producing the diverse expansion rates seen along the rift (Parson & Wright, 1996; Seebeck et al., 2014). This convergent setting and association with active volcanism, defines the Taupō rift as an intra-arc rift (Villamor et al., 2017). Melting of the mantle is a fundamental control in rifting mechanics, as the rising of mafic magma is an effective method to accommodate extensional strain (Rowland et al., 2010). This control is provided by flux melting on the subducting slab beneath the central North Island. The rift displays three primary mechanisms of rifting: narrowing, lateral migration and along strike propagation (Villamor et al., 2017).

The evolution of the Taupō rift can be subdivided into 'Old' (2 Ma-350 ka), 'Young' (350 ka-25 ka) and 'Modern' (25 ka-recent), similarly to the TVZ. However, these ages are based on relative dating of fault structures rather than absolute dating of eruptive deposits and are subject to inconsistency (Villamor et al., 2017). Issues arise here due to the dominance of volcanic deposits in the Taupō Rift, which are poorly cohesive and less likely to preserve evidence of extensional structures than other deposit types (Rowland et al., 2010). Additionally, as deposits from each eruption do not span the entirety of the rift, constraining faulting in different regions of the rift can be challenging (Villamor et al., 2017).

The 'Old' rift (2 Ma-350 ka) has a largely incomplete record, in large part due to rapid subsidence of rifted areas as well as large scale eruptions at 550 ka and 350 ka which have buried much of the faulting evidence (Villamor & Berryman, 2006b,a; Chambefort et al., 2014; Downs et al., 2014; Mouslopoulou et al., 2008). Hence it is difficult to determine the age of rift initiation, instead inferred as coeval with the TVZ at $\sim$ 2 Ma (Wilson et al., 2009; Cole & Spinks, 2009; Chambefort et al., 2014). The first confirmation of rift faulting in the region is a shift in the tectonic regime from strike-slip to extensional, identified from geothermal borehole stratigraphy in the northern TVZ (Milicich et al., 2013). The width of the old Taupō rift is $\sim$ 70 km, as indicated by steep negative gravity contours from buried bounding faults (Figure 1.5 (Seebeck et al., 2014; Wilson & Rowland, 2016; Stagpoole et al., 2021)). These anomalies indicate significant displacement on the 'Old' boundary faults, suggesting

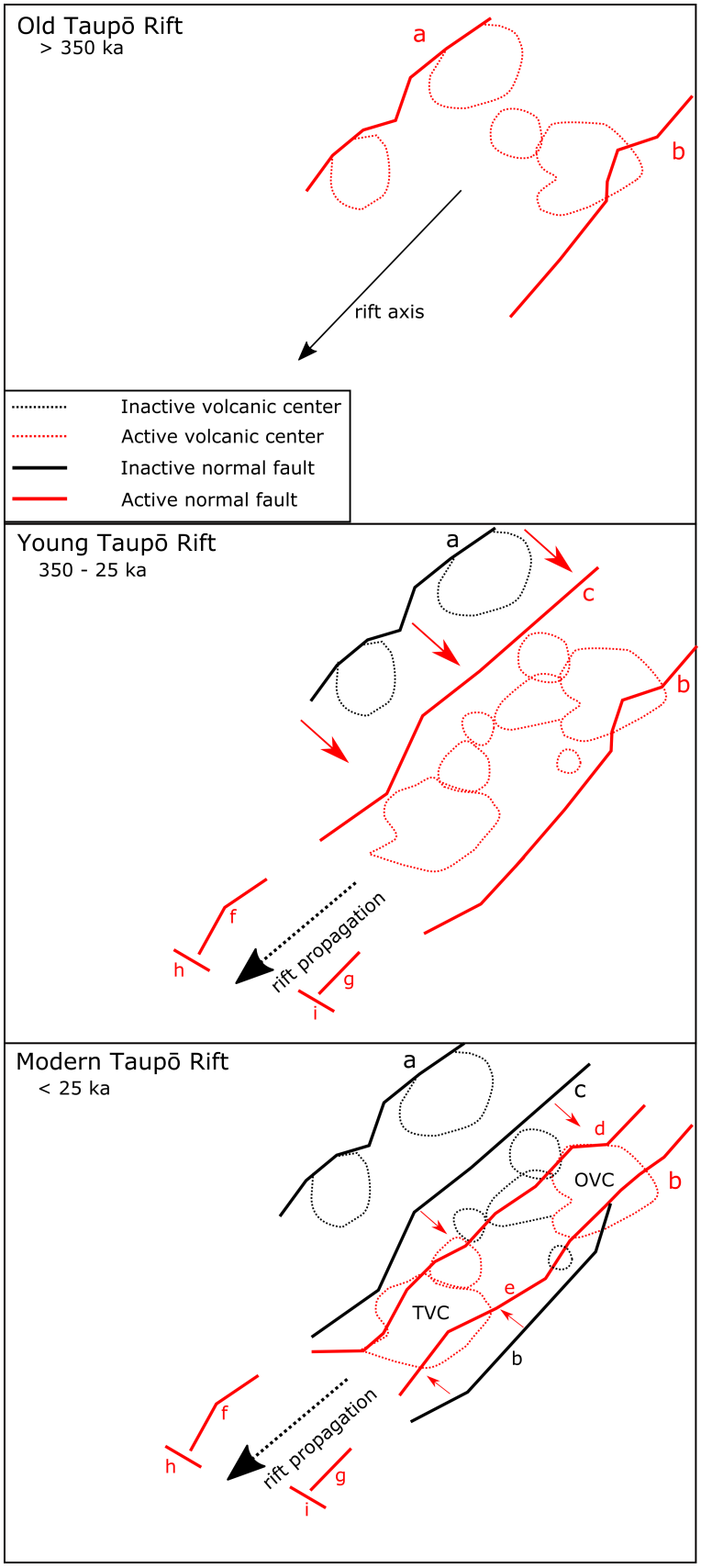

Figure 1.5: Conceptual model of the evolution of the Taupō Rift, adapted from Villamor et al. (2017).

most early extension was accommodated through tectonic rifting prior to the emergence of volcanism (Villamor et al., 2017).

During this stage of rifting, the western boundary shifted significantly eastward (Figure 1.5), as reflected by small, disconnected gravity anomalies on this edge (Villamor et al., 2017; Stagpoole et al., 2021). These contours step eastward, connected by perpendicular accommodation zones in a pattern not shared by the eastern boundary (Villamor et al., 2017). Thus the narrowing of the rift during this stage was largely asymmetrical. The eastern bounding faults migrated later, triggered by rollback in the subducting slab (Stern et al., 2006).

The Young Taupō Rift (350 ka–25.5 ka) shows significantly faster evolution, likely associated with an increase in shallow silicic volcanism (Figure 1.5). The Young Rift is bounded by super eruptions, displacing units following and prior to the Whakamaru and Oruanui super-eruptions respectively (Villamor et al., 2017). For example, the Pokuru fault in the central rift displaces older Maroa volcanic domes (∼140-250 ka) but not the Oruanui ignimbrite (Villamor et al., 2017).

During this period there is significant narrowing of the rift as extension becomes more constrained (Villamor et al., 2017). The majority of total rift narrowing and extension occurred during this stage, as the western margin continued to migrate inwards in the central and northern rift (Figure 1.5). The narrowing that occurred during this phase would require $\sim$ 5 Myrs of extension at current values, more than the full rift timespan (Svartman Dias et al., 2015). This lack of extension is accommodated in part by tectonic structure, with the inherited basement structure of the rift trending subparallel to its strike (Seebeck et al., 2014). This has been inferred to increase the rate of narrowing in the area, as extension is accommodated by these favourable faulting conditions (Seebeck et al., 2014).

Volcanism was another key factor in the increased narrowing of the Young Rift, evidenced by a lack of subsidence, as the rift remained elevated due to consistent magmatic re-invigoration (Rowland et al., 2010). The evolution to a magma-assisted rift (Villamor et al., 2011), also allowed extension to occur at lower stress levels than mechanical faulting (Corti et al., 2003; Buck, 2004). The large volumes of silicic volcanism and shallow magma chambers that coincided with the Young Rift reduced the strength and thickness of the crust within the rift (Villamor et al., 2017). This prompted the inward migration of faulting towards the central nuclei, narrowing the rift as a whole (Corti et al., 2013; Zwaan et al., 2016).

In addition to significant narrowing in the central and northern sections, the Young Rift

experienced southward propagation along strike (Figure 1.5). The southern portion of the rift had an initial width of ∼40 km, approximately 30 km narrower than the Old Rift boundaries (Villamor et al., 2017). This affirms that southward propagation of the rift occurred after narrowing of the central and northern regions during the Old Rift stage. This narrowing concentrated stress at the southern tip of the rift, encouraging propagation along strike (Villamor et al., 2017).

The Hikurangi Subduction Zone is also a strong control on rift orientation and was migrating south at rates of ∼33 km/Myr (Wallace et al., 2007). This is believed to have led the southward propagation of the rift. However, the propagation rates in the southern rift are up to 10 times faster than the migration of the Hikurangi Subduction Zone (Wallace et al., 2007). This indicates propagation was unlikely the result of purely structural controls, with the influx of silicic volcanism also coinciding with southward propagation (Villamor & Berryman, 2006a). Massive ignimbrite eruptions during this phase in the Central TVZ are inferred to have cause rotations in the principal stress orientations in the rift, aiding southward propagation (Ellis et al., 2014).

The Modern Rift (<25.5 ka) is approximately 20km wide, displaying approximately 50 km of narrowing over two million years (Ellis et al., 2014), (Figure 1.5). This substantial thinning of the crust, with cumulative vertical slip rates on faults around Taupō of ∼4–5 mm/yr should have produced around 10 mm/yr of subsidence along the rift (Rowland & Sibson, 2001; Villamor & Berryman, 2001). Approximately 100 m of expected subsidence should be reflected in paleo-shorelines around Lake Taupō, formed due to rising water levels following the Oruanui super-eruption (Manville et al., 1999; Manville, 2002; Barker et al., 2021). However, no net subsidence is visible. This suggests that during the modern rift, the emplacement of large silicic magma bodies nullified the subsidence caused by faulting (Manville & Wilson, 2003).

The central and northern regions of the Modern Rift show substantial narrowing and crustal thinning compared to the south (Figure 1.5), but these areas are heterogeneous in maturity. As rifts mature, more extension is accommodated by magma (Buck, 2004; Buck et al., 2006; Villamor et al., 2017), evidenced by the volcanic centres in the central and northern rift. However, in the regions separating the two active caldera volcanoes, most extension is accommodated by faulting (Seebeck & Nicol, 2009; Rowland et al., 2010; Villamor et al., 2011; Allan et al., 2012). It is inferred that some areas in the central and northern rift have undergone evolutionary reversal, having once matured to magma-dominated rifting but have since regressed to tectonic accommodation of extensional stress (Villamor et al., 2017). One example is the region separating the Taupō and Maroa Volcanic Centres. This zone housed multiple eruptions during the

young stage of the rift, but in the modern stage only accommodates extension via faulting (Rowland & Sibson, 2001; Seebeck et al., 2014). By contrast, the southern section of the rift has experienced little modern magmatic extension and has no silicic volcanic centres (Villamor et al., 2017), (Figure 1.5). Instead, most extension here is purely mechanical and largely accommodated by motion on the eastern boundary fault (Villamor & Berryman, 2006b; Cassidy et al., 2009).

The evolution of the Taupō rift has been notably faster than in intracontinental rifts. Most intracontinental arcs take a minimum of 10 million years to evolve from a purely extensional regime to a magma-dominated setting (Wolfenden et al., 2005). In these settings, volcanism requires sufficient thinning of the crust to initiate, which can take up to 10 million years through faulting (Villamor et al., 2017). By contrast, the Taupō Rift was coeval with the emergence of the TVZ and became magma-dominated within 2 million years. The presence of the Hikurangi Subduction Zone meant that large scale volcanism was present during the rift's initiation, accelerating its evolution (Villamor et al., 2017). This reduces the influence of tectonic faulting, meaning bounding faults in the Taupō rift are less prominent than in intracontinental rifts (Avni et al., 2012; Bosworth & McClay, 2001).

1.3 Taupō and magma-tectonic interaction

1.3.1 Current conditions at Taupō

Holocene volcanism (12 ka – present) has provided insight into the modern state of Taupō's magma reservoir, which is important to understand when regarding the risk Taupō Volcano currently poses (Barker et al., 2021). Eruptive products from the 25 Holocene eruptions at Taupō show little compositional variation and are crystal-poor, despite a range of vent sites and eruptive volumes (Barker et al., 2015). This suggests rather than a long-lived magma chamber beneath Taupō, crystal poor rhyolitic melts are being mobilised from a deeper crystal mush (O. Bachmann & Huber, 2016; Illsley-Kemp et al., 2021). This modern system evolved rapidly following the Oruanui super-eruption, as the resulting decompression prompted a large influx of mafic magma to reset the mush system (Barker et al., 2015). Holocene eruptive products indicate two key factors. Firstly, uniform mineralogy through eruptions suggests that rhyolitic melts were being assembled as large melt bodies prior to eruption (Dunbar et al., 1989; Sutton et al., 1995; Barker et al., 2015). Secondly, diffusion ages from the deposits suggested these eruptible melt bodies were assembled on decadal timescales (Barker et

al., 2016). This gives a strong indication that conditions at Taupō Volcano can change in a time-frame relevant to current hazard monitoring.

A lack of pre-eruptive zoning in Holocene eruptive deposits also implies these rhyolites were erupted shortly after being extracted and assembled at 5–8 km depth, based on melt inclusion H_20/CO_2 contents (Dunbar et al., 1989; Barker et al., 2015; Myers et al., 2018, 2019). This places the shallow rhyolitic system within these depth boundaries. A first order estimate of a 250–1000 km^3 mush zone was made based on combining this depth estimate with vent spacing (Barker et al., 2015).

This estimate was further refined following analysis of seismic unrest beneath Lake Taupō in 2019. The earthquakes during this unrest were located to the northeast and southwest of the Horomatangi Reefs (Figure 1.4), the vent area within the lake deemed the most likely location for a future eruption (Otway, 1986; Webb et al., 1986; Wilson, 1993; Illsley-Kemp et al., 2021). This gap in seismicity around Horomatangi Reefs defines the width of the modern reservoir, highlighting the brittle-ductile transition as its edges (Illsley-Kemp et al., 2021). Based on this distribution of earthquakes and inferring the eastern boundary based on vent positions, a minimum volume estimate of 80 km^3 was determined (Illsley-Kemp et al., 2021). However, the maximum area exceeds 250 km^3, as the lack of seismicity to the northwest could indicate the reservoir extending further in this direction.

The heating and renewal of the modern mush system, which can be divided into shallow (5–8 km) and deep (8–12 km) portions, is driven by mafic intrusions from the mantle (Barker et al., 2015). Holocene melt inclusions indicate variation between mantle melting regimes beneath and between calderas (Barker et al., 2020). The melt inclusions highlight subduction-related flux melting beneath calderas, whereas intercaldera melting is driven by decompression (Barker et al., 2020). This variable melting is supported by seismic imaging, revealing large spatial discontinuities consistent with variable fluid-flux emanating from the subducting slab (Eberhart-Phillips et al., 2020). Based off their volcanic and geothermal outputs, four to ten times as much mafic melt is intruding beneath TVZ calderas, sustaining the large silicic reservoirs (Barker et al., 2020).

Evidence of mafic recharge is reflected in the distribution of the 2019 seismicity, which occurred between 7–9 km and 11 km depth (Illsley-Kemp et al., 2021). These distributions are likely reflecting magma ponding, caused by the density contrasts between the two mush zones (Bain et al., 2013; Illsley-Kemp et al., 2021). The lineations of earthquakes are therefore defining the intersection of the two mush zones and the intersection

of the lower mush zone with the deep mafic feeder zone.

1.3.2 Magma-tectonic interactions at Taupō

Faulting and other dynamic stress changes are common around calderas, having the potential to interact with their complex magmatic systems and impact on eruptive behaviour (Buck et al., 2006; Baer et al., 2008; Biggs et al., 2011). An example of this is Long Valley caldera in California, where favourable stress conditions created by shallow normal faulting allowed eruption to occur in 1350 AD (Mastin & Pollard, 1988; Bursik et al., 2003). Additionally, sequential tapping of separate magma bodies during the 2.1 Ma eruption at Yellowstone caldera also suggests a potential tectonic trigger (Myers et al., 2016). Volcanic triggering is also seen at the Afar Rift in Ethiopia, with regular dike intrusions occurring every 1–9 months depending on changes in the regional stress regime (Belachew et al., 2011).

Major eruptions at Taupō caldera similarly display evidence of tectonic interaction, particularly the Oruanui supereruption. Pumice clasts sampled from Oruanui fall deposits are split into biotite-free and biotite-bearing, with the biotite-bearing clasts depleted in Zirconium and Hafnium (Allan et al., 2012). These depletions match biotite bearing clasts from NE-dome magma erupted 1 kyr prior, with trace element concentrations from amphibole crystals further confirming this (Sutton et al., 1995; Wilson & Charlier, 2009; Allan et al., 2012). It is suggested the biotite-free and biotite-bearing magmas were united when magma from the NE-dome reservoir was intruded laterally through diking (Allan et al., 2012). This suggests that the Oruanui eruption was immediately preceded and initiated by a tectonic event. These controls further impacted on the Oruanui eruption phases, with the stress drop caused by the initiating dike temporarily closing the erupting vent (Allan et al., 2012). Phase two deposits mirror the first phase, suggesting another rift-related dike restarted the eruption once sufficient stress rebuilt (Costa et al., 2011). This indicates the regional stresses in the Taupō Rift exerted strong controls over the Oruanui eruption.

While evidence for regional tectonics driving eruptions is most clear during the Oruanui eruption, it can be inferred for other Holocene eruptions in the TVZ. Following the Oruanui eruption, rhyolitic eruptions in the TVZ vary significantly in eruptive volume, with no significant correlation to the repose time between events (Wilson, 1993). This indicates that the steady accumulation of magma within the silicic system is not solely responsible for eruptions, suggesting a more complex triggering mechanism.

Understanding of this interplay is limited and is a key concept investigated in this research. Determining the likelihood of Taupō erupting is of paramount importance and based on previous eruptions can be determined by three independent factors. These are: the potency of the deep mafic feeder system, the potency of the shallow silicic system and the tectonic stress state around calderas in the central TVZ (Rowland et al., 2010). The three factors can be quantified by mafic magma-static pressure, the tendency for a percentage of the silicic system to undergo partial melting and crustal differential stress (Rowland et al., 2010).

The interplay and intensity of these factors is critical to the activity and outcome of unrest at Taupō Volcano. High levels of all three stresses would likely result in a large-scale caldera eruption, although such scenarios are rare as the factors are co-dependent (Rowland et al., 2010). For example, mafic magma pressure limits local differential stress by accommodating extension without faulting (Buck et al., 2006; Rowland et al., 2010). However, this can then increase pressure on the silicic system, which can induce inflation-based faulting (Simakin & Ghassemi, 2010). The nature of the silicic system is heavily influential, with inflation of the magma reservoir or the encapsulation of intruding dikes often resulting in changes in the differential stress fields on surrounding faults (Rowland et al., 2010; Simakin & Ghassemi, 2010). It has also been demonstrated that the motion on normal faults or stress changes due to rifting can impact the activity of the silicic system (Acocella et al., 2015).

1.4 Unrest at Taupō

Seismicity is common at Taupō, and primarily occurs as swarms of low magnitude (M<0–2.5) earthquakes, which forego a typical foreshock-aftershock pattern. Despite this pattern, larger events are also known to occur at Taupō, such as the M 5.3 event on the 4th of September in 2019 (Illsley-Kemp et al., 2021). Determining the origin of these swarms as magmatic or tectonic is key, as the former can be used to infer inflation or migration of the magma reservoir below (Charlton et al., 2020). With this goal in mind, reviewing the history of unrest in the Taupō area is imperative. Seismicity at Taupō can be separated into before and after 1985, when seismometer coverage around the lake began to improve. In addition to poor instrument coverage, the ignimbrite deposits covering the region are poorly consolidated and tend to enhance attenuation of seismic signals (Henrys & Hochstein, 1990; Bannister, 1992; Dowrick, 2007; Rowland et al., 2010). As a result, earthquake locations prior to 1985 lack confidence (Sherburn, 1992a,b; Otway & Sherburn, 1994).

1.4.1 Pre-1985

The earliest felt reports in the region date back to 1895 with a swarm of earthquakes lasting approximately 6 weeks (Eiby, 1966). The largest event produced a level of surface fracturing which suggested a magnitude of 6–7.5 (Eiby, 1966; Grindley, 1986). It is unclear whether this event was of tectonic or magmatic origin, but the inferred magnitude suggests the potential for significant unrest in this region.

This was followed by the 1922 seismic earthquake swarm, which is the earliest recorded seismic earthquake swarm in New Zealand (Eiby, 1966). Seismicity during this period began approximately 50 km northeast of Taupō and migrated south, accompanied by ground shaking and normal faulting (Potter et al., 2015). Deformation was widespread throughout the Taupō Fault Belt, with ruptures up to 3 km in length observed on the Kaiapo, Whakaipo and Whangamata faults (Peltier et al., 2009). Subsidence on a metre scale was also observed and was exaggerated in the western side of the Whakaipo fault (Hull & Grindley, 1984). While this swarm was likely due to mechanical faulting, the large displacements relative to the small magnitudes of the events suggests a component of aseismic magma deformation (Barker et al., 2021).

Prior to 1985, two more periods of moderate unrest were identified, the first lasting only a month in December 1964 (Potter et al., 2015). The high frequency of volcano-tectonic earthquakes in this swarm combined with the typically aseismic location at Taupō's western bay indicate this unrest was associated with magmatic activity (Potter et al., 2015; Barker et al., 2021).

The second period of moderate unrest was between October 1982 and June 1983, with two major swarms in February and June (Potter et al., 2015). Lake levelling studies indicate that during this unrest Kinloch was uplifted by ∼43 mm, with a further 11 mm of uplift recorded at the eastern lake shore (Otway, 1986). Seismicity later migrated towards the Horomatangi Reefs, coinciding with 55mm of subsidence on the hanging-wall of the Kaiapo Fault and 10mm of uplift on its foot-wall (Otway et al., 1984; Otway, 1986; Webb et al., 1986; Wilson, 1993). These observations together suggest a portion of this unrest period was associated with magmatic processes (Potter et al., 2015; Barker et al., 2021). The largest earthquakes during this period (∼M4.3) ruptured the Kaiapo Fault in the same location as in 1922 (Hull & Grindley, 1984; Otway et al., 1984). This shows a trend developing with both the 1922 and 1983 swarms displaying uplift, rupturing on the Kaiapo fault followed by regional subsidence on its western side (Grindley, 1986; Peltier et al., 2009; Potter et al., 2015). This suggests that in both cases the Kaiapo and Whakaipo faults were accommodating the bulk of extension.

1.4.2 1985 Onwards

In 1985 a six-station network of seismometers was deployed around Lake Taupō (Sherburn, 1992b; Barker et al., 2021). This greatly improved the ability to monitor unrest, reducing the dependence on temporary research arrays. Since deployment, four episodes of 'minor' unrest (1996 – 1999, 2001, 2008 and 2019) have been recorded (Potter et al., 2015; Illsley-Kemp et al., 2021)). In addition to these unrest periods, in 1987 the M 6.3 Edgecumbe earthquake occurred near the Bay of Plenty (Grapes et al., 1987; Barker et al., 2021). This event ruptured the Edgecumbe Fault and is the largest recorded onshore earthquake associated with the Taupō Rift (Beanland et al., 1990), indicating of the potential of the Taupō Rift to produce large tectonic events.

The first period of unrest in 1996 began with approximately 40mm of uplift at Horomatangi Reef, with seismicity increasing following this (Potter et al., 2015; Peltier et al., 2009) (Figure 1.6A). This uplift was attributed to an inflating magma source beneath the reef (Peltier et al., 2009). There was no discrepancy in motion either side of the Kaiapo fault as seen in 1922 and 1983 (Peltier et al., 2009).

Unrest occurred again between December 2000 and June 2001 and involved a minimum of three hydrothermal eruptions at Wairakei Geothermal Field (Potter et al., 2015; Barker et al., 2021). This unrest was focused in the Taupō Fault Belt (Figure 1.6B), specifically around the Kaiapo Fault (Otway, 1980, 1989; Otway & Sherburn, 1994; Otway et al., 2002; Peltier et al., 2009). However, earthquakes during this unrest period have not been located accurately enough to confirm which fault they occur on, making it unwise to attribute all activity to the Kaiapo Fault. Following this unrest, asymmetrical deformation occurred to either of the Kaiapo Fault, with uplift to the east and subsidence to the west (Peltier et al., 2009). However, only 67% of vertical displacements over this period can be explained by normal motion on the Kaiapo Fault and no ruptures were observed (Peltier et al., 2009).

Minor unrest in 2008 was recorded between Motutaiko Island and Karangahape Cliffs (Figure 1.6C), in addition to 40–50mm of uplift observed at Horomatangi Reef (Potter et al., 2015; Barker et al., 2021). The spatial distribution of the swarm is oriented parallel to the Taupō rift and close to the negative gravity anomaly inferred as the Oruanui collapsed caldera (Davy & Caldwell, 1998; Barker et al., 2021). This swam is thought to have been triggered by a tectonic slow-slip event, however considering its location within the caldera it is likely the magmatic system also played a strong influencing role (Fournier et al., 2013).

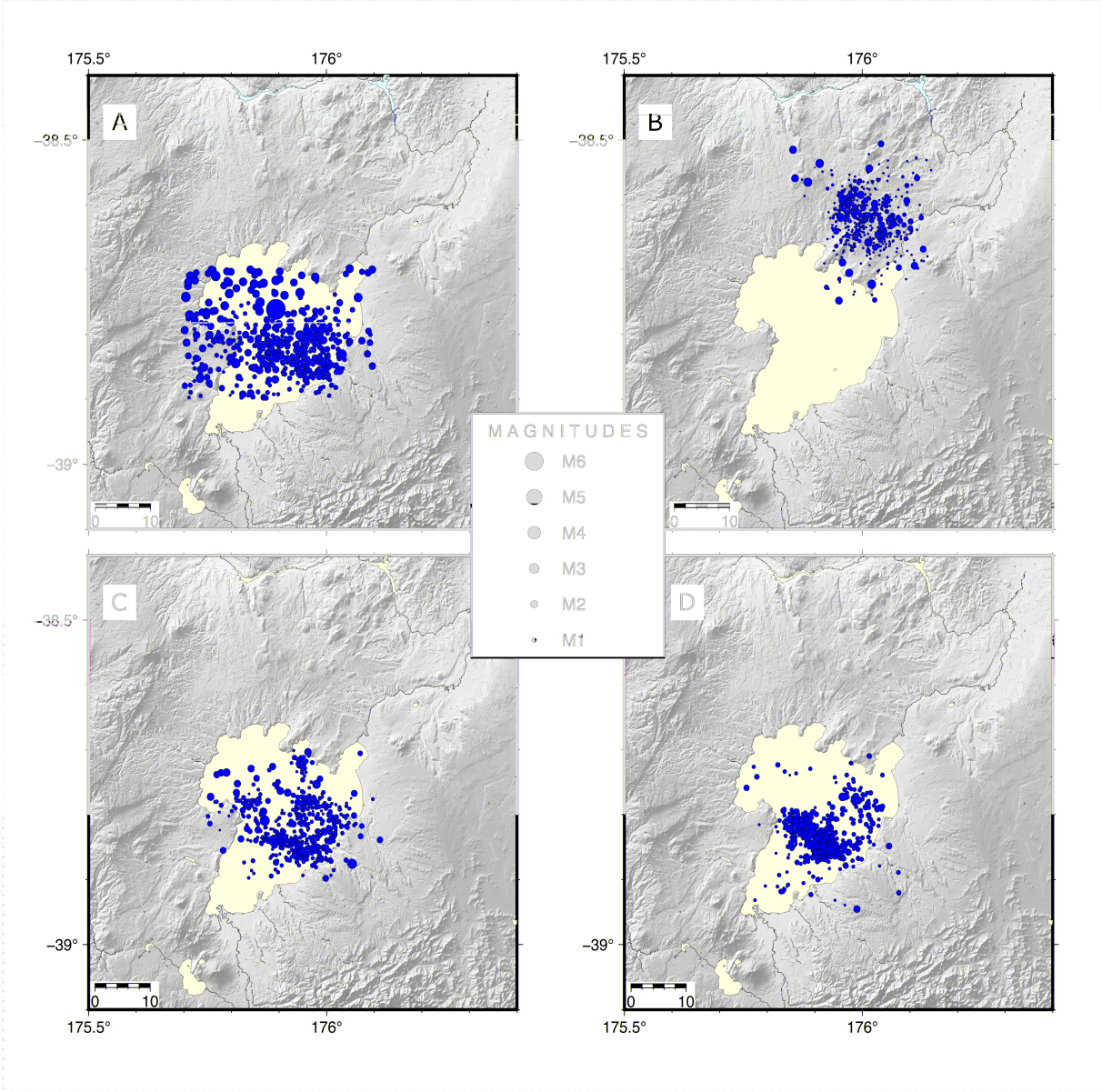

Figure 1.6: Instrument recorded periods of unrest since 1985 as identified by Potter et al. (2015). Earthquakes are shown as red circles and are scaled to magnitude. Where magnitude data is not available, magnitudes have been adjusted to 1.0 although this is only an issue for the 2001 swarm. All information was taken from GeoNet. The timeframes are A: 01/03/1996–01/03/1999, B: 01/01/2001–01/07/2001, C: 24/03/2008–30/09/2008, D: 01/06/2019–29/09/2019. Figure adapted from Barker et al. (2021), but plotting only earthquakes in the respective swarms.

The most recent recorded period of unrest occurred 10 years later in 2019 (Figure 1.6D (Illsley-Kemp et al., 2021)). This unrest was separated into seven swarms, with the first swarm occurring beneath the southern lake and displaying focal mechanisms and spatial distribution consistent with extensional faulting (Illsley-Kemp et al., 2021). The second swarm, also situated in the southern Lake Taupō, showed similar characteristics to swarms resulting from the ascent of magma or fluid along existing faults (Hayes et al., 2004; Bannister et al., 2016; Reyners et al., 2007). The other five swarms show little evidence of slip or fluid motion occurring on any fault planes and are distributed between Karangahape Cliffs and Motutaiko Island (Illsley-Kemp et al., 2021). The spatial distribution of these swarms is similar to the 2008 unrest, suggesting they are also related to the underlying magma chamber. Additionally, most events during this unrest period are best explained by non-double-couple focal mechanisms, which are inferred to result from the movement of magma (Clarke et al., 2019; Illsley-Kemp et al., 2021).

To summarise, there are two distinct patterns in the distribution of seismicity around Taupō, although we are more confident in these for events after 1985. The majority of recorded earthquake swarms occurred beneath Lake Taupō and were centred around Horomatangi Reef. By contrast, the 2001 swarm is dominated by events distributed within the Taupō Fault Belt, aligning closely with major fault lines. While this is the only recorded swarm to have occurred in the fault belt, the 1922 swarm and the first swarm in the 1983 unrest period resulted in rupturing of faults in this area. This suggests that earthquakes occurring during 1922, 2001 and the early portion of 1983 are the result of slip on faults in the Taupō Fault Belt. By comparison, the unrest in 1996-99, 2008, 2019 and the latter half of 1983 were more likely associated with the magma reservoir beneath Taupō. It should be noted that earthquake activity beneath the lake is concentrated towards the eastern shore, with Taupō's Western Bay being historically aseismic (Potter et al., 2015; Barker et al., 2021).

1.5 Thesis structure

This thesis consists of four chapters, the contents of which are summarized below.

- **Chapter 1: Introduction**
  This chapter is separated into three parts. The first section (Section 1.1) outlines the motivations behind this research and why it centres on Taupō in 2001 before summarising our research objectives. The second section (Section 1.2) provides a

geological background, focusing on the evolutions of the Taupō Volcanic Zone and the Taupō Rift. The final part of this chapter outlines the modern conditions at Taupō (Section 1.3) and the history of recorded unrest in the area (Section 1.4).

- **Chapter 2: Methods**

  This chapter consists of two parts, the acquisition and processing of the earthquake data. The first part of the chapter (Section 2.1) provides a summary of the two research arrays used, briefly commenting on the formatting issues we initially encountered. Then the methodology used to derive our high resolution earthquake locations from the raw time-series data is outlined (Section 2.2). This is separated into five parts, outlined in a flow diagram. In the first subsection we describe the process of manually picking phase arrivals for our template events, before detailing the technique and parameters for detecting new earthquakes during the swarm. The third part of this chapter outlines the technique used to derive absolute locations for these detections. The theory and program parameters utilised for accurately relocating the detections are detailed in the fourth subsection, before the chapter is concluded with a description of the magnitude and focal mechanism calculation process.

- **Chapter 3: Results**

  Chapter 3 outlines the results of data processing. This begins with a description of the error associated with the location and relocation process (Section 3.1) before a brief look at the locations of the template earthquakes (Section 3.2). Following this, the spatial and temporal distributions of the earthquakes after matched-filter detection and GrowClust relocation are outlined (Sections 3.3 & 3.4). This is accomplished primarily through map and cross-section representation. We also present the focal mechanism calculations for six higher magnitude events from the swarm (Section 3.5).

- **Chapter 4: Discussion & conclusions**
  In the final chapter we discuss the interpretation of the results from the previous chapter. This centres around the identification of relocated seismicity occurring beneath Lake Taupō's previously aseismic Western Bay (Section 4.1), which we believe represents magmatic intrusion. We also introduce further lines of evidence to support this, both from Taupō and other caldera settings (Section 4.2). Finally, we consider how the relocation of the 2001 earthquake swarm at Taupō is contextualised within the larger magma-tectonic interactions of the Taupō Vol-

canic Zone before concluding on these interpretations and recommending areas of potential future research (Sections 4.3 & 4.4).

Chapter 2

Methods

This chapter consists of a description of how we acquired the dataset and processed it to obtain the desired results. This began with retrieving time-series data from two research arrays deployed during between January and June 2001 and converting the data into the required miniSEED format (Section 2.1). This is followed by an outline of the methods used to process the miniSEED data for spatial, temporal, magnitude and focal mechanism analysis of the swarm (Section 2.2).

2.1 Data acquisition

As the Taupō Fault Belt seismicity occurred in 2001, the national GeoNet seismometer coverage was not as comprehensive as it is currently. Earthquake waveform data downloaded from GeoNet is also in a triggered format. This records snippets each time an earthquake is identified and would restrict identification of earthquakes missed by GeoNet. Considering these constraints, we are utilising two research arrays set up as part of academic studies. These arrays record continuous data and are better suited for detecting new events. Using two temporary arrays produced a more comprehensive spread of stations around the Taupō Fault Belt (Figure 2.1).

2.1.1 CNIPSE array

The CNIPSE or Central North Island Passive Seismic Experiment array (Figure 2.1, blue) was deployed in 2001 from the 8th of January to the 27th of June (Henrys et al., 2003). This array was part of an international effort to produce a detailed 2-D

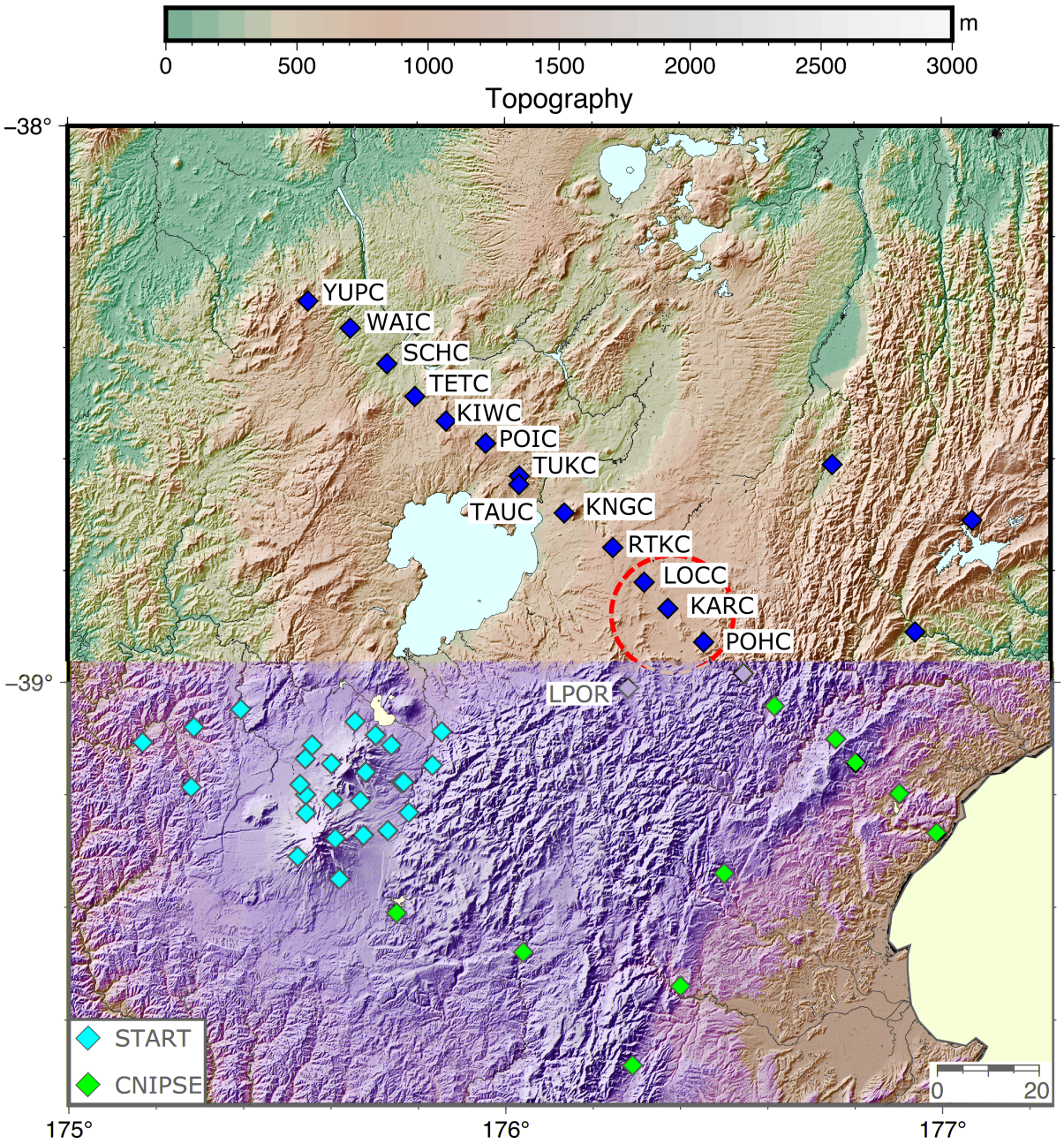

Figure 2.1: Station map of seismometers used for data acquisition. We used two research arrays, the Central North Island Passive Seismic Experiment array (CNIPSE array, blue) and the Seismic Tomography Around Ruapehu and Tongariro array (START, purple). Problematic stations have been circled in red. Central CNIPSE stations have been labelled.

picture of the shear wave structure of the subducted and overlying plates in the central North Island (Henrys et al., 2003). This study was a major collaboration between the Institute of Geological and Nuclear Sciences, the University of Leeds and Victoria University of Wellington (Henrys et al., 2003). Data from the CNIPSE array was later incorporated into modelling of the crustal and upper mantle velocity structure of the TVZ (Harrison & White, 2006).

The CNIPSE array consisted of 74 total stations (32 broadband, 42 short-period), including a mixture of ORION and REFTEK sensors (Reyners & Stuart, 2002). A subsection of these recorded relevant data, most notably the line of 18 stations deployed down-dip of the subducted plate (Reyners & Stuart, 2002), Figure 2.1). Stations along this line had a uniform spacing of 10 km and were housed in 600 mm-deep pits on cement slabs to remain level (Reyners & Stuart, 2002). In practice these worked well, keeping stations correctly oriented and dry (Reyners & Stuart, 2002).

The ORION recorders contained a 1 Gb data cartridge and were serviced at monthly intervals to guard against any data loss (Reyners & Stuart, 2002). The REFTEK stations had a larger storage capacity (4.3 Gb), which took ∼83 days to fill and were therefore serviced less frequently (Reyners & Stuart, 2002).

The CNIPSE array was deployed concurrently with the estimated length of our earthquake swarm, from the 1st of January until 26th of June (Figure 2.2). This combination of spatial and temporal proximity to the Taupō Fault Belt seismicity makes the CNIPSE array well positioned for detecting lower magnitude earthquakes. The precise locations of the CNIPSE stations can be seen in Table 2.1.

There were some issues with the deployment of the CNIPSE array which should be noted. Due to the desired alignment and spacing of the down-dip line, some seismometers were deployed in areas with no competent rock (Reyners & Stuart, 2002). This is reflected in the variation in recording quality, with most stations producing good quality data despite a few notable exceptions on the Kaingaroa Plateau (Figure 2.1, circled stations).

Technical issues were also encountered, with some REFTEK sensors experiencing sporadic one second time jumps (Reyners & Stuart, 2002). This is a known issue with older REFTEK seismometers but was not addressed prior to deployment. However, the time jumps were easily identified and avoided when looking at the time-series data. Additionally, padding the time series data with zeroes to fill gaps mitigated any impact this may have on our processing.

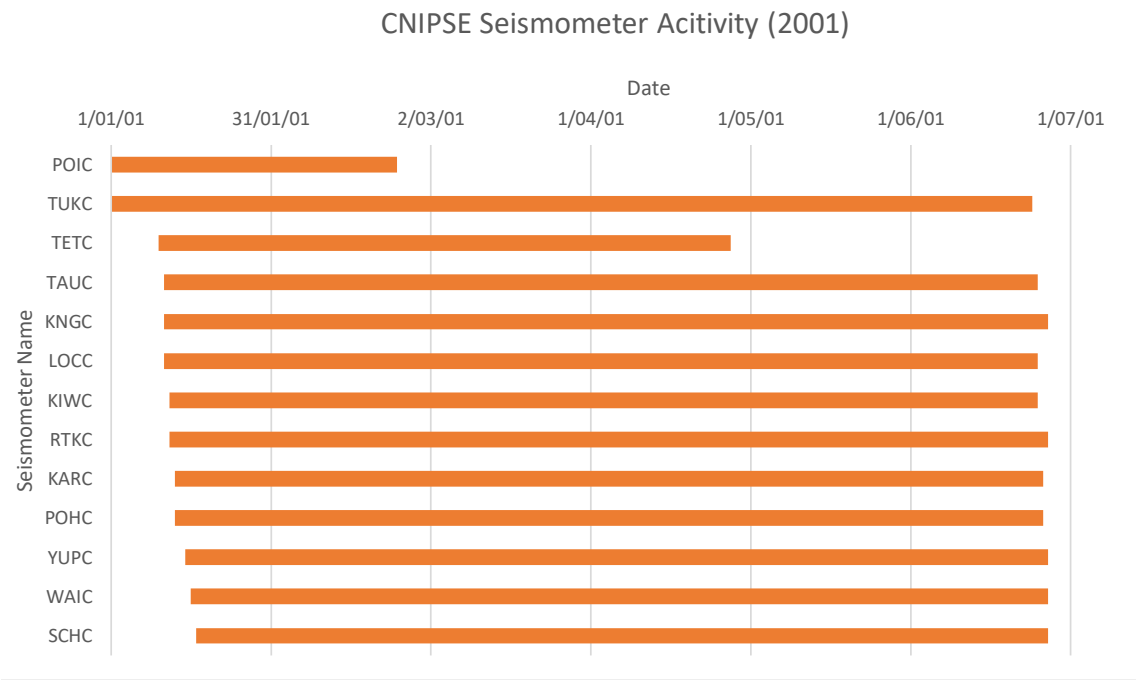

Figure 2.2: Gantt chart displaying the activity of seismometer stations in the CNIPSE array.

Another issue encountered with the REFTEK seismometers was a failure to record data, likely caused by incompatibility between older DAS's (Data Acquisition Systems) and newer disk units (Reyners & Stuart, 2002). Unfortunately, due to the low maintenance requirements of the seismometers, loss of recordings were not identified rapidly, meaning this issue persisted (Reyners & Stuart, 2002). Loss of data was further compounded by weather conditions, particularly during May. Large amounts of fog caused reduced solar power input, exacerbating data loss during this month (Reyners & Stuart, 2002). This issue was more impactful than the sporadic time jumps, creating some compatibility issues during the detection stage of the data processing.

2.1.2 START array

The second source of seismic data was the START (Seismic Tomography Around Ruapehu and Tongariro) array, which consisted of 28 seismometers shipped from the University of Cambridge and Seis-UK (Reyners & Stuart, 2002). The START array was deployed in 2001 from January to June around Mt Ruapehu and operated concurrently with the CNIPSE array (Reyners & Stuart, 2002). The aim of this research was to investigate variations in P-wave velocity in the Tongariro Volcanic Centre, using earthquake locations to indicate a shallowing of the brittle-ductile transition beneath Ruapehu (Reyners & Stuart, 2002).

The START array was installed southwest of the Taupō Fault Belt, near Mount Ruapehu (Figure 2.1, purple). Therefore, it is not expected for smaller magnitude earthquakes in the swarm to be confidently identified on these stations. However, energy from larger magnitude earthquakes in the swarm should be visible, providing increased coverage for our seismometer network. The accuracy of earthquake relocation can increase when using additional stations, although spacing and geometry of the network are also key considerations (Trugman & Shearer, 2017). Therefore it is likely the inclusion of the START array will help increase the quality of the processing results. Unlike the CNIPSE array, all START stations were active for the entirety of our time frame. The precise locations of the stations in the START array can be seen in Table 2.1.

The START array suffered from the same data loss issues as the CNIPSE array. This ranged from recordings stopping after a few hours to complete days of data being lost. There was also variation as to which data was lost. While entire stations of data were lost on some days, individual channels would be lost on others. As with the data from the CNIPSE array, this complicated data processing during the detection phase.

Station	Latitude (south)	Longitude	Elevation (m)
Central CNIPSE			
YUPC	38.316	175.550	540
WAIC	38.365	175.647	340
SCHC	38.429	175.731	260
TETC	38.532	175.866	544
KIWC	38.572	175.957	626
POIC	38.631	176.034	572
TUKC	38.646	176.033	520
TAUC	38.697	176.137	551
KNGC	38.759	176.248	669
RTKC	38.821	176.320	716
LOCC	38.868	176.374	724
KARC	38.928	176.456	773
POHC	38.984	176.544	659
Other CNIPSE			
KNZ	39.023	177.673	32
LDEN	38.488	175.795	451
LGDS	39.268	176.986	37
LGLS	39.101	176.755	525

LJAI	38.610	176.750	381
LKOW	39.340	176.500	431
LMAT	39.680	176.290	524
LMAU	38.910	176.940	209
LMOW	39.410	175.750	880
LOPO	39.143	176.801	526
LPAP	39.198	176.901	198
LPOR	39.010	176.280	696
LRAN	39.480	176.040	591
LTAT	39.042	176.615	522
LWAI	38.710	177.070	609
LWTT	39.540	176.400	354
TOZ	37.733	177.502	85.0
START			
S01	39.200	175.542	1145
S02	39.200	175.542	1145
S03	39.233	175.543	1496
S04	39.112	175.557	982
S05	39.136	175.541	975
S06	39.145	175.601	1215
S07	39.182	175.529	1020
S08	39.310	175.524	1553
S09	39.070	175.655	765
S10	39.272	175.674	1248
S11	39.210	175.604	1359
S12	39.264	175.730	1073
S13	39.094	175.702	833
S14	39.112	175.738	810
S15	39.178	175.760	901
S16	39.232	175.778	940
S17	39.211	175.667	1165
S18	39.160	175.679	1410
S19	39.148	175.832	568
S20	39.080	175.286	268
S21	39.187	175.280	320
S22	39.107	175.169	220

S23	39.278	175.610	1733
S24	39.048	175.393	502
S25	39.088	175.853	556
S26	39.350	175.619	1109
S27	39.178	175.766	830
S28	39.310	175.522	1580

Table 2.1: Summary of the latitude, longitude and elevation data of the seismometer stations in both the CNIPSE and START arrays. The CNIPSE array has been divided into the central straight array (listed based on deployment location) and the more widely distributed stations (listed alphabetically)

2.1.3 Data formatting

Waveform data from each station was acquired in 24-hour increments and originally formatted as Seismic Analysis Code (SAC) files. SAC is a method of formatting data developed at Lawrence Livermore National Laboratory and is designed for the study of sequential signals, primarily time series data (Helffrich et al., 2013). Within the SAC files large quantities of station metadata is stored, including the station network, latitude, longitude, elevation, and depth. This information was used to map our arrays (Figure 2.1).

Utilising the Python package Obspy (Beyreuther et al., 2010), SAC files for both the CNIPSE and START arrays can be read and separated into traces. A loop can then be implemented, extracting the desired information from each station in any of the given SAC files. Identifying where each station is oriented relative to the Taupō Fault Belt is important for accurate data processing, as stations further from the Taupō Fault Belt should see earthquake signals arriving later. Knowing the approximate order in which we expect to see earthquake arrivals on our stations provides a reference when identifying earthquakes.

Following the extraction of station information from the raw data in its SAC format, all seismic waveform data were converted into 'miniSEED' format. While this method of formatting results in the loss of most information beyond time series data, it is more readily compatible with data processing tools. This is accomplished using Obspy,

which combines the SAC files for a given day into one miniSEED file. This allows CNIPSE and START data to be analysed concurrently.

2.2 Data processing

There were five stages of data processing (Figure 2.3, red): identification and phase picking of earthquakes in Snuffler (Heimann et al., 2019) to be used as templates; matched-filter detection using templates via EQcorrscan (Chamberlain et al., 2018); location of the resulting detections with NonLinLoc (Lomax et al., 2000); and differential relocation of detections using GrowClust (Trugman & Shearer, 2017). This relocation process was followed by local magnitude calculation. Aside from this process, we also calculated focal mechanisms for six of the higher M_L earthquakes which occurred during our time frame (Figure 2.3, F1–F3).

2.2.1 Manual earthquake detection

Data processing began with identifying earthquakes in the combined miniSEED waveform files (Figure 2.3). This was done using the Pyrocko application Snuffler, which functions as a seismogram workbench, allowing interactive browsing of seismogram data (Heimann et al., 2019).

Once the miniSEED files are loaded into Snuffler, earthquakes can be identified with an event marker. P and S phase arrivals can then be picked interactively. Each station has three channels of varying orientation, HHN, HHE and HHZ, corresponding to measuring north, east, and vertical motion. The P-phase arrival is taken as the first energy arrival of the earthquake, while the S-phase arrival is determined by the change in amplitude of the waveform as the shear-waves arrive at the seismometer (Figure 2.4).

Defining earthquake phase arrivals is crucial for determining location, as the difference in time between each arrival at a seismometer is a function of distance and velocity. As P-waves have a higher velocity than S-waves, earthquakes occurring at a greater distance will have a greater lag time between their P and S arrivals. The velocity of the rock the seismic waves are passing through will also affect how fast they travel, making this the second key element to consider.

Given we were dealing with approximately 702.4 Gb SAC data, it was unrealistic and inefficient to manually pick every earthquake arrival. Furthermore, closely spaced

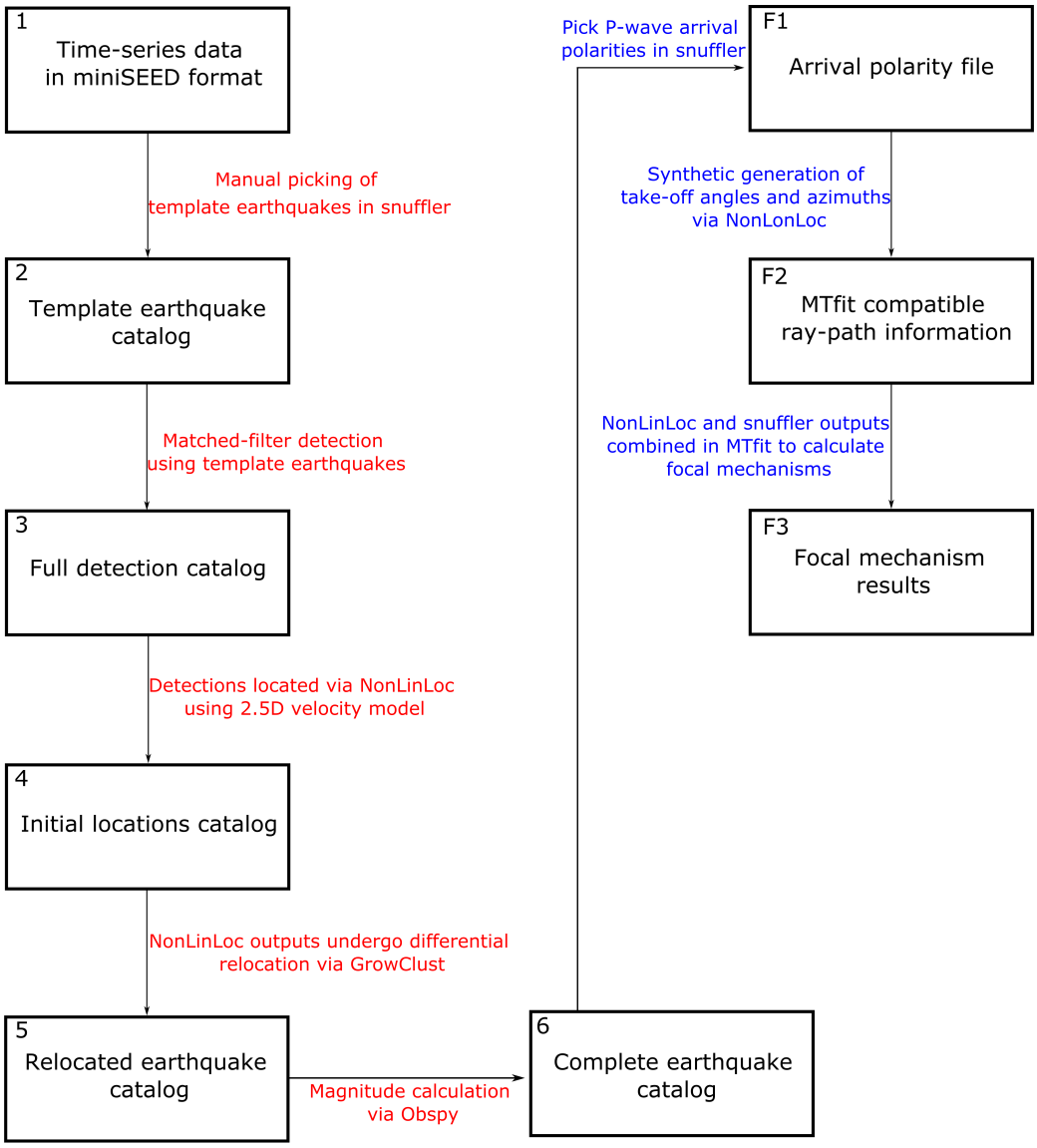

Figure 2.3: A workflow diagram outlining the steps requires to process earthquake data, written in red. This outlines the methodology, as we manually pick template earthquakes in Snuffler and use these to automatically detect the rest of our earthquakes. We then locate these detections using NonLinLoc and use the output files to further relocate as many of these detections as possible in GrowClust. This also shows the secondary workflow for calculating focal mechanisms, labelled F1–F3 and written in blue.

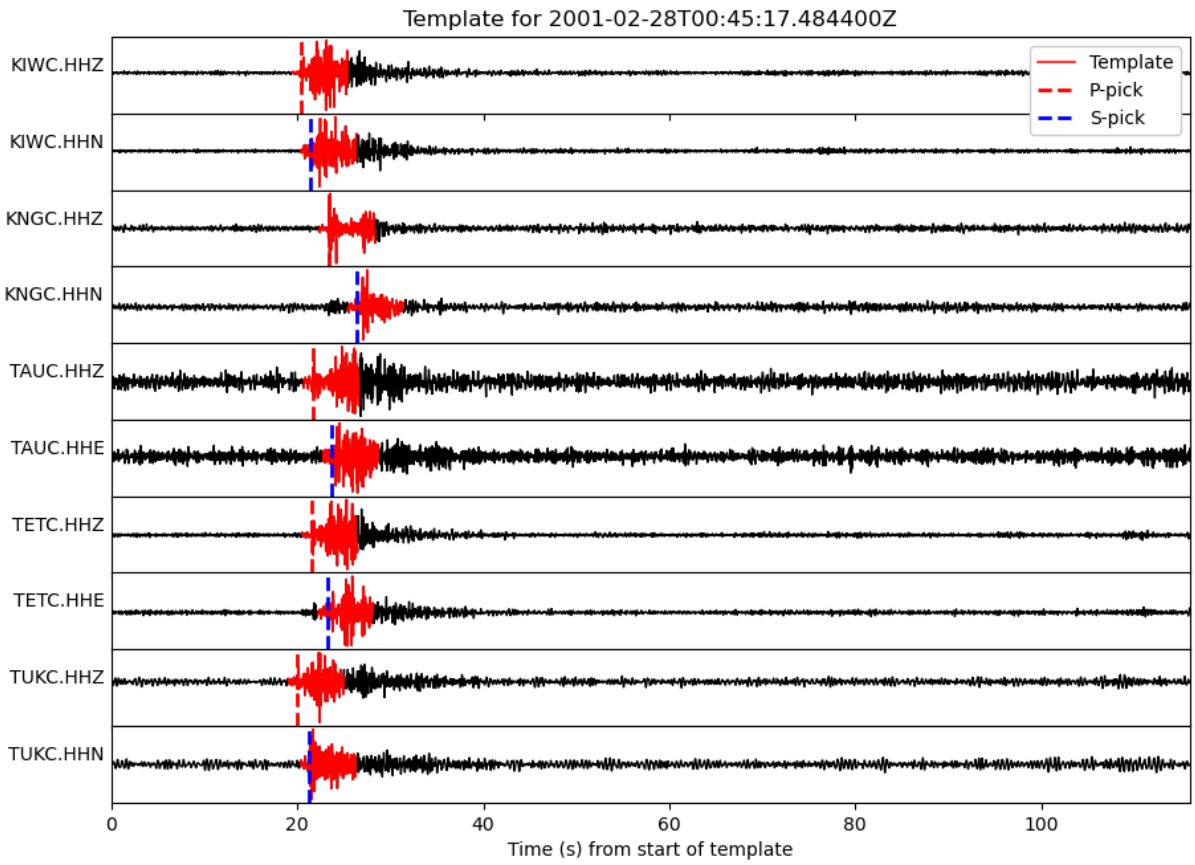

Figure 2.4: A template event picked on 28/02/2001. P-phase arrival picks are shown as red dotted lines while S-phase arrival picks are shown as blue dotted lines. The section of each waveform taken as the template is highlighted red. The Y-axis designates the station and channel the earthquake has been picked on.

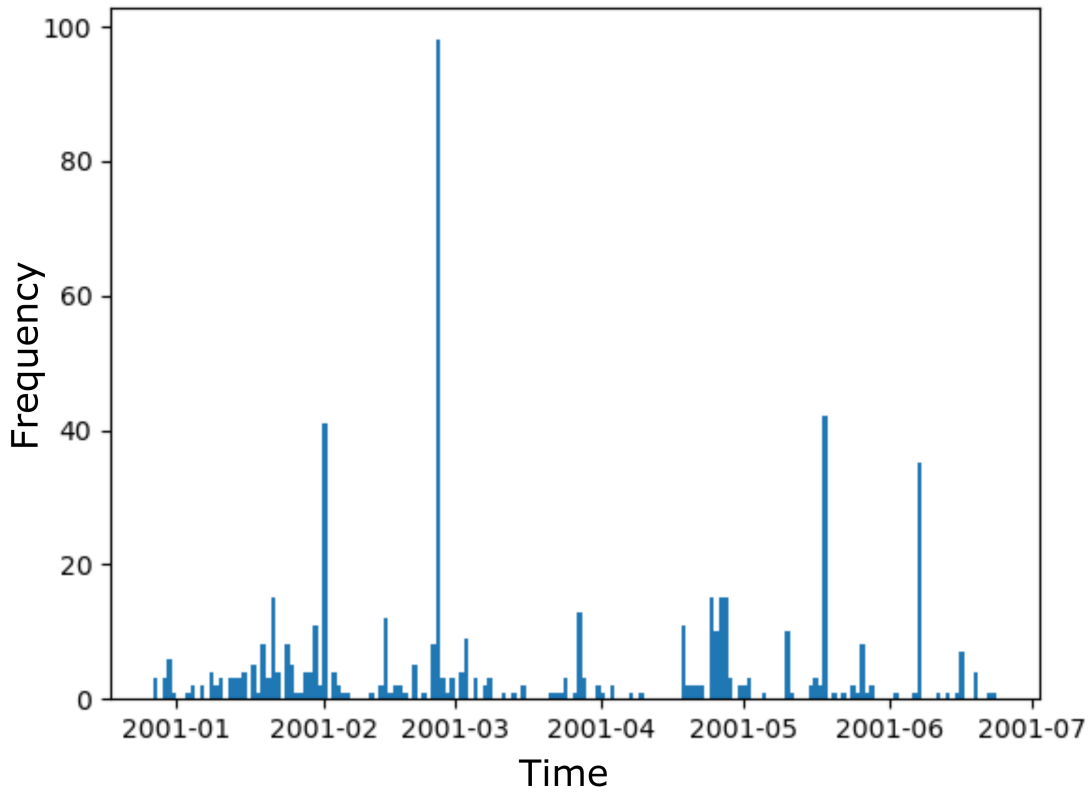

Figure 2.5: Frequency plot of earthquakes occurring during the 2001 unrest in the Taupō Fault Belt as identified by GeoNet. The maximum value was ∼98 earthquakes, recorded on 25/02/2001.

earthquake arrivals proved difficult to pick with a high level of confidence and periods of rapid earthquake arrivals were common. Instead, we focused on developing a catalog comprising well recorded earthquake arrivals to be later used as templates. The primary objective when developing this catalog was to identify earthquakes spread throughout our time frame. Increased variation in these events furthers the likelihood of identifying other earthquakes in the upcoming automated detection (Section 2.2.2). This reduces the possibility of missing events, which may occur if all the templates are closely related in space and time.

Using GeoNet detections as a reference, we identified three days on which significant seismicity occurred during our swarm: the 24th and 25th of February and the 17th of May (Figure 2.5). Earthquakes were identified and manually picked for these days using Snuffler. Additionally, we picked arrivals for every earthquake detected by GeoNet during the swarm which recorded a magnitude ≥ 1. These combined strategies produced a catalog of 529 earthquakes, varying between magnitudes of 0.5–3.5 as calculated by

GeoNet, to be used next in the matched-filter detection process (Section 2.2.2). This catalog comprises a minimum of three events in each month of the swarm and contains only 32 fewer events than GeoNet detected in the entire swarm.

2.2.2 Template matched-filter detection

The second stage of data processing is the detection of new earthquakes using the manually picked Snuffler template earthquakes (Figure 2.3). This is done with the matched-filter detection technique using EQcorrscan (Chamberlain et al., 2018). Due to the nature of our data, with large numbers of earthquakes occurring in quick succession, Snuffler proved unequipped for manually detecting all seismicity during our time frame. Trying to identify events within a swarm can often be difficult due to overlapping waveforms and above average amplitudes masking smaller events (Warren-Smith et al., 2017). To overcome these issues, rather than relying on manual detection or conventional Short Term Amplitude (STA)/Long Term Amplitude (LTA) detection, we used matched-filter detection. Matched-filter detection is estimated to be able to detect signals approximately 0.7 orders of magnitude lower than the smallest possible STA/LTA detections (Gibbons & Ringdal, 2006), ideal for the magnitudes of earthquakes occurring in 2001.

This approach is used to detect earthquakes with similar waveforms and can be exploited to detect other events matching this waveform signature, even those below the usual magnitude detection threshold (Gibbons & Ringdal, 2006). Events are detected when similarity between a template and a continuous waveform stream, summed across all channels, exceeds a correlation coefficient threshold (Warren-Smith et al., 2017). We implemented this method using EQcorrscan, an open-source python package (Chamberlain et al., 2018). EQcorrscan has already been successfully applied to many studies, including detecting aftershocks of the M_L 6.0 Wanaka earthquake in New Zealand in 2015 (Warren-Smith et al., 2017). Within aftershock sequences, events can be missed by energy-based detection due to increased average amplitudes and overlapping waveforms (Warren-Smith et al., 2017). Having assessed this was limiting their ability to detect and analyse the aftershock patterns following the Wanaka event, Warren-Smith et al. (2017) picked 100 events with clear P and S phases from the aftershock sequence to be used as templates. These templates had a wide spatial (up to 8 km) and temporal (up to 26 days following the mainshock) distribution to capture the evolution of the sequence (Warren-Smith et al., 2017). This approach was successful due to the size of the template catalogue and the high degree of waveform similarity typically present in

aftershock sequences (Geller & Mueller, 1980; Gibbons & Ringdal, 2006; Slinkard et al., 2013). As a result, Warren-Smith et al. (2017) were able to detect 2545 earthquakes over the 28 days following the mainshock, 27 times the amount detected by GeoNet.

EQcorrscan gives seismologists the ability to capitalize on the parallel nature of earthquake detection algorithms, applying the matched-filtering technique to continuous waveform data (Chamberlain et al., 2018). EQcorrscan computes normalised cross-correlations between a detection and a single channel in the frequency domain. Correlations for a single-channel normalised coefficient are then aligned based on the relative delays of the template and summed across the channels it is detected on (Warren-Smith et al., 2017). For example, a perfect detection found with a template that included five channels would have a cross-correlation sum of 5, perfectly matching all channels. The equation for computing normalised cross-correlations is shown below (Equation 2.1, taken from Chamberlain et al. (2018)).

$$cc(y) = \frac{(\sum_{x=0}^{n})(t(x) - \bar{t})(d(x+y) - \bar{d}(y))}{\sqrt{\sum_{x=0}^{n}(t(x) - \bar{t})^2 \sum_{x=0}^{n}(d(x+y) - \bar{d}(y))^2}} \tag{2.1}$$

Here 'cc' is the normalised cross-correlation coefficient of the sample 'y'. Additionally, 't' is the amplitude of the template data point, 'd' is the continuous data, '$\bar{d}(y)$' is the local mean of the continuous data between the sample 'y' and the sample '$y+n$', while '$\bar{t}$' is the mean amplitude of the template (Chamberlain et al., 2018).

EQcorrscan parameters

The workflow for this program comprises two main phases, template creation and event detection (Chamberlain et al., 2018). Templates are comprised of trimmed, six second Obspy stream files, with the stream window beginning one second prior to the P-wave arrival pick. Each stream is band-pass filtered, using a low-cut of 1.5 Hz, a high-cut of 10 Hz, a sampling rate of 25 Hz and a filter order of 4. These streams, the coefficient threshold of 8 and a second stream of waveform data to detect against are all required for matched-filter detection (Chamberlain et al., 2018). The EQcorrscan output is a list of detection objects, containing the time of detection and the cross-correlation sum. These can be used in multiple Obspy functions. This use of Obspy classes within the components of EQcorrscan make it simple for the outputs to be used for further analysis, such as relocation (Chamberlain et al., 2018).

EQcorrscan is also able to overcome issues that arise with repeating earthquake data,

such as detections occurring close in time. These could be detections of the same event with different templates. Given the number of templates we are using and the congested arrival of events, this is something we are likely to encounter. To resolve this, repeat detections can be removed by determining which detections occur within a certain time frame (0.5 seconds) of another and then iteratively removing the event with the lowest cross-correlation coefficient until only the event with the strongest correlation is left (Warren-Smith et al., 2017).

Following the matched-filtering process, we produced a catalog of 3873 earthquakes, which were then located in the following section via NonLinLoc. This catalog includes both the 529 templates manually picked and an additional 3344 events identified by EQcorrscan.

Matched-filter challenges

Matched-filter detection proved to be the most time-consuming stage of data processing, due to the high volumes of data involved and the compatibility issues that arose with our data. The size of the combined CNIPSE and START data was approximately 702.4 Gb, which took approximately 30 hours to download and convert from SAC to MiniSEED format.

Compatibility issues were also a major factor, due to the quality and age of the data. While the data from each array were sorted into files for each day, recordings were not uniform in their start and end points. While most streams would span approximately midnight to midnight on each day, some stations would begin their 24 hour recording with a delay and carry on recording into the next day. Given these were the streams used for detection, this produced significant gaps in which possible detections could be missed. To combat this issue, streams of data were read in groups of three, with the target day accompanied by data from the days before and after. This meant any gaps created from formatting issues were solved, as the three days worth of data for each station could be trimmed to only write out the target day. This was done for every day between 11/01/2001 and 30/06/2001.

A second issue was data loss. As mentioned in Section 2.1, stations occasionally had large portions of data missing, sometimes entire channels of data. This produced compatibility issues within EQcorrscan, which automatically pads smaller gaps with zeroes to address such issues. However, this is a temporary solution for small gaps, with the program requiring a minimum of 80% of each stream to be competent data

(not entirely zeroes). Unfortunately, this was not the case on multiple occasions with our data, requiring significant padding to successfully complete detection.

In cases where stations had lost an entire channel-worth of data, padding was not an option. In these cases, the rest of the station data for that day had to be removed, as missing full channels caused a range of input errors with EQcorrscan that could not be resolved. Fortunately, this was not a common occurrence and was limited to stations that were either distant from the Taupō Fault Belt or had been previously noted for producing bad data as a result of their location (Reyners & Stuart, 2002).

2.2.3 Non-linear earthquake location

Following the detection of earthquakes using matched-filter detection, initial locations can be calculated using NonLinLoc (Lomax et al., 2000). This process defines absolute earthquake locations which were later improved by calculating relative locations using GrowClust (Trugman & Shearer, 2017). Location calculation via NonLinLoc is the third stage of data processing (Figure 2.3).

NonLinLoc methodology

NonLinLoc is based on a probabilistic hypocentre location approach, allowing detailed estimations of location errors (Tarantola et al., 1982). The unknown variables, such as the hypocentre coordinates and origin time, are compared with observed earthquake arrivals assuming a theoretical relationship (Lomax et al., 2000). In the case of earthquake location, this relationship is the travel time between earthquake phase arrivals. This can be represented by the following inverse problem adapted from previous works (Equation 2.2, (Poupinet et al., 1984; Shearer, 1997; Waldhauser & Ellsworth, 2000; Trugman & Shearer, 2017)).

$$minimize||r_k|| = ||tt_k - TT_k(m_i)|| \tag{2.2}$$

Here, the objective is to minimise the norm of the residuals (r_k) between the observed and predicted phase arrival times (tt_k and TT_k respectively) from the source (m_i) to a set of seismic stations($_k$). The predicted arrival times (Equation 2.2) are dependent on the velocity structure the seismic waves are travelling through and the hypocentral location of the earthquake, which is dependent on the hypocentral position and the

origin time (Waldhauser & Ellsworth, 2000). The velocity structure is accounted for by an adopted velocity model. Accounting for the four parameters of hypocentral location requires that only events that have phase arrivals picked on four or more stations can be located in NonLinLoc.

Resulting earthquake locations can then be represented as a single, highest probability location (Figure 2.6, green), or as a posterior probability density function (PDF, Figure 2.6, red). These PDFs represent each event as a function of the probability distribution over all possible hypocentre locations (Lomax et al., 2000; Latorre et al., 2016). The significant advantage of using a non-linear location algorithm is the ability to resolve irregular or multi-modal PDFs, due to the non-linear relationship between hypocentre location and calculated travel times (Lomax et al., 2000).

By contrast, the solutions outlined by iterative linear programs only produce a single point solution and all error estimations are made based on the statistics evaluated at this point (Lomax et al., 2000). These are only a good representation if the PDF is assumed to be a near perfect ellipsoid, which is rarely the case (Lomax et al., 2000). This assumption brings risk considering the unique spread of the stations in our research, which contributes to spatial uncertainty in the computed earthquake locations. The alignment of the CNIPSE array produced highly skewed error distributions, with higher location error perpendicular to the array (Figure 2.6, blue diamonds). Due to this, possible hypocentre locations are better constrained parallel to the array than perpendicular. Ideally, an even spread of stations around the area of seismicity could be achieved, allowing observations to be made from all sides and constrain error.

While this network alignment is not perfect, increased resolution parallel to the CNIPSE array is beneficial, as a focus of this research will be identifying the sources of seismicity within the Taupō Fault Belt. Given the majority of faults within the belt strike northeast, minimising error perpendicular to this trend will help differentiate faults. The START array also provided some help in increasing coverage, however as mentioned previously it is too distant for smaller M_L earthquakes to be detected. The primary function of the NonLinLoc location outputs is to be used for differential relocation (See 2.2.4).

NonLinLoc parameters

NonLinLoc operates by searching a velocity grid, which occupies the defined latitude and longitude coordinates of our study region. This is set by inputting the coordinates

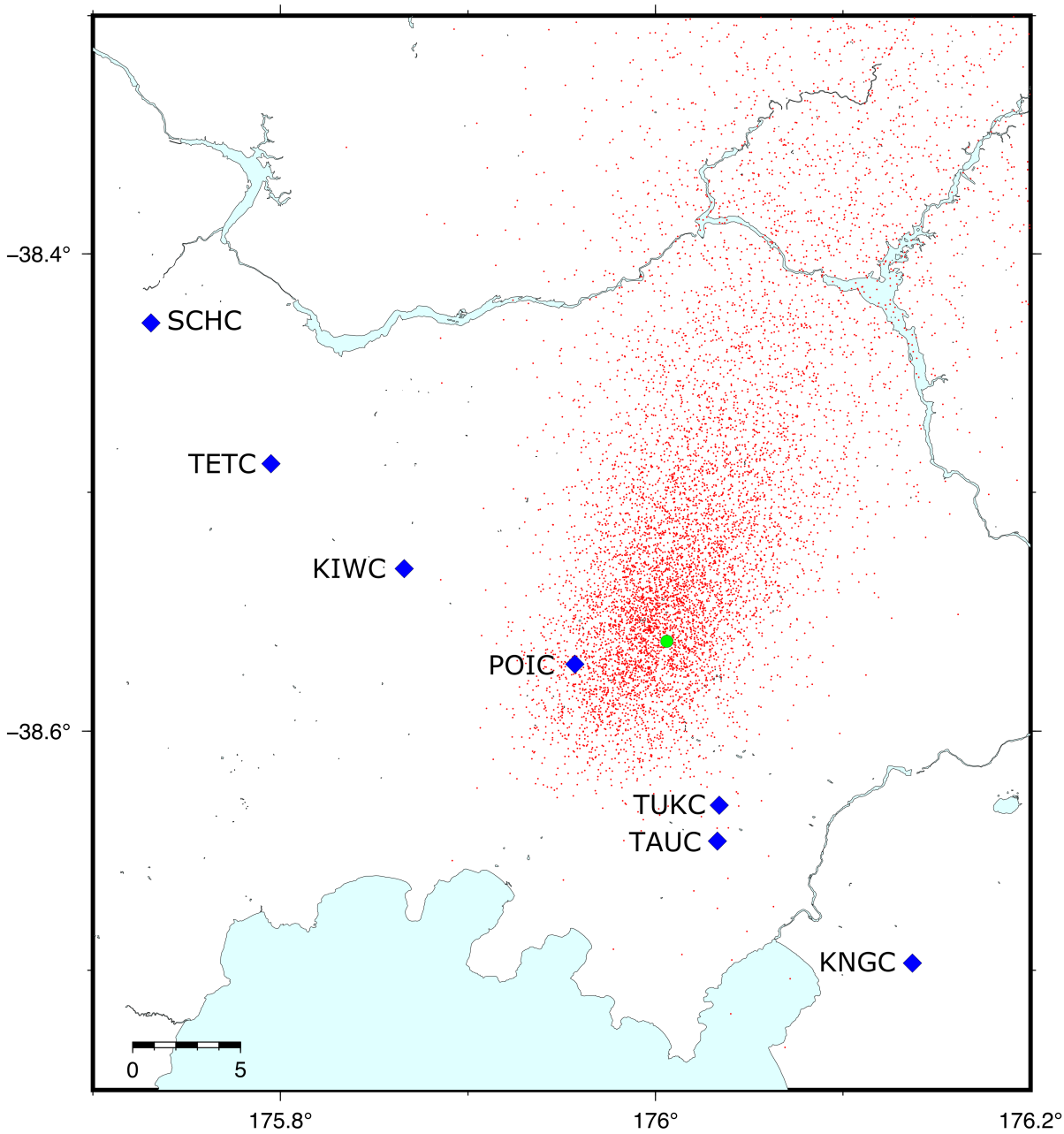

Figure 2.6: A map view showing examples of the outputs from NonLinLoc for a given earthquake, showing both the probability density function (red) and the highest probability location (green). Active faults are shown in black and nearby CNIPSE stations have been labelled.

of the southwest corner of the grid and choosing the number and size of nodes to fill it out. The velocity structure of the grid can then be defined, using either planar layers of changing Vp/Vs values, or building polygons to represent areas of specific velocity (see 2.2.3).

Following the construction of a velocity grid large enough to include all stations, a 3D version of the Eikonal finite-difference scheme is run (Podvin & Lecomte, 1991). This scheme computes the first arrival times of ray propagation, considering the existence of different propagation modes and correctly accounting for sharp changes in velocity contrasts (Podvin & Lecomte, 1991). Generally, computing first arrival times in heterogeneous velocity grids is difficult, as the model receives an unpredictable number of rays at any point, leading to mixing of wavefront information and producing inadequate solutions (Podvin & Lecomte, 1991). However, this is accounted for by NonLinLoc using an algorithm that gives stable recovery of diffracted waves near surfaces with a strong velocity contrast, giving accurate travel times for diffracted waves (Podvin & Lecomte, 1991).

This process creates travel time grid files between every seismic station and the centre of each node in the search grid. This saves time during location, as travel times between an event and any given station can be called directly instead of being calculated in real time. Following this, locations can be determined. Events were taken from the Snuffler pick file, which is converted to an inventory catalog in the QuakeML format. Events from this catalog were converted into phase picks, which are compatible with NonLinLoc and could be located using oct-tree sampling. Oct-tree sampling utilises recursive subdivision of the velocity grid (Lomax et al., 2000). Here the 3D grid is initially divided into cells and sampled, with the probability of an earthquake location being within one of these cells approximated by Lomax et al. (2000), Equation 2.3).

$$P_i = V_i PDF(x_i) \tag{2.3}$$

Here, V_i is the cell volume, the PDF is the Probability Density Function and x_i is the coordinates of the cell centre (Lomax et al., 2000). The resulting probability values are listed in size order and subsequently the cell with the highest probability is subdivided and sampled in the same process (Lomax et al., 2000). This subdividing and sampling process repeats itself until one of two previously defined values is met; either the minimum cell size is achieved, or the algorithm reaches the maximum number of sampling runs without achieving the minimum cell size. The first option is more desirable, as it indicates that a suitable resolution of the PDF was achieved. An

advantage of the oct-tree approach is the sampling cascade will follow the highest PDF value, meaning areas of higher location probability are more densely sampled (Lomax et al., 2000). The sampling spread will therefore approximate the shape of the PDF (Figure 2.6, red). The final highest value cell can also be taken as the highest probability hypocentre (Figure 2.6, green), which can be more appropriate when dealing with large numbers of earthquakes.

Velocity model

Earthquake location via NonLinLoc can be achieved using either a 1D or 2.5D velocity model. A 1D model characterises velocity as a function of depth, assuming no lateral variation (Figure 2.7, bottom). Given the complexity of the subsurface in the central Taupō Rift and our emphasis on high resolution earthquake location, we have chosen to construct a 2.5D model (Figure 2.7, top). This more complex model was adopted from the results of seismic imaging in the area by Stern & Benson (2011) as part of the Mantle of Crust (MORC) project via the North Island Geophysical Transect (NIGHT) array.

Specific Vp values were lifted from the Stern & Benson (2011) model and used to map out a 2D velocity model in NonLinLoc (Figure 2.7, top). This model is comprised of 21 separate polygons, each with defined Vp values and gradients from Stern & Benson (2011), which were then assembled to form a 2D model. Having accounted accurately for subsurface variation across the Taupō Rift, the model is projected in the Y-plane (Venegas, 2011). This converts the 2D model into a 2.5D model. Ideally, we would not have to assume constant velocity values parallel to the rift, but subsurface variation is higher perpendicular to the rift and it is more important to constrain this axis.

The 2.5D velocity model is shown to be significantly more complex than the alternative 1D model (Figure 2.7). It follows a similar pattern of low Vp values (2–3 km/s) in the upper 2 km of the crust but indicates the low-velocity portion of the central Taupō rift (∼95-148 km, Figure 2.7, top) extends significantly deeper than in the 1D approximation. The 2.5D model suggests that lower Vp values are more appropriate, with a layer of 6 km/s rock extending down to approximately 35 km depth. By contrast, no layer with a Vp of 6 km/s exceeds 15 km depth in our 1D model. Additionally, the 2.5D model does not exceed a velocity value of 8 km/s, unlike the 1D layered model, which increases to >9 km/s below 60 km depth. These factors, combined with the clear improvements in accounting for the velocity structure of the Taupō rift suggest the 2.5D model is more appropriate.

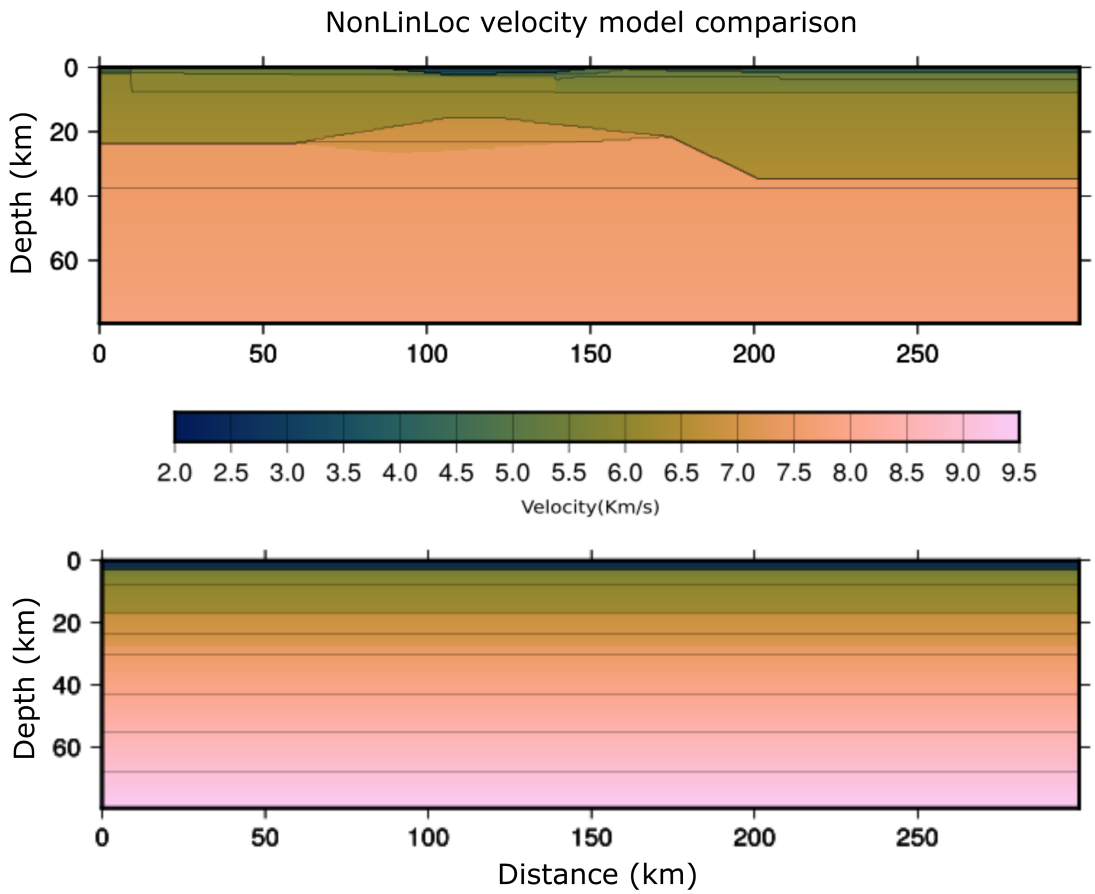

Figure 2.7: Vertical cross-sections of the 2.5D model used by NonLinLoc and of an alternative 1D velocity model for comparison. The cross-sections run across the Taupō Rift, adjacent to the CNIPSE array. In the 2.5D model (top), the low velocity basin (dark blue) marks the centre of the rift and the 7 km/s structure beneath is it the corresponding rift pillow. The 1D model (bottom) assumes no lateral variation in velocity. Values for both models were adopted from Stern & Benson (2011).

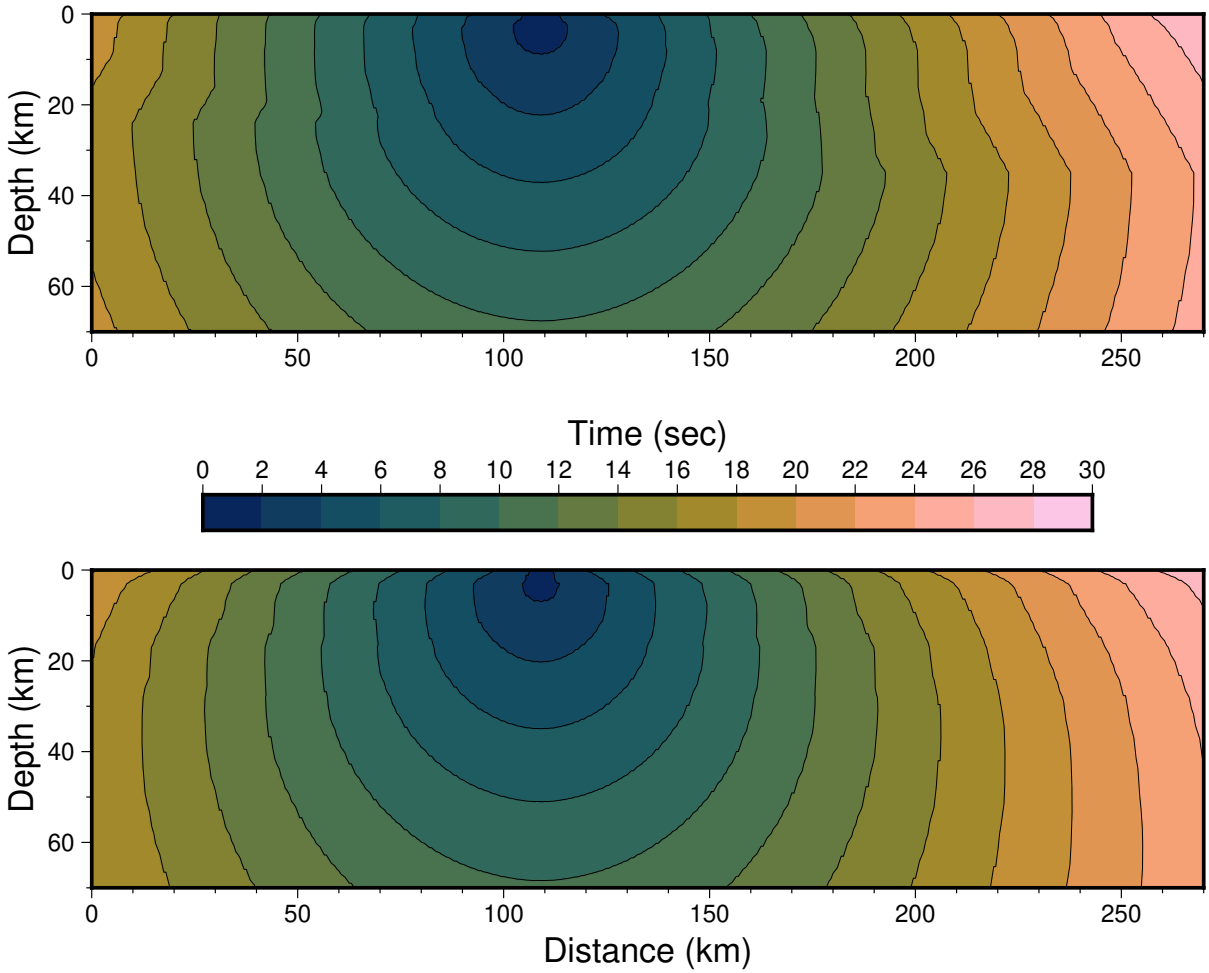

Figure 2.8: The two subplots both show cross-sections of travel time grids calculated by NonLinLoc using the CNIPSE station 'KIWC'. The top subplot uses the new 2.5D velocity model we have constructed, while the bottom subplot uses an alternative 1D velocity model.

The differences between the 2.5D and the 1D model are further reflected in the travel time grid files created for each of our seismic stations. travel time plots from the CNIPSE station KIWC (Table 2.1) indicate the 1D model shows a uniform distribution, due to the simplicity of the layered model (Figure 2.8, bottom). The structure of the 2.5D travel time grid indicates changes in the travel time gradient around the rift pillow structure at ∼24 km depth (Figure 2.8, top). There is also variation seen in the shallow subsurface (0-8 km) which is not mirrored in the 1D grid.

2.2.4 Differential relocation

The absolute locations produced by NonLinLoc typically have a high degree of error associated with them (Thurber, 1983, 1992; Thurber & Eberhart-Phillips, 1999). As

a result, we chose to also calculate relative relocations for all detected earthquakes (Figure 2.3). This is accomplished via GrowClust (Trugman & Shearer, 2017) and is a necessary step to produce the high resolution earthquake locations required for comprehensive analysis of subsurface structures.

GrowClust methodology

The locations produced by NonLinLoc, which were based on absolute phase arrival times, are subject to error given their heavy reliance on velocity structure and accurate phase picks. Despite the use of the 2.5D velocity model, the accuracy of NonLinLoc locations and other location techniques will always be limited by imperfect knowledge of 3D variations in the Earth's structure (Thurber, 1983, 1992; Thurber & Eberhart-Phillips, 1999). Fortunately, computational advances have produced methods that instead work around relative earthquake relocation based primarily on differential travel times of pairs of events observed at common stations (Trugman & Shearer, 2017). These methods extract differential travel times with far greater precision than absolute travel times, resulting in sharper seismicity and resolution of fine scale fault structures (Rubin et al., 1999; Waldhauser et al., 1999; Astiz & Shearer, 2000; Shearer, 2002).

GrowClust is one of these methods of differential relocation, relying on waveform cross-correlation techniques to resolve precise differential travel times from pairs of events as opposed to comparing observed and predicted travel times, as with NonLinLoc (Trugman & Shearer, 2017). This creates a new inverse problem similar to Equation 2.2, but instead attempting to minimise the residuals between the observed and predicted differential travel times for a given pair of events observed at common stations (Equation 2.4, (Trugman & Shearer, 2017)). This equation can be summarised below, where we are trying to minimise the norm of the residuals (dr_k) between the observed (dtt_ij, k) and predicted ($dTT_k(m_i, m_j)$) differential travel times observed at a common station (k). The predicted travel time must account for the sources of both events in the pair.

$$minimize||dr_k|| = ||dtt_ij, k - dTT_k(m_i, m_j)|| \tag{2.4}$$

This method of linking event pairs via differential times allows for the joint inversion of relative hypocentral locations, which is much less computationally expensive than phase arrival based methods (Trugman & Shearer, 2017). This joint inversion also reduces the error affects of unmodeled perturbations in the NonLinLoc velocity model. The differential travel times calculated from cross-correlation can be orders of magnitude

more precise than the absolute travel times calculated from manual arrival picking (Trugman & Shearer, 2017).

Relative relocation is generally based on differential travel times of pairs of events observed at common sites, utilising waveform cross-correlation to produce precise travel times (Waldhauser & Ellsworth, 2000). GrowClust expands on this, inputting differential travel times and cross-correlation into a hierarchical clustering algorithm (Trugman & Shearer, 2017). The GrowClust algorithm then groups seismic events based on waveform similarity and relocates them depending on the other linked events in their group (Trugman & Shearer, 2017).

GrowClust relative relocation operates off the input of NonLinLoc hypocentre phase files, calculating differential travel times and cross-correlation values from obspy using functions within the GrowClust package. These are used to group waveforms based on their similarity and weights data based on the correlation quality, creating a hierarchy within each cluster (Trugman & Shearer, 2017).

The GrowClust clustering and relocation algorithm operates as follows. Events are assigned to an initial starting cluster number, following which a similarity coefficient is computed for each event pair to determine the similarity of the events (Trugman & Shearer, 2017). This similarity coefficient is taken as the sum of cross-correlation values observed at stations common between the two events. Events are then sorted based on the similarity coefficient, moving down the hierarchy with the most similar pairs relocated first (Trugman & Shearer, 2017).

For each new pair there are three circumstances the algorithm must consider. If both events in the pair are highly correlated but members of single-event clusters, the clusters are merged. Both events are then relocated to the centre of this new combined cluster (Trugman & Shearer, 2017). If either of the events are already part of a cluster with multiple other events, the GrowClust algorithm must determine whether to merge the clusters and relocate every event in both clusters relative to each other. If there are enough event pairs that link the two clusters together (the ratio of links to failed links exceeds a pre-set threshold) then the clusters are relocated relative to the ten strongest event pair links (Trugman & Shearer, 2017). This will create a new cluster, with the event locations all in the same position relative to each other, but the centre of the cluster is a combination of the previous two. Finally, if an event pair are shown to belong to the same cluster, GrowClust moves on as these events have already been relocated in one of the previous two scenarios (Trugman & Shearer, 2017). Cluster processing is continued until they can no longer be merged or relocated without returning

values below the correlation threshold.

As previously mentioned, GrowClust is just one of multiple relocation methods, the most widely used approach being the double-difference (DD) method by Waldhauser & Ellsworth (2000). GrowClust acts as an alternative for the double-difference method, firstly aiming to provide a more robust misfit criteria than the L2 norm (least squares) used in standard DD matrix inversions (Trugman & Shearer, 2017). GrowClust instead utilises the L1 norm, which requires no explicit matrix inversion and is less sensitive to input time outliers (Trugman & Shearer, 2017). The L1 norm has been shown in some cases to yield improved results compared to L2-norm solutions (Shearer, 1997). Another issue with the DD method is that inversions can become unstable if the matrix representing the complete solution is not well conditioned, which can occur when correlations between distant event pairs weigh heavily on the inversion (Trugman & Shearer, 2017). By contrast GrowClust applies cluster ideas to decide which event groupings are relocated and which are best left as independent locations, providing greater weight to more highly correlated event pairs. GrowClust uses differential travel times and cross-correlation together in its hierarchical clustering algorithm.

Finally, one of the key powers of GrowClust is the short run time. GrowClust combines the cluster analysis and relocation steps into one process, making less computationally expensive and more suited for large datasets (Trugman & Shearer, 2017). This speed makes it practical to incorporate bootstrap resampling to estimate errors in the model and relocated earthquake hypocentres (Trugman & Shearer, 2017). Previous studies have also shown that, for sequences recorded by a network with inadequate station coverage, locations of clusters can differ on a kilometre scale between GrowClust and double-difference relocations (Waldhauser & Schaff, 2008; Hauksson et al., 2012; Trugman & Shearer, 2017). Given the seismometer coverage at Taupō in 2001, GrowClust's hierarchical clustering suits the research objectives better than double-difference relocation.

GrowClust parameters

For GrowClust to run, the following files must be inputted prior to running the program. Firstly the waveform data for each event to be relocated must be read in and sliced into 6 second clips, which are formatted into a dictionary. A list containing the latitude and longitude information for each seismometer station is also inputted to calculate differential travel times. GrowClust requires a 1D velocity model, made using values from Stern & Benson (2011) (Figure 2.7, bottom). Taking Vp values at regular depths

down the central node of the model produced by Stern & Benson (2011), we inputted a laterally uniform model compatible with GrowClust. The cross-correlation information must also be inputted, which is created using the catalog of detected earthquakes and the dictionary of event streams. During the creation of this cross-correlation file, a bandpass filter is applied, filtering the streams between 1 and 10 Hz. The maximum separation for each cross-correlation pair was set to 8 km, implying that relocation pairs further than 8 km apart are not part same cluster or fault zone. This decision was based on the ∼30 km width of the Taupō Fault Belt and high number of faults within this region.

In addition to inputting a number of files, there are also GrowClust algorithm parameters required prior to relocation. The Vp/Vs ratio is set to 2.0, as taken from Stern & Benson (2011) and was the same value used during the NonLinLoc calculations. The depth parameters for the travel time tables in the algorithm are defined by the commands: tt_dep0=0 (minimum depth in km), tt_dep1=50 (maximum depth) and tt_ddep=1 (depth spacing). These parameters need to encompass the depth range of the swarm. The range parameters (x-axis, in km) for travel time calculations are defined by: tt_del0=0 (minimum range), tt_del1=300 (maximum range) and tt_ddel=2 (range spacing). The range parameters for the width of the travel time search must encompass all the stations in the inputted station list.

Three more GrowClust input parameters must be defined prior to running the program. First the 'rmin', which is the minimum cross-correlation coefficient for differential times used when computing the event-pair similarity coefficients (Trugman & Shearer, 2017). We tested rmin values of 0.25, 0.36, 0.5 and 0.6 in separate GrowClust runs (Figure 2.9).

The distribution of relocated earthquakes is broadly similar across all rmin values (Figure 2.9). All maps show separate, linear clusters of earthquakes occurring within the fault belt accompanied by a circular cluster occurring beneath Lake Taupō. The clusters within the fault belt show good consistency across the different runs, with only some individual events moving short distances. The cluster occurring beneath the lake showed the most inconsistency and is more elongated at rmin values of 0.5 and 0.25 (B & C, Figure 2.9) than in the 0.36 or 0.6 runs (A & D, Figure 2.9).

Based on these comparisons, we decided on an rmin value of 0.5. This was a high enough correlation coefficient to successfully remove outliers and relocate events confidently. This relocated 2729 of the 3783 detected events and was largely composed of clusters containing less than twenty events. However, there were four clusters containing >100 events. Given there was very little spatial variation between GrowClust outputs using

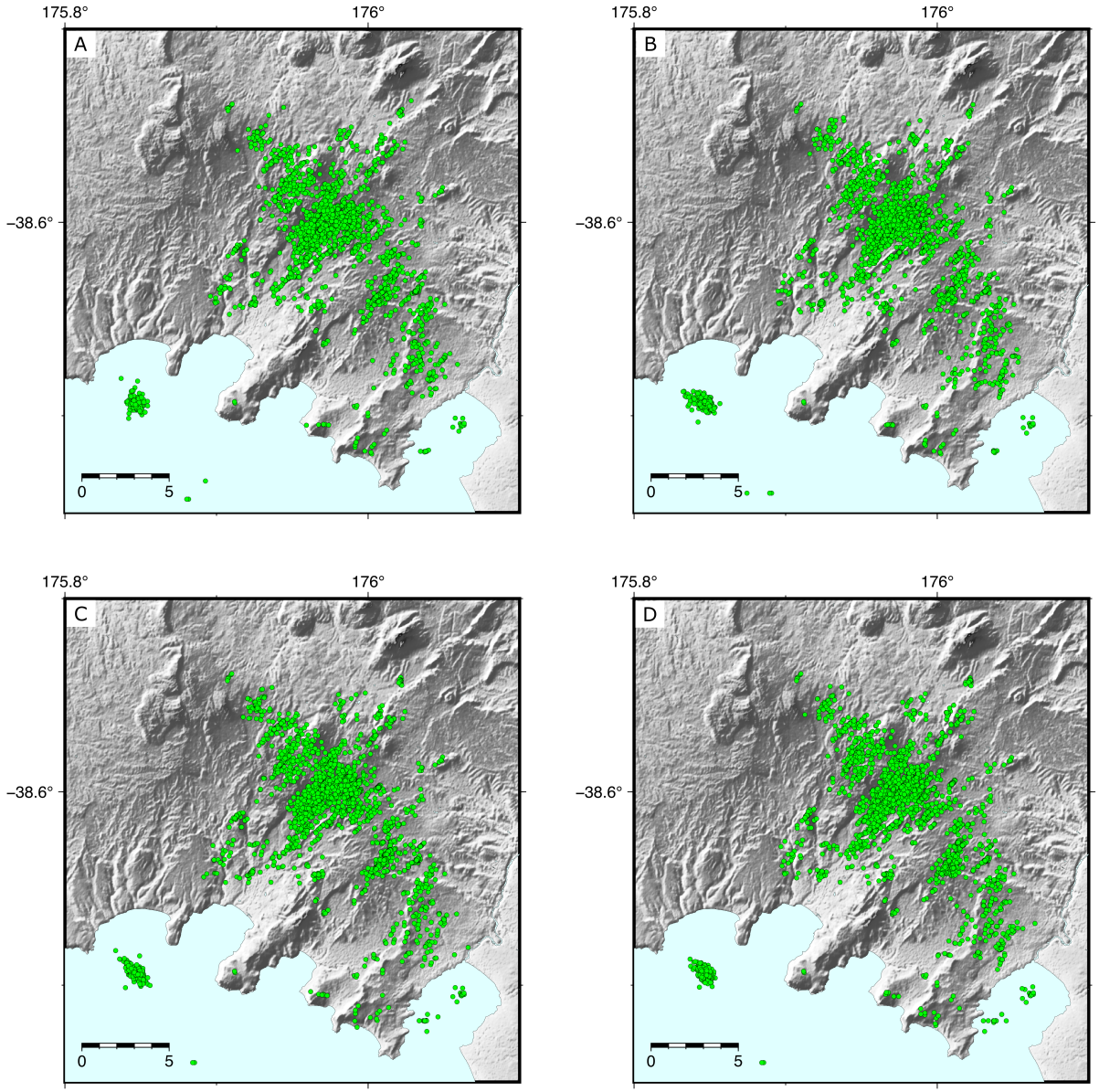

Figure 2.9: A map view of four different relocation runs from GrowClust. Each subplot has the corresponding rmin value: A = 0.36, B = 0.25, C = 0.5, D = 0.6. In each plot, earthquake magnitudes were not included and all events have a uniform size.

rmin values of 0.5 and 0.6 (See results) and they relocated a similar number of events (2729 and 2748), we have chosen the lower threshold. This is to reduce the chance of valid events not being relocated as the result of an overly strict correlation coefficient.

The second input parameter is 'delmax' which is the maximum station distance used for differential times in the event-pair similarity calculation (Trugman & Shearer, 2017). This value was set at 150 km, which remained constant in all GrowClust runs. The final input parameter is 'rmsmax', which is the maximum root-mean-square (rms) differential time residual for a suggested cluster merger to be allowed during relocation (Trugman & Shearer, 2017). This value was set to 1.20 and remained constant in all GrowClust runs. The 'rmsmax' could have been increased if ray path lengths were excessive or data quality was poor. However, given the close proximity of stations to the 2001 seismicity and having taken additional steps to ensure good data quality (e.g. building the 2.5D model), we chose not to increase the 'rmsmax' value.

Differential relocation resulted in 2729 of the 3873 detected earthquakes being relocated. This was an encouraging statistic, meaning over 70% of the detected events were relocated. During spatial and temporal distribution analysis, only relocated earthquakes were used (e.g. Figures 3.4 & 3.13). This improved the precision of our interpretation of subsurface structures. When analysing the rate of seismicity over the course of the swarm, the full earthquake catalog of relocated and non-relocated events was used to accurately estimate the size of the swarm (e.g. Figure 3.8).

Finally, the short run-time of GrowClust allowed the completion of an additional run at the chosen 'rmin' value of 0.5. This run implemented a bootstrap resampling component to estimate error. This resampled the data 10 times, outputting the same locations at the original 'rmin: 0.5' catalog while additionally calculating error estimates in the relative locations. The relative error estimates, along with the absolute error estimates calculated by NonLinLoc, will be outlined in the results chapter (Section 3.1).

2.2.5 Magnitude calculation

Following differential relocation, the final step in processing the relocated catalog is the calculation of local magnitudes (M_L) for each event (Figure 2.3). Magnitudes are an essential aspect of earthquake analysis and will help interpret the faults accommodating slip during this swarm.

Seismic energy will attenuate at varying rates within the crust based on the presence of partial melt, magmatic intrusions and lithologic variation (Schlotterbeck & Abers,

2001; Carletti & Gasperini, 2003; Keir et al., 2006; Wang et al., 2009). Given the high volumes of ignimbrite deposits in the Taupō region and the presence of the modern magma system beneath Lake Taupō, attenuation is relatively high in this region compared to the rest of the North Island (Henrys & Hochstein, 1990; Bannister, 1992; Dowrick, 2007; Rowland et al., 2010). This must be corrected with an attenuation curve, which will become part of the local magnitude estimation. This involves inverting maximum body-wave amplitude and hypocentral distance information to derive an M_L scale (Richter, 1935, 1958; Illsley-Kemp et al., 2017). This is shown below (Equation 2.5).

$$M_L = \log(A) - \log(A_0) + C \tag{2.5}$$

Here A is the maximum zero-to-peak amplitude on the seismogram, $\log(A_0)$ is a distance correction term and C is a correction term for each component of the seismic station from which the amplitude was taken. Both corrections are calculated empirically. However, Richter's scale tended to underestimate magnitudes at stations close to earthquake hypocentres and overestimate at more distant stations (Hutton & Boore, 1987). This led to the formation of an equation to calculate attenuation rates over varying hypocentral distances prior to calculating the local magnitude by Hutton & Boore (1987) (Equation 2.6). This equation is defined below.

$$-\log(A_0) = n\log(r/17) + K(r - 17) + 2 \tag{2.6}$$

Here, r is the hypocentral distance in kilometers and n and K are constants related to geometrical spreading and seismic attenuation. Equation 2.6 is calculated prior to Equation 2.5 to ensure more accurate local magnitude calculations.

The methodology employed here aims to simulate the response of the Wood-Anderson seismometer the M_L scale was defined for (Anderson & Wood, 1925; Illsley-Kemp et al., 2017). To do this, the instrument response must be calculated for each event, convolving velocity-based seismograms into displacement (Anderson & Wood, 1925; Kanamori & Jennings, 1978; Illsley-Kemp et al., 2017). We must then pick the maximum zero-to-peak amplitude of each event in our final catalog of relocated and non-relocated events. These amplitudes are limited to a three second window and filtered between 1 and 10 Hz. Distances for the hypocentre of each event is determined by a combination of event and station locations. The calculation of local magnitude is then completed, using the equations of Richter (1935); Hutton & Boore (1987).

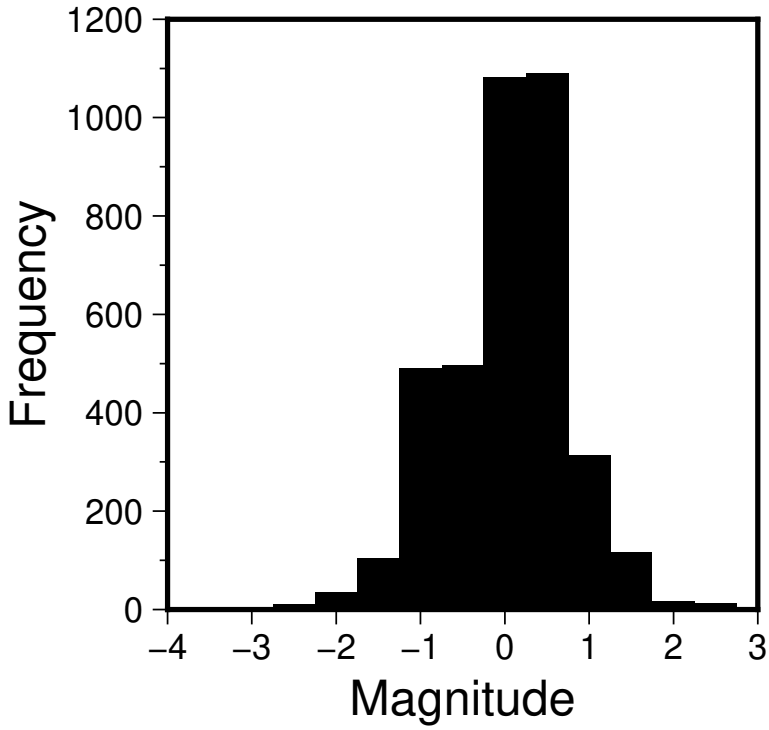

Figure 2.10: A histogram showing the magnitude distribution of earthquakes detected over the course of the 2001 swarm. The distribution consistent with expectations, indicating we are detecting all earthquakes > M_L 0–0.5.

It should be noted that for the 2001 seismicity, a full magnitude inversion was not completed. Instead we utilised the equation of Hutton & Boore (1987) and used the inversion parameters for Taupō previously calculated by Illsley-Kemp et al. (2021). The distribution of magnitudes calculated for the earthquakes detected in the 2001 swarm is shown in Figure 2.10. This distribution indicates that we have a magnitude of completeness between M_L 0–0.5, suggesting we are detecting all earthquakes at or above this magnitude threshold. Below this threshold, the frequency of detections decreases, consistent with this proposed magnitude of completeness.

2.2.6 Focal mechanism calculation

The final stage of data processing focused on calculating focal mechanisms for a small number of chosen events in the swarm. Focal mechanisms can be used to describe the kinematic behaviour of seismic sources using the event's moment tensor (Pugh et al., 2016). This will be done using MTfit, a source inversion package developed for Python (Pugh & White, 2018). MTfit utilises the polarity picks from the P-wave arrivals identified in Snuffler and amplitude ratios in a Bayesian framework to estimate

the source probability density function (PDF) for each event (Pugh & White, 2018).

When completing inversions in seismology, ordinarily Greens function's are calculated to perform full waveform inversions (Heimann, 2011; Duputel et al., 2012). This works well for regional seismicity but the calculations can be difficult on smaller networks as the velocity structure is rarely well constrained (Pugh et al., 2016). These velocity variations significantly effect ray-paths due to the close proximity of receivers to seismic sources (Reasenberg, 1985). Complex velocity structures and close proximity between sources and receivers are both restricting factors for our dataset, pushing us to utilise observational parameters such as P-wave polarities and amplitude ratios which are more robust in these conditions (Reasenberg, 1985; Hardebeck & Shearer, 2002, 2003; Snoke et al., 2003).

P-wave polarities and amplitude ratios are incorporated by MTfit in a Bayesian framework to estimate the full source PDF for full moment tensor model spaces (Pugh & White, 2018), allowing the production of double-couple solutions. Double-couple solutions were chosen as most earthquakes in the swarm are likely due to faulting and with the non-ideal station network distribution, it would not have been possible to constrain non-double-couple solutions. The inversion method aims to find the best fitting model parameters for the given data. In the case of source inversion the PDF describes the likelihood of observing the data for a given earthquake source considering the model (Pugh et al., 2016). However, this is dependent on the probability of the model based on the observed data (P-wave arrivals), which is termed the posterior PDF and can be evaluated using Bayes' Theorem (Bayes, 1763; Laplace, 1812; Sivia & Skilling, 2006).

$$\rho(model|data) = ((\rho(data|model)\rho(model)) \div (\rho(data))) \tag{2.7}$$

The two PDFs are related using previous probabilities, stemming from observational data, by Bayes' theorem (Equation 2.7). The likelihood of observations and uncertainties for a source at each receiver are combined over a range of random moment tensor samples to produce the likelihood for all receivers (Pugh & White, 2018). These samples correspond to the distribution of possible earthquake locations on a focal sphere and allow the inclusion of location and model uncertainties. These samples are combined, summing the locations and uncertainties to produce the marginalised location likelihood (Sivia & Skilling, 2006; Pugh et al., 2016; Pugh & White, 2018). We chose a limit of 100,000 samples to be combined and marginalised. If MTfit is still able to produce solutions past this limit, it rejects the focal mechanism as it cannot be adequately constrained.

MTfit differs from other Bayesian inversion approaches by its focus on far-field observations such as P-wave polarities and amplitude ratios (Pugh et al., 2016). Other methods utilise near-field observations and finite-fault models (Zollo & Bernard, 1991; Minson et al., 2013). However, these have proven to be less stable when the velocity structure of the research area is uncertain (Pugh et al., 2016).

The earthquakes inputted to MTfit were chosen based on their previously calculated local magnitude (see 2.2.5). This decision was made due to higher magnitude earthquakes typically producing clearer signals on seismometer recordings, making it easier to identify P-wave arrival polarities. Larger magnitude events are also more likely to produce clear signals on both the CNIPSE and START arrays, regardless of their location. This is advantageous events with an increased number of polarity picks are likely to produce more well constrained focal mechanisms. Based on experience attempting to pick polarities in Snuffler, we decided on a lower threshold of $M_L1.5$. This was justified, as we were able to successfully calculate moment tensors for a $M_L1.55$ event, but could not successfully calculate for a $M_L1.47$ event. Other factors, such as the location of the earthquake relative to the recording station, will affect the clarity of phase arrivals, but these are out of our control.

Polarities on P-wave arrivals must be identified without a filter applied to the waveform data in Snuffler. Filters, while helpful for isolating earthquakes from background noise, can introduce phase shifts that affect the apparent polarity of the P-wave arrival. Therefore selected events must either have sufficient magnitude, or be close enough to the seismometer to record a clear arrival in an unfiltered stream. The other values required for the MTfit algorithm, notably the take-off angle and azimuth for the ray in each source-receiver pairing, are calculated when the event is located via NonLinLoc. A focal mechanism is then calculated by MTfit, assuming the source can be constrained within our limit of 100,000 random samples.

Because the normalised full moment tensor source is 5-D, there are several different methods for accurately representing the source on paper (Hudson et al., 1989; Riedesel & Jordan, 1989; Chapman & Leaney, 2012; Tape & Tape, 2012). Each focal mechanism we outputted has three subplots: two fault plane plots and a map view of the focal mechanism location (Figure 2.11). The full fault-plane subplot (Figure 2.11, top-left) shows all possible fault plane orientations that could explain the arrival data, presenting the average as green lines. The three kinematic axes, 'Pressure', 'Null' and 'Tensile' are plotted as red, green and blue dots respectively. The second subplot shows the highest probability pairing of fault plane orientations that could explain the earthquake arrival data (Figure 2.11, top-right). In this subplot, the compressional quadrants have been

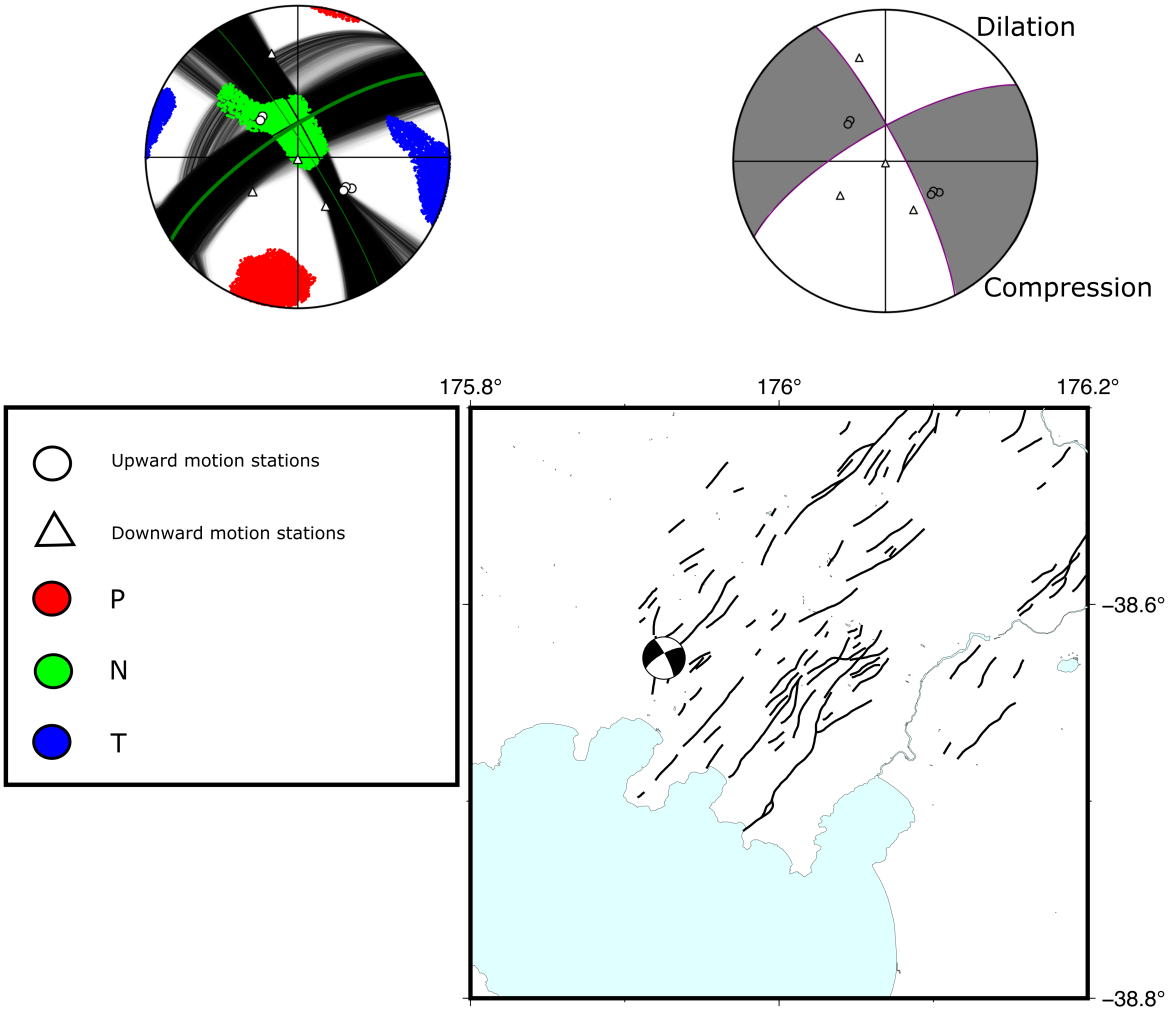

Figure 2.11: Example of focal mechanism result plots, consisting of two fault plane subplots from MTfit and a map of the mechanism. This example event is the first focal mechanism result. In both fault plane subplots, dilatational stations are white triangles and compressional stations are white circles (legend). The left plot shows all possible pairs of fault plane orientations that could explain the polarity data, with darker lines indicating higher probability. The average pairing are shown as green lines. The kinematic Pressure (P), Null (N) and Tensile (T) axes are plotted on this fault plane subplot. The right hand plot shows the highest probability pairing of fault plane orientations. The beach-ball focal mechanism plot is shown on the map, showing compression in black and dilation in white.

shaded, in addition to the inclusion of station motion data points. Regarding station data, stations recording upward motion are shown as circles, while stations recording downward motion are shown as triangles. The highest probability focal mechanism is also plotted in map view, against the active faults in the Taupō region (Figure 2.11, map).

Chapter 3

Results

This chapter begins with a brief description of the template earthquake locations, calculated by NonLinLoc (Section 3.2). Then outlines the results of the detection and relocation process including analysing the spatial and temporal distributions of relocated events (Sections 3.3 & 3.4). GrowClust managed to relocate 2729 out of the 3782 earthquakes detected by EQcorrscan, representing a 72% relocation success rate. Given these results will be used to interpret subsurface structures, we want to ensure only accurately relocated earthquakes are used in these sections of the results.

Finally, we present the results of MTfit's focal mechanism calculations (Section 3.5). This will involve the location of each event used, as relocated in GrowClust and two fault plane plots showing the full range of possible solutions and the highest probability solution. This section will present the results of the six successful focal mechanisms.

3.1 Location uncertainties

Before discussing the results of the location and relocation processes, the error associated with these locations must be addressed. For the locations determined by NonLinLoc, the average horizontal and depth error estimates were 5.2 and 4.5 km, respectively. This error is calculated for all 3782 earthquakes detected via EQcorrscan and is based on the 68% confidence level of the PDF ellipsoid. The horizontal NonLinLoc error is normally distributed (Figure 3.1), with an average closer to 3–4 km when down-weighting outliers. The NonLinLoc depth error distribution is bi-modal, with most locations having 3–4 km of associated depth error. A second peak indicates a large number of earthquakes have absolute depth error between 5–6 km.

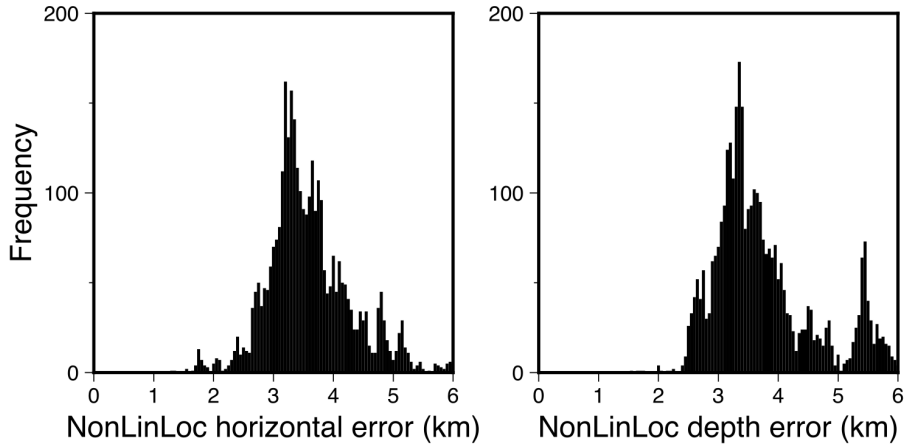

Figure 3.1: Two histograms showing the distributions of the absolute horizontal and depth error associated with the locations calculated by NonLinLoc

There is additional error associated with the 2729 relocations completed via GrowClust, termed the relative error. The relative error was calculated via bootstrap analysis and is the median absolute deviation of the bootstrap event location distribution. The average horizontal and vertical relative error estimates are 0.25 and 0.18 km, respectively. The relative error is negatively skewed compared to the normal distribution of the absolute NonLinLoc errors. Both the relative horizontal and depth errors display this distribution, indicating a high weighting of low relative error values.

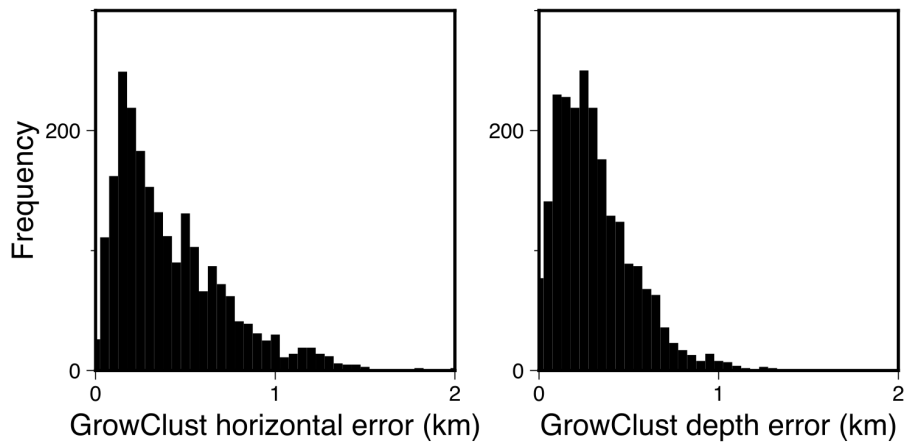

Figure 3.2: Two histograms showing the distributions of the relative horizontal and depth error associated with the relative locations calculated by NonLinLoc

Considering this, it is clear that the NonLinLoc located earthquakes include significantly higher error estimates than the relocated earthquakes. This is consistent with expectations. This means while the absolute locations or depths of the swarm earth-

quakes may vary, the position of earthquakes relative to each other shows little variance. Therefore, we are confident in the clusters and subsurface structures outlined by the results of the relocation process.

3.2 NonLinLoc results

Following the identification of template earthquakes in snuffler, these events were located in NonLinLoc as a data quality check. NonLinLoc does not output the necessary resolution for us to make confident interpretations, but provides conformation that the template events have been picked and located reasonably. Furthermore, these locations can aid initial interpretations, as we would expect earthquakes detected using these templates to be located in similar areas.

The distribution of the template earthquakes shows most events occurred within the bounds of the Taupō Fault Belt (Figure 3.3). There are some outliers which occur beneath Lake Taupō and five events which occurred further southeast. These outlier events show little clustering and are limited to individual, well spaced events. By contrast, the template events located within the Taupō Fault Belt show distinct grouping. The most prominent of these is the northeast trending, elongated cluster of earthquakes in the centre of the fault belt. This cluster sits between the Whangamata and Ngangiho faults and is approximately 2 km north of the Kinloch township (See Figure 1.1 for major fault locations). This cluster appears to be located closer to the Whangamata Fault, but the resolution of these results is not high enough to confirm this. Template earthquakes occurring within the Taupō Fault Belt are generally closely spaced.

3.3 Spatial distribution of relocated events

This section outlines the spatial distribution of the relocated earthquakes. These results are based on the earthquakes in GrowClust, using an rmin value of 0.5 (C in Figure 2.9). Detections that could not be relocated have been omitted from the spatial results section, given the increased error associated with NonLinLoc locations.

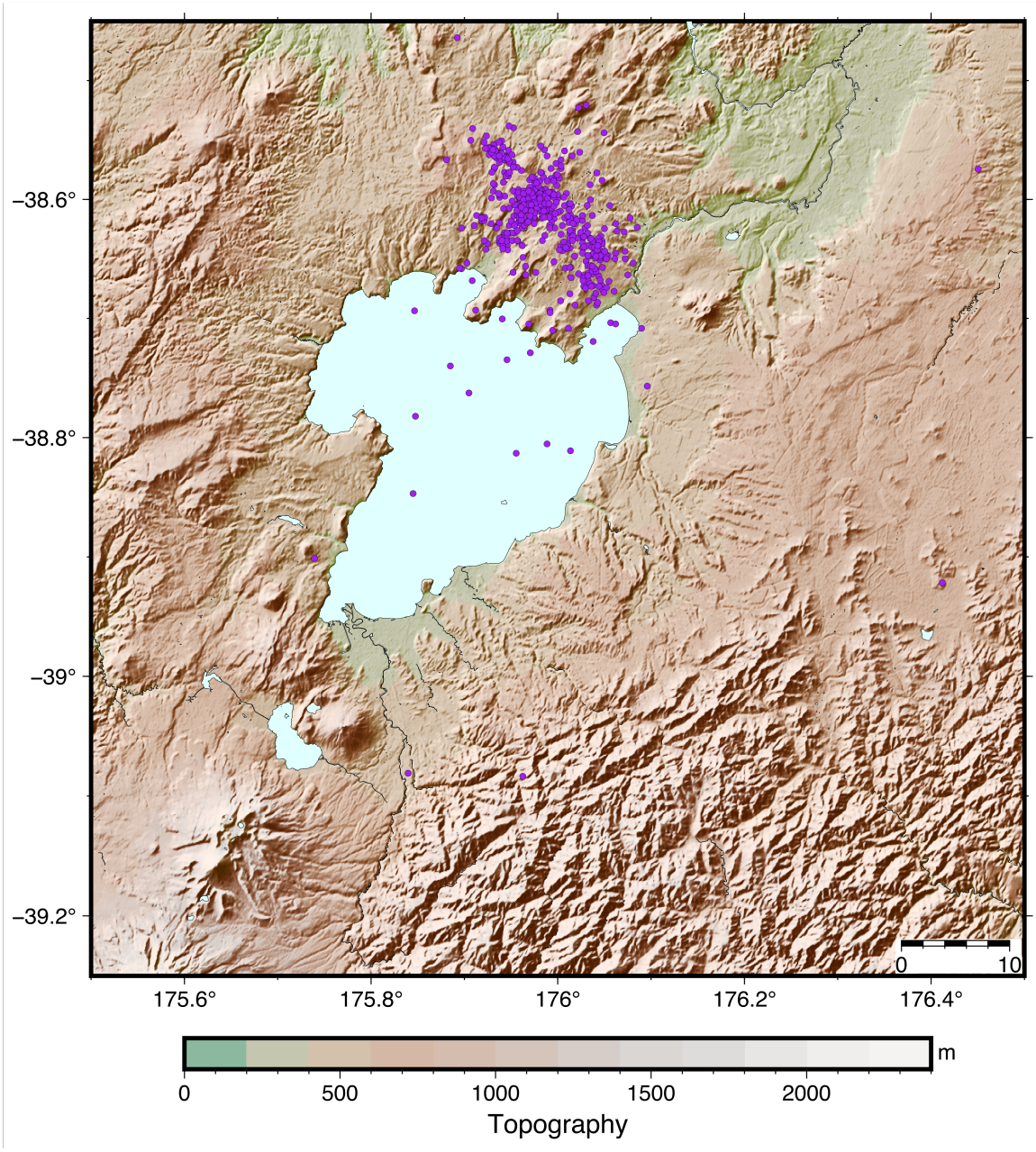

Figure 3.3: A map of the template events identified in snuffler and located in NonLinLoc. Earthquakes are shown as purple circles, magnitudes were not calculated for template events so sizes are uniform. Distance scaled in km.

3.3.1 Mapped results

The distribution of the relocated events shares similarities with the template events located by NonLinLoc, both producing a large cluster closely aligned to the Whangamata Fault (Figure 3.4). Several other clusters of events are also seen in close proximity to the Whakaipo and Kaiapo faults to the southeast. The clusters, along with others within the Taupō Fault Belt, are mostly linear in their distribution and trend parallel to the fault belt. In some instances, specifically on the southeastern side of the Kaiapo fault close to Taupō township, there are linear groupings of earthquakes which are not aligned with any known faults.

Another major cluster of earthquakes occurred beneath Lake Taupō's Western Bay. This cluster of events is elongate in map view, trending northwest and perpendicular to the fault belt. Isolated events also occur near beneath the northeastern lake-shore in close proximity to Taupō township (Figure 3.4).

The majority of swarm earthquakes are low magnitude, especially the ones making up the large clusters close to the Whangamata, Whakaipo and Kaiapo faults (Figure 3.4). Here we see high numbers of low magnitude earthquakes (<1 M_L), punctuated by more irregular, larger magnitude (1–2.5 M_L) events. The ratio of low to high magnitude events decreases significantly in the northwestern extent of the Taupō Fault Belt, with a larger proportion of high magnitude events (M_L 1.5–2.5) occurring in this region. The magnitudes of events occurring beneath the northeastern bay are larger and show less variation than most in the fault belt. The major cluster beneath the Western Bay consists primarily of <1 M_L earthquakes.

3.3.2 Cross-section results

There are four separate vertical cross-sections taken through the relocated swarm data (lines: A, B, C and D in Figure 3.4). Cross-section A covers the vertical distribution of events in the northwestern region of the Taupō Fault Belt, encompassing the Whangamata and Ngangiho faults (Figure 3.5).

The distribution of events in cross-section A is skewed towards the centre of the fault belt, with most events occurring between 5–9.5 km along the cross-section. This includes the large cluster of events in close proximity to the Whangamata Fault, at ∼6–6.5 km along the cross-section. This large cluster consists of multiple smaller groups trending at near vertical angles. This pattern is also seen further northwest, with another

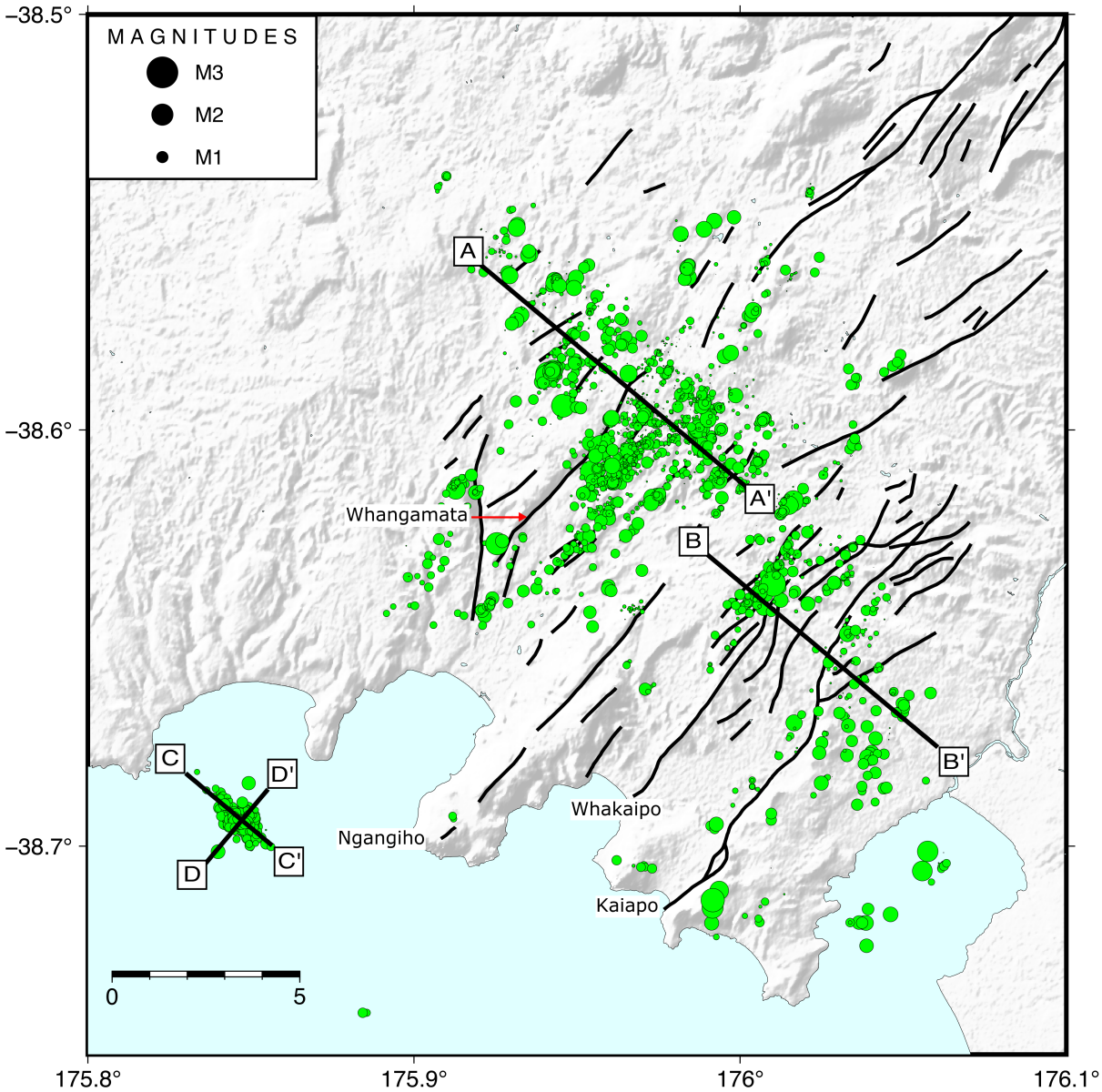

Figure 3.4: A map of double-difference relocated earthquakes, including detections and templates, via GrowClust using an 'rmin' value of 0.5. Earthquakes are shown as green circles and active faults are black, with major faults labelled. Four cross-section lines have been plotted, and correspond to Figures 3.5, 3.6 & 3.7.

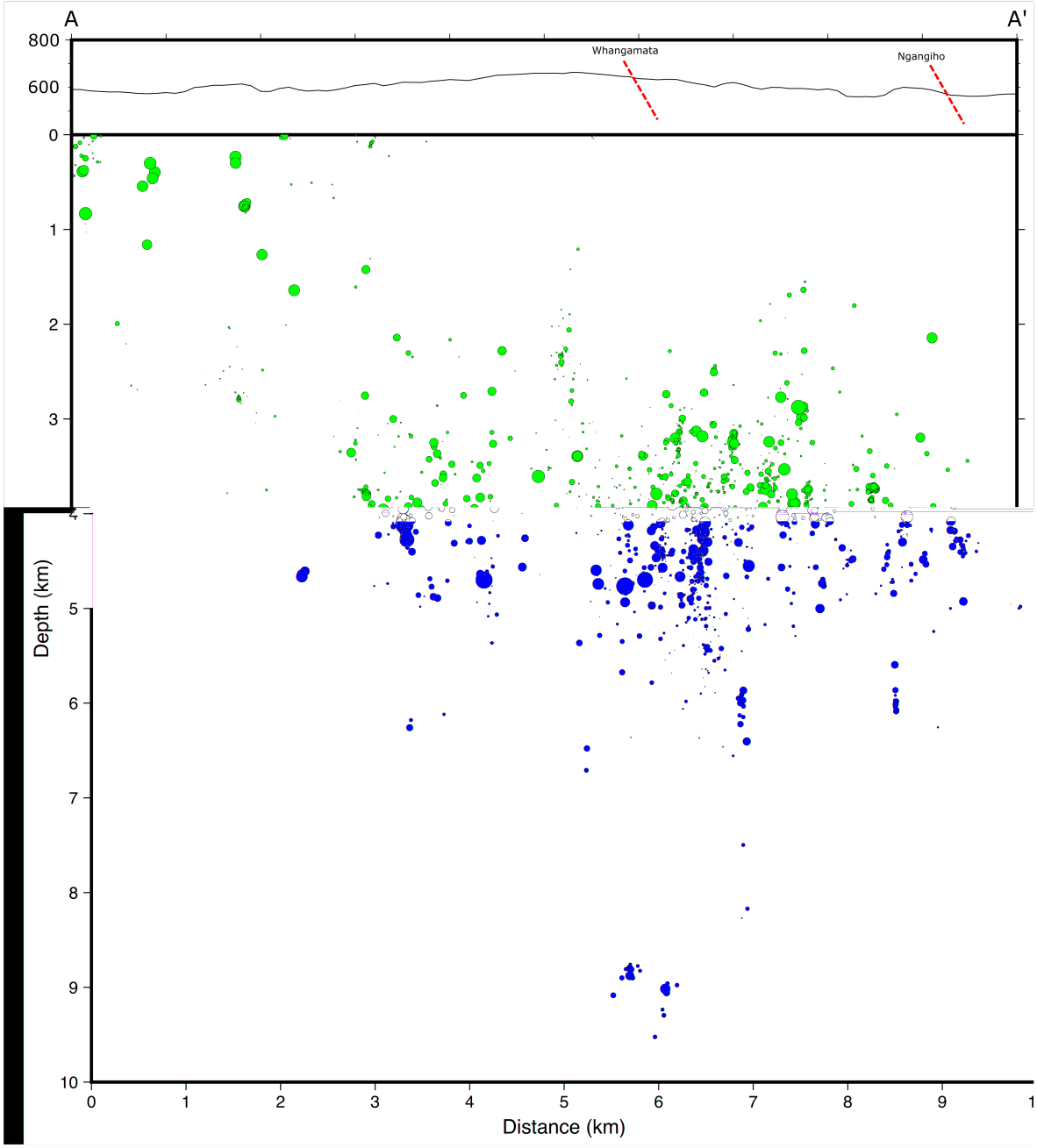

Figure 3.5: Cross-section of earthquakes relocated by GrowClust. This cross-section corresponds to the line marked A–A' in Figure 3.4 and uses the same magnitude scale. Depth and distance are in km, while elevation is scaled in metres.

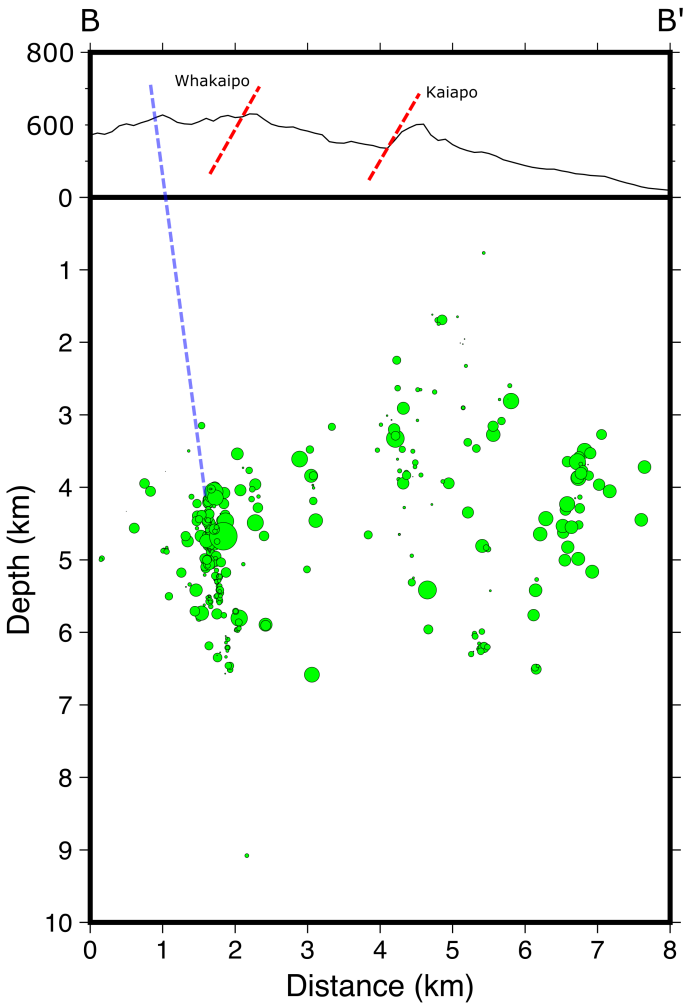

Figure 3.6: Vertical cross-section corresponding to the line B–B' in Figure 3.4, spanning the southeastern portion of the Taupō Fault Belt. Trend of prominent cluster is projected upward with a blue line. The Whakaipo and Kaiapo faults are shown as red dashed lines and the same magnitude scale is used as in Figure 3.4. Elevation above 0 is measured in metres.

steeply dipping cluster of events visible at ∼3 km.

The depth distribution of events along cross-section A is relatively uniform, with most events occurring between 2.5–5.5 km depth (Figure 3.5). There are two notable variations on this trend. Firstly, earthquakes occurred within 2 km of the surface from 0–4 km along cross-section A, including some events within the upper ∼200m, before quickly deepening. These events consist primarily of $M_L \geq 1$ events and show little magnitude variation. Secondly, at ∼6 km along the cross-section, a small cluster of earthquakes occurs at 9 km depth, the deepest in this region of the fault belt.

The depth distribution of events in the southeastern portion of the Taupō Fault Belt is more consistent than in the northwest, with the majority of events occurring within

a 3–6.5 km depth range (Figure 3.6). There are outliers occurring at 9km depth and within 2km of the surface, but these are individual events rather than clusters seen further northwest. There are also less events occurring in this southern half of the fault belt compared to in the northwest.

The most prominent cluster of events occurs ∼2 km along cross-section B, corresponding to the cluster closely aligned to the Whakaipo Fault (Figure 3.4). This significant grouping of earthquakes forms a steeply dipping cluster between 4–7 km depth. This cluster dips approximately 80 degrees and displays a range of magnitudes. The majority of events are relatively low magnitude, however one of the largest magnitude events ($M_L > 2$) in the entire swarm occurred around 5 km depth within this cluster. Another, less prominent cluster of events occurred approximately 7 km along cross-section B (Figure 3.6), consisting of higher magnitude earthquakes.

There are other isolated groupings of earthquakes separating these two clusters below the topographic rise inferred as representing the Kaiapo Fault topography. These groupings also contain multiple $M_L > 1$, but are not as dense as the cluster beneath the Whakaipo Fault. Small groupings of low magnitude earthquakes also occur sporadically throughout cross-section B.

The final two cross-sections, C and D, bisect the large cluster of events occurring beneath Lake Taupō's Western Bay (Figure 3.4). Cross-section C runs perpendicular to the Taupō Fault Belt, while cross-section D is parallel (Figure 3.7).

The spatial distributions of the earthquakes in cross-sections C and D indicate the cluster is dipping approximately 80 degrees to the northwest. The events in the cluster are more constrained than those in the Taupō Fault Belt, forming a tight ellipsoid with few outliers. The cluster is thickest between ∼3 and 5 km depth, before pinching out towards its shallower and deeper regions. Two notable outliers can be seen in cross-section D at ∼1 and 3 km along the cross-section line. Both are $M_L 1$ events occurring between 3 and 4 km depth and occur approximately 1 km removed from the cluster. Additional outliers can also be seen above and below the main cluster, occurring around 1 and 7 km depth respectively. These events are lower magnitude than the horizontal outliers occurring to the north and south (Figure 3.7).

The magnitudes in these cross-sections are reduced compared to seismicity in the fault belt, recording no events $> M_L$ 1.5 and a large number of $< M_L$ 1 events. In keeping with the ellipsoidal spatial distribution, the majority of higher magnitude events occur in the centre of the cluster. Generally, there is less variation in magnitude in the lake cluster than in clusters within the Taupō Fault Belt (Figures 3.5 & 3.6). There are

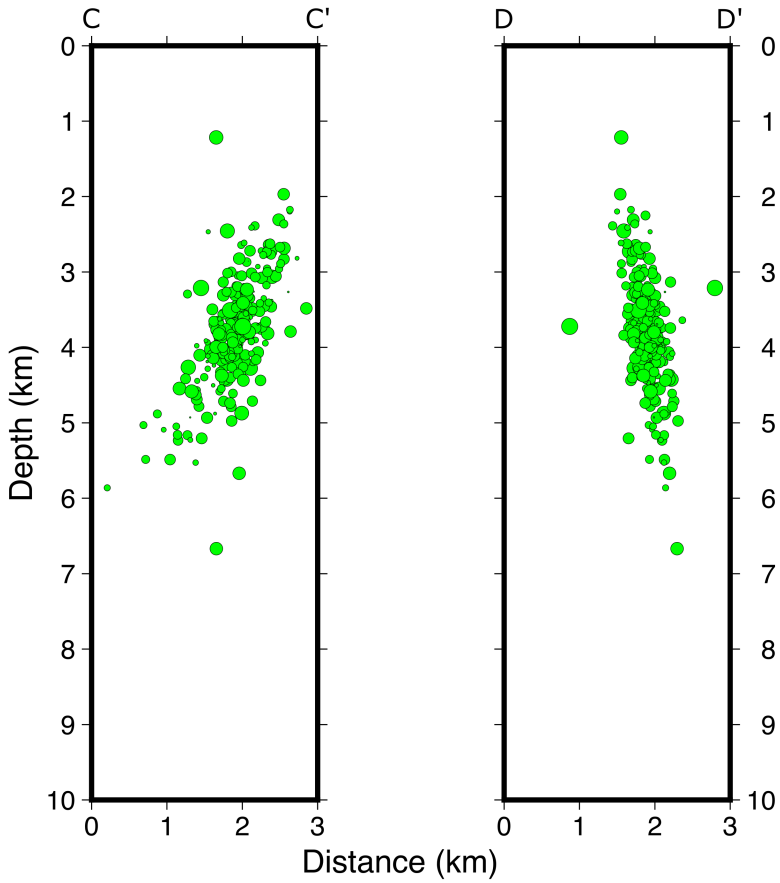

Figure 3.7: The left plot is a vertical cross-section corresponding to line 'C' in Figure 3.4. The right plot is a vertical cross-section corresponding to line 'D' in the same plot. Magnitude scales are as in Figure 3.4.

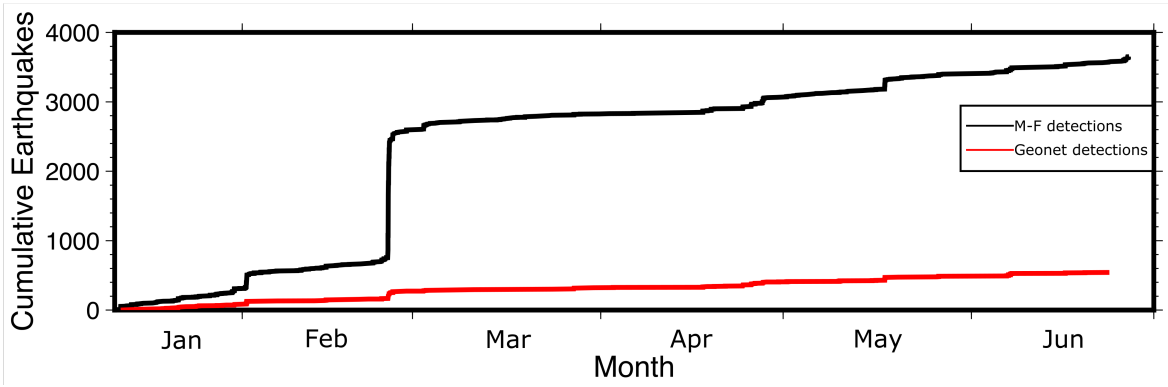

Figure 3.8: Plot of the cumulative total earthquakes against the months of the year. Our matched-filter (M-F) detections are shown in black. A second line (red) has been included to show the cumulative total of events detected by GeoNet.

also considerably fewer small magnitude earthquakes in this cluster compared to fault belt earthquake clusters.

3.4 Temporal distribution of relocated earthquakes

3.4.1 Broad focus

Along with the spatial distribution of earthquakes that occurred during this swarm, we are interested in their temporal distribution. Broadly, the rate of earthquake occurrence follows a step-wise trend, with a shallow linear trend punctuated by short periods of significant earthquake occurrence (Figure 3.8). The largest of these spikes in earthquake activity occurred on the 24th and 25th of February, where the number of cumulative earthquakes increases by approximately 2000. This cluster of earthquakes makes up a significant portion of the total earthquakes count for the swarm, but smaller periods of unrest can also be identified. An increase in the cumulative number of earthquakes of approximately 300 occurred on the 2nd of February (Figure 3.8). A similar period of unrest can also be identified on the 17th of May, increasing the cumulative earthquake total by $\sim$200 events.

In the four months without significant (>200 events) unrest periods, multiple episodes of minor unrest occur (Figure 3.8). This is evident in the later half of April, where unrest can be identified on five separate occasions, but are limited to less than 100

earthquakes each. March displays a similarly asymmetrical distribution of earthquakes, with a few periods of minor unrest occurring at the start of the month. In both March and April, between periods of minor unrest there is a shallow linear increase in cumulative earthquake total of ∼200 earthquakes per month. This suggests regular seismicity in these months, but at a frequency too small for our cumulative plot to resolve.

The asymmetrical distribution is not seen in January and June, which have small periods of unrest evenly distributed throughout. These minor spikes in cumulative earthquake total help contribute to the linear trend most clearly seen in January and June.

The step-wise pattern is mirrored in the detections made by GeoNet over this time (Figure 3.8, red line). Small spikes occurred at the same intervals, indicating we are detecting significantly more earthquakes during periods of increased seismicity than GeoNet, but are generally detecting events on the same days.

The distribution of earthquakes parallel to the Taupō Rift is relatively constrained, with the majority of swarm earthquakes occurring in a 10 km band either side of our cross-section line (Figure 3.9, top). The primary exception to this trend occurs during some periods of increased seismicity, seen during February, April and May. Early swarm earthquakes at the beginning of January are tightly constrained to the 10km central band, with the only exception being a small number of earthquakes occurring approximately 12 km to the southwest (down-rift). These events mark the beginning of the swarm beneath Lake Taupō's Western Bay (Figure 3.4), with more earthquakes occurring here during February, March and April. The rift-parallel spread of earthquakes increases in February, with high seismicity on the 1st producing events further southwest. Another, much larger, period of seismicity occurred on the 24th and 25th of February, showing earthquakes occurring further southwest and northeast.

Few earthquakes occur within the Taupō Fault Belt in March, instead accumulating further southwest in the Western Bay cluster (Figure 3.9). During the later half of the swarm (April to June), the rift-parallel spread of earthquakes increases, with a greater proportion of events occurring to the southwest of the central fault belt. This most clear during periods of high seismicity on the 27th of April and the 17th of May.

The spatial distribution of earthquakes perpendicular to the Taupō Rift begins with a moderate 10 km spread along the cross-section line (Figure 3.9, middle). This indicates most January events occurred in the central fault belt but were loosely constrained. This level of diversity disappears moving into February, with the majority of events

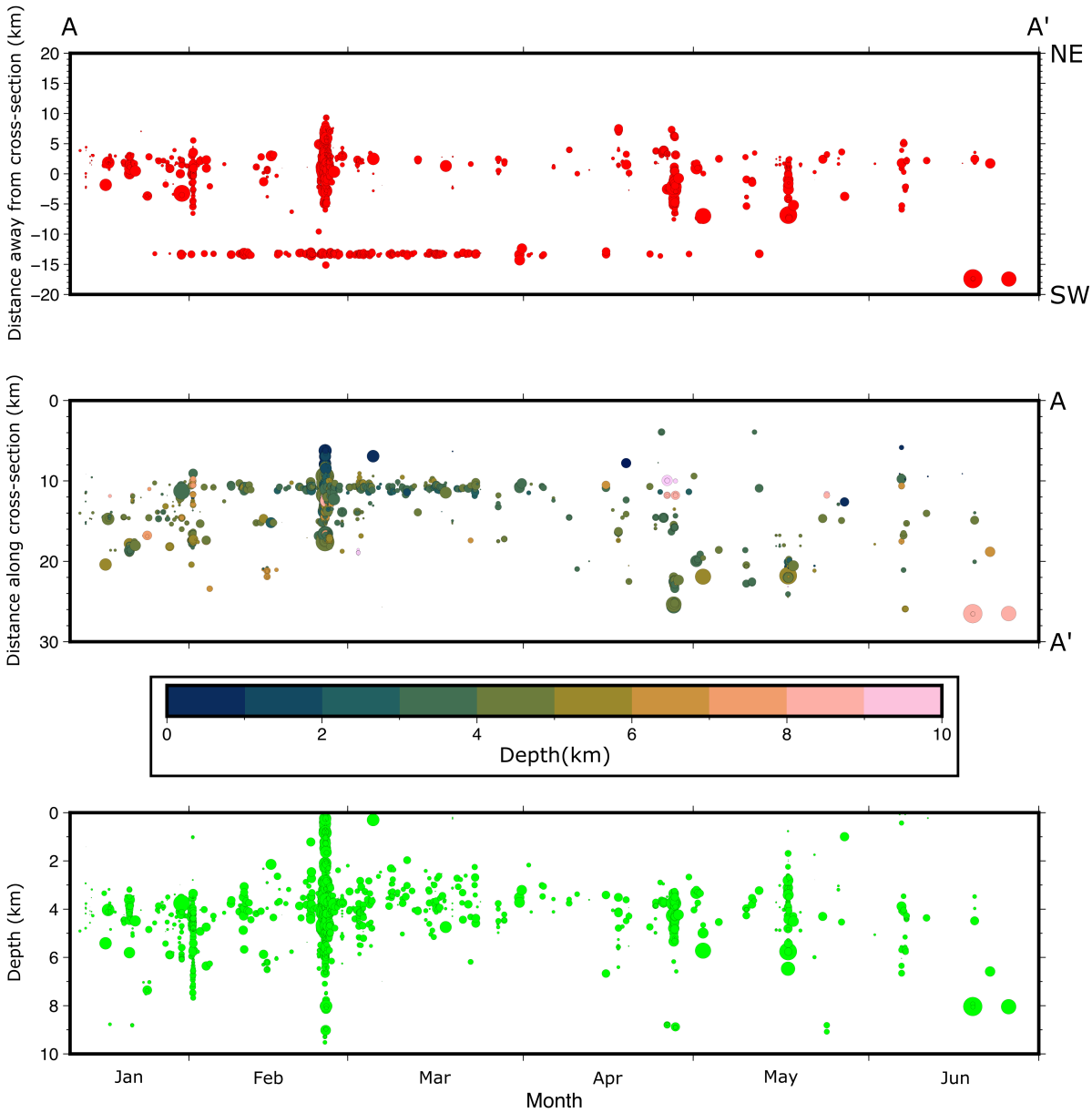

Figure 3.9: Three plots relating the location and depths of earthquakes relative to their origin time, ranging from 11/01/2001–30/06/2001. All plots show time (in months) on the x-axis. The top plot shows the distribution of earthquakes perpendicular to the cross-section A in Figure 3.13. The middle plot displays the distribution of earthquakes along the same cross-section, with increasing values moving from northwest to southeast across the fault belt. The middle plot uses a depth colour scale. The bottom plot shows the depth of swarm earthquakes compared to origin time.

constrained to ∼10 km along the cross-section. This places most February events as occurring in the northwest region of the fault belt. Two exceptions to this occur on the 1st and 25th, where a number of earthquakes are distributed further southeast and northwest. Earthquakes occurring in March return to a tight spread, corresponding to the cluster beneath the Western Bay. The distribution perpendicular to the rift becomes highly variable during the latter half of the swarm, with the spread increasing to between 10 and 27 km along the cross-section. This indicates events in April, May and June were more heavily distributed across the central and southeast regions of the fault belt.

The depth distribution of events over the course of the swarm shows less variation than location (Figure 3.9, bottom). The depths of earthquakes during the swarm show good consistency on a broad scale, with most events occurring between 3–6 km. The main exceptions to this trend is during stretches of 1–2 days on which high volumes of seismicity occurred in February, April and May. During this periods, variation increases, ranging between 1 and 9 km depth on the 25th of February.

3.4.2 Periods of high seismicity

Examining the cumulative earthquake count and earthquake location relative to time (Figures 3.8 & 3.9), we have identified three periods of increased seismicity. These are the 1st and 24–25th of February and the 17th of May.

On the 1st of February, earthquakes occur between 15:30 and 18:30, separated by a 30 minute period of quiescence (Figure 3.10). Earthquakes share a relatively uniform depth between 4 and 6 km. Through both periods of earthquakes there are two major clusters of events, occurring in tightly constricted groups at 12 and 17 km along our rift-perpendicular cross-section (Figure 3.10, middle). There is more variation in the rift-parallel distribution, with earthquakes occurring in a 10 km range through the central fault belt (Figure 3.10, top).

The 24th and 25th of February host approximately 2000 earthquakes (Figure 3.8). When looking at this period of high seismicity, which lasts approximately 11 hours, we see most of the rift-parallel distribution is constrained to a ∼4 km band near the centre of the fault belt (Figure 3.11, top). Between 23:00 and 3:00, there are a number of earthquakes which occur 1–5 km southwest (down-rift) of this primary cluster of events. This trend is later reversed, as between 4:00 and 5:30 earthquakes instead occurred further northeast (up-rift) of the large central cluster.

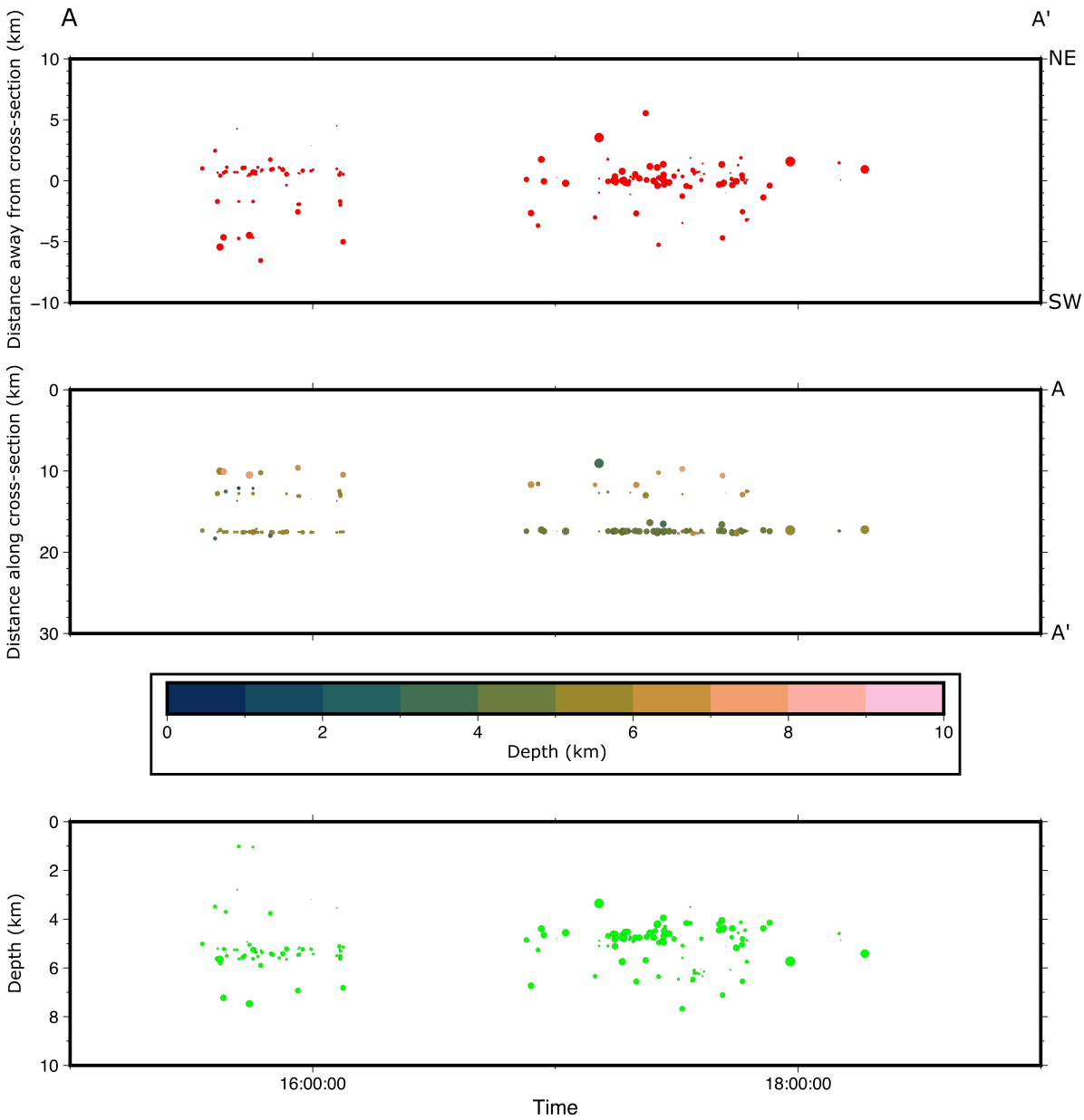

Figure 3.10: Three plots relating the location and depths of earthquakes to their origin time for events occurring between 15:00 and 19:00 on the 1st of February. Plots are as is in Figure 3.9, relating to cross-section A in Figure 3.13.

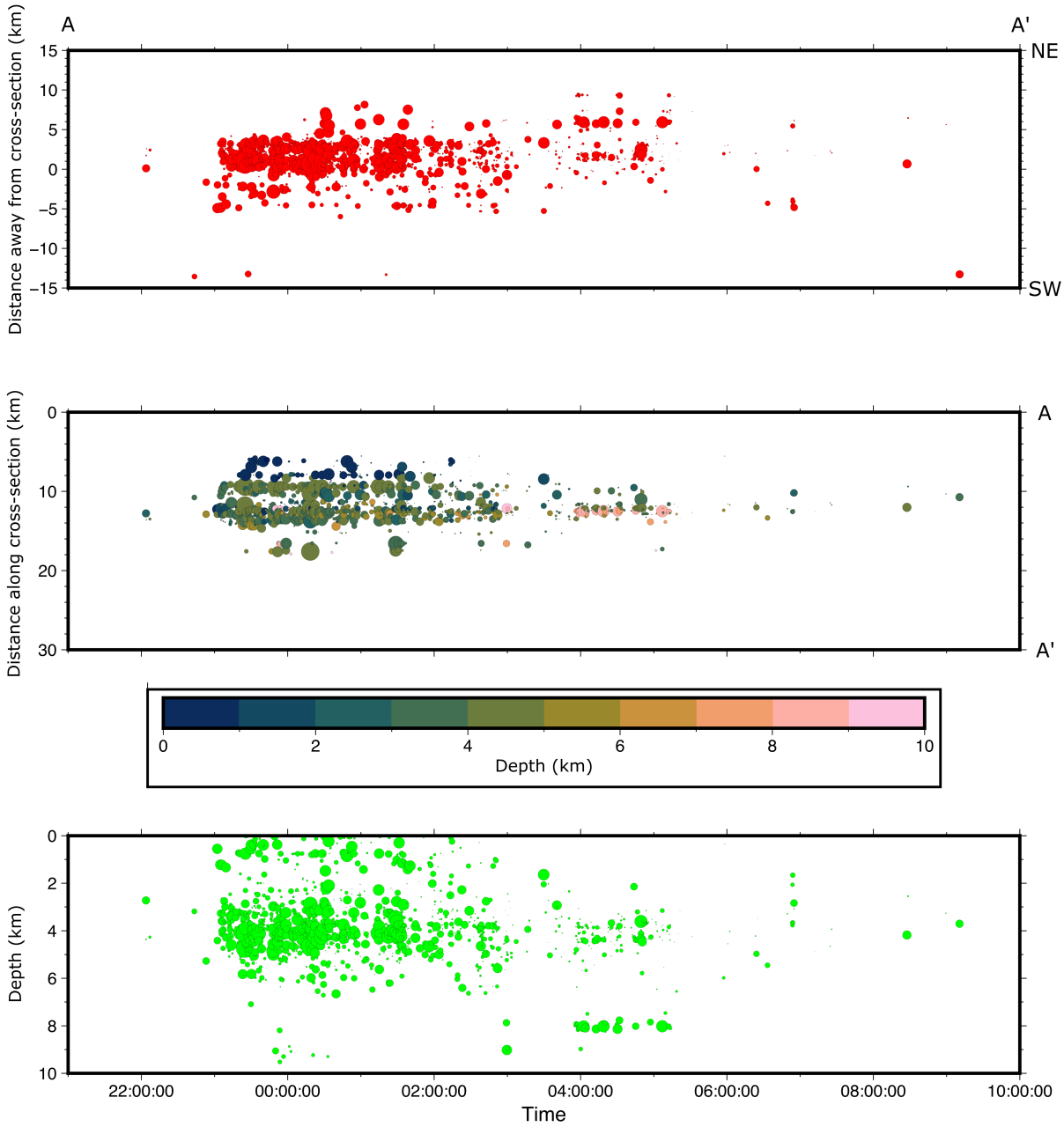

Figure 3.11: Three plots relating the location and depths of earthquakes to their origin time for events occurring between 21:00 on the 24th of February and 10:00 on the 25th of February. Plots are as is in Figure 3.9, relating to cross-section A in Figure 3.13.

When analysing the variation in location perpendicular to the Taupō Rift, we see the majority of earthquakes occur ∼13 km along the cross-section (Figure 3.11, middle). This corresponds to the cluster occurring near the Whangamata Fault (Figure 3.4), which accumulates earthquakes for approximately four hours, followed by a 30 minute period of quiescence before a further 90 minutes of activity. There are also three distinct lineations occurring at 6, 7 and 9 km along the cross-section. These lineations have durations of ∼3 hours and begin sequentially. The main cluster begins at approximately 23:00, followed by the 9km lineation at ∼23:10, the 7 km lineation at ∼23:20 and the 6 km lineation at ∼23:30. These lineations also become shallower as they move to the northwest, as seen by the deeper colour of the 6km lineation events. Following the period of quiescence at 3:30, activity is constrained to the largest cluster.

The depth range of events during this period of seismicity indicates most events occurred between 2.5 and 6 km depth (Figure 3.11, bottom). However, a secondary grouping of events was significantly shallower, within 1km of the surface and likely corresponding to the northwestern clusters. There are also a small number of events occurring deeper than the main cluster, at approximately 8–9 km depth.

Approximately 200 earthquakes occurred on the 17th of May, occurring primarily between 17:00 and 20:00 with a an hour of rapid activity around 17:45 (Figure 3.12). The along-rift distribution of these events indicates activity begins towards the centre of the fault belt, before progressively moving down-rift approaching 18:00 (Figure 3.12, top). After 18:00 the distribution of earthquakes moves further northeast towards the centre of the fault belt. The distribution of earthquakes across-rift is incredibly well constrained, with events forming a 2 km band occurring 21 km along the cross-section (Figure 3.12, middle). The depth distribution is slightly less uniform, with most events occurring between 2–6 km depth. There is also a notable outlier occurring at approximately 1 km depth.

3.4.3 Mapping temporal variation

Another method of high resolution analysis is mirroring the relocation map (Figure 3.4) and incorporating temporal data (Figure 3.13). This provides another view on the relationship between time and location for earthquakes in the 2001 swarm, allowing contextualisation with respect to the Taupō Fault Belt and its active faults.

Given two periods of increased seismicity occurred in the first two months of a six month swarm, the colour scale applied has been asymmetrically divided. As a result,

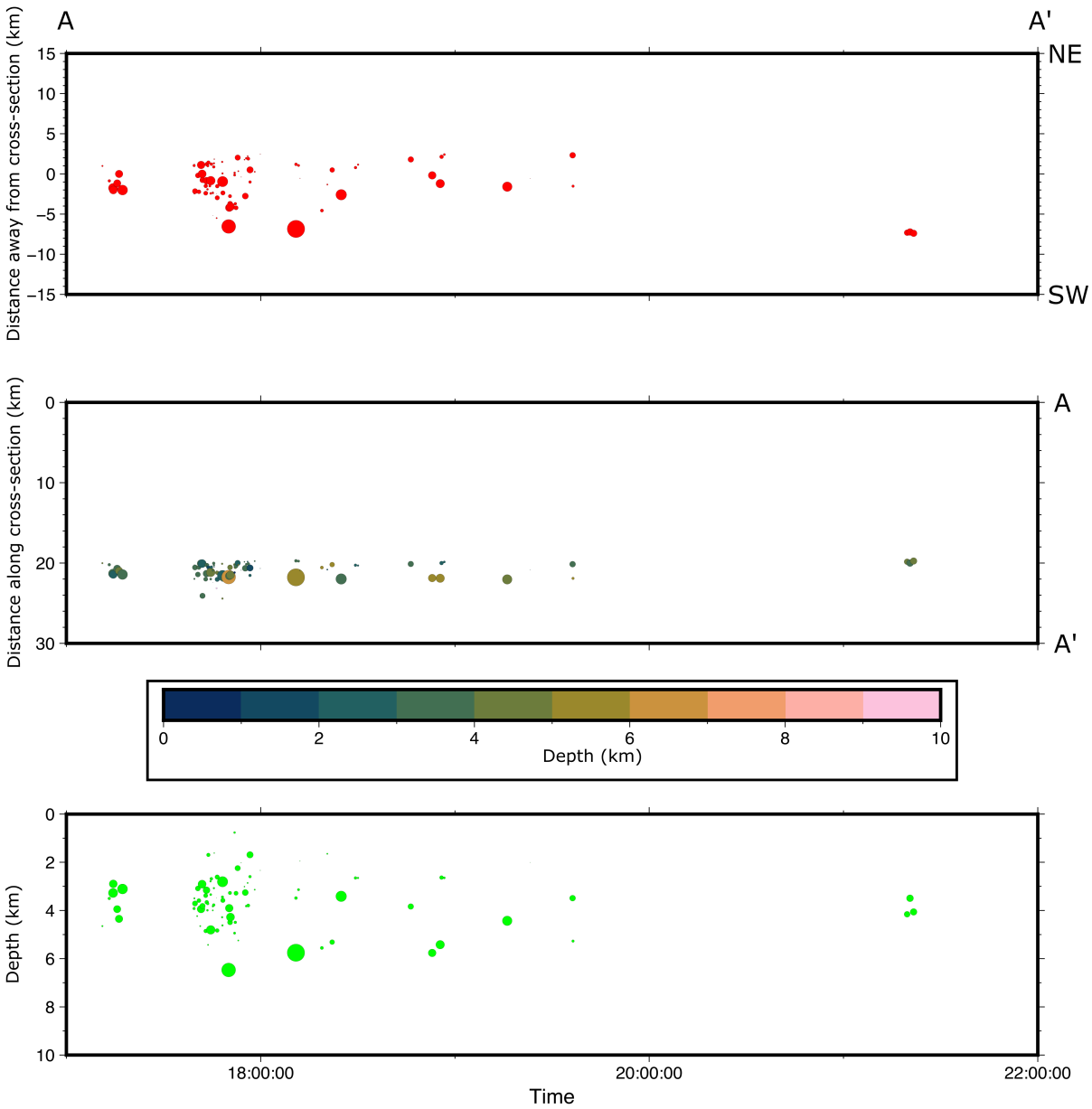

Figure 3.12: Three plots relating the location and depths of earthquakes to their origin time for events occurring between 17:00 and 22:00 on the 17th of May. Plots are as is in Figure 3.9.

January and February have been divided into four colour increments. March has been divided into two colour increments, given seismicity occurs beneath the Western Bay throughout this month (Figure 3.9). As the majority of seismicity during each of April, May and June occurs on a single day, a single colour for each month has been applied. This will capture the overall temporal diversity of the 2001 seismicity while allowing for increased resolution in months with more than one period of high seismicity.

There were approximately 300 earthquakes that occurred in January, the majority of which occur within the Taupō Fault Belt (Figure 3.13, dark blue). Within the fault belt, events in January are limited to the central and southeastern regions. Two groupings of earthquakes stand out close to the Ngangiho and Kaiapo faults, both occurring between 4 and 6 km depth. The grouping near the Kaiapo fault is larger, dips steeply and displays high magnitude variation (Figure 3.14). The earthquakes during January are $\sim M_L$ 1, although some larger magnitude events can be seen near the Ngangiho and Kaiapo faults. Generally, smaller clusters and individual events share a relatively uniform magnitude distribution.

Earthquakes occurring in February dominate the central and northwestern Taupō Fault Belt, showing strong clustering close to multiple active fault lines (Figure 3.13, green-brown). The largest of these groups forms close to the Whangamata Fault, with smaller clusters running along several unidentified active faults. There are more clusters further northwest, which align with smaller, unidentified active faults. In the northwestern Taupō Fault Belt February events stretch up-rift, with multiple $M_L > 1.5$ events occurring above the -38.6° latitude marker (Figure 3.13, map). The February events in the central fault belt are focused between 3–5 km depth, but become shallower towards the northwest and rise to within 1 km of the surface (Figure 3.14). There is a significant amount of magnitude variation in these events, with February clusters in the northwest and central Taupō Fault Belt containing a small number of $M_L > 1.5$ events surrounded by a tightly constrained grouping of smaller magnitude events. Earthquake magnitudes in February become more uniform moving further northwest.

A small minority of February earthquakes occurred further southeast, interspersed with January events around the Whakaipo Fault (Figure 3.14, teal). These events occurred during the period of high seismicity on the 1st of February and are concentrated in a steep cluster. Some individual events are scattered throughout the fault belt, including one M_L 2 event near the Whangamata Fault. Finally, February events can be seen occurring in the large cluster beneath Lake Taupō's Western Bay (Figure 3.15). Earthquakes occurring during February make up approximately 30% of this cluster and are largely contained within the central 2 km of its ellipsoidal shape. There is

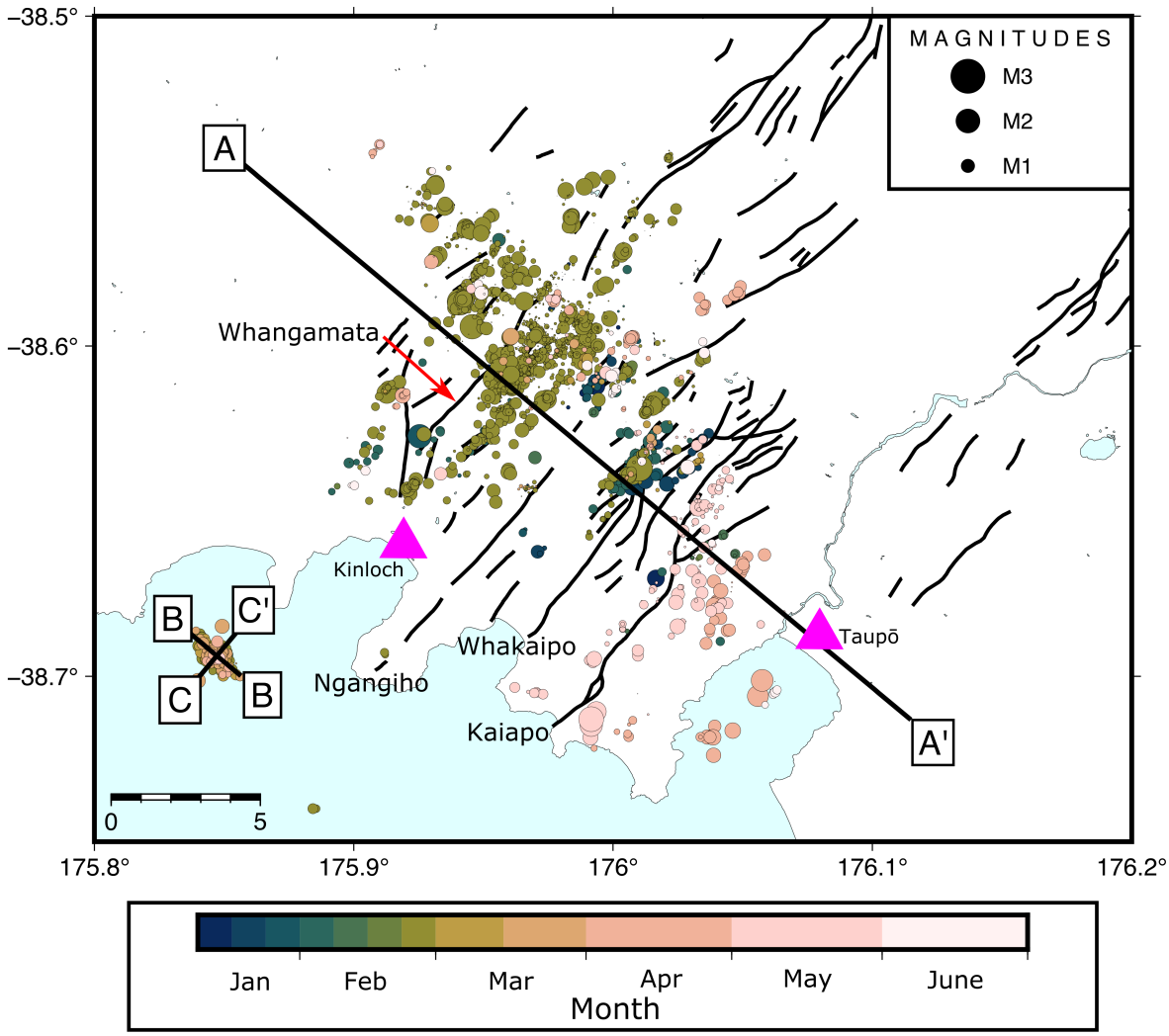

Figure 3.13: A map of relocated earthquakes, as in Figure 3.4, with earthquakes coloured according to their origin time. There are three cross-section lines A,B and C corresponding to Figures 3.14 & 3.14. Distance and magnitude scales are included. Taupō and Kinloch townships are labelled triangles.

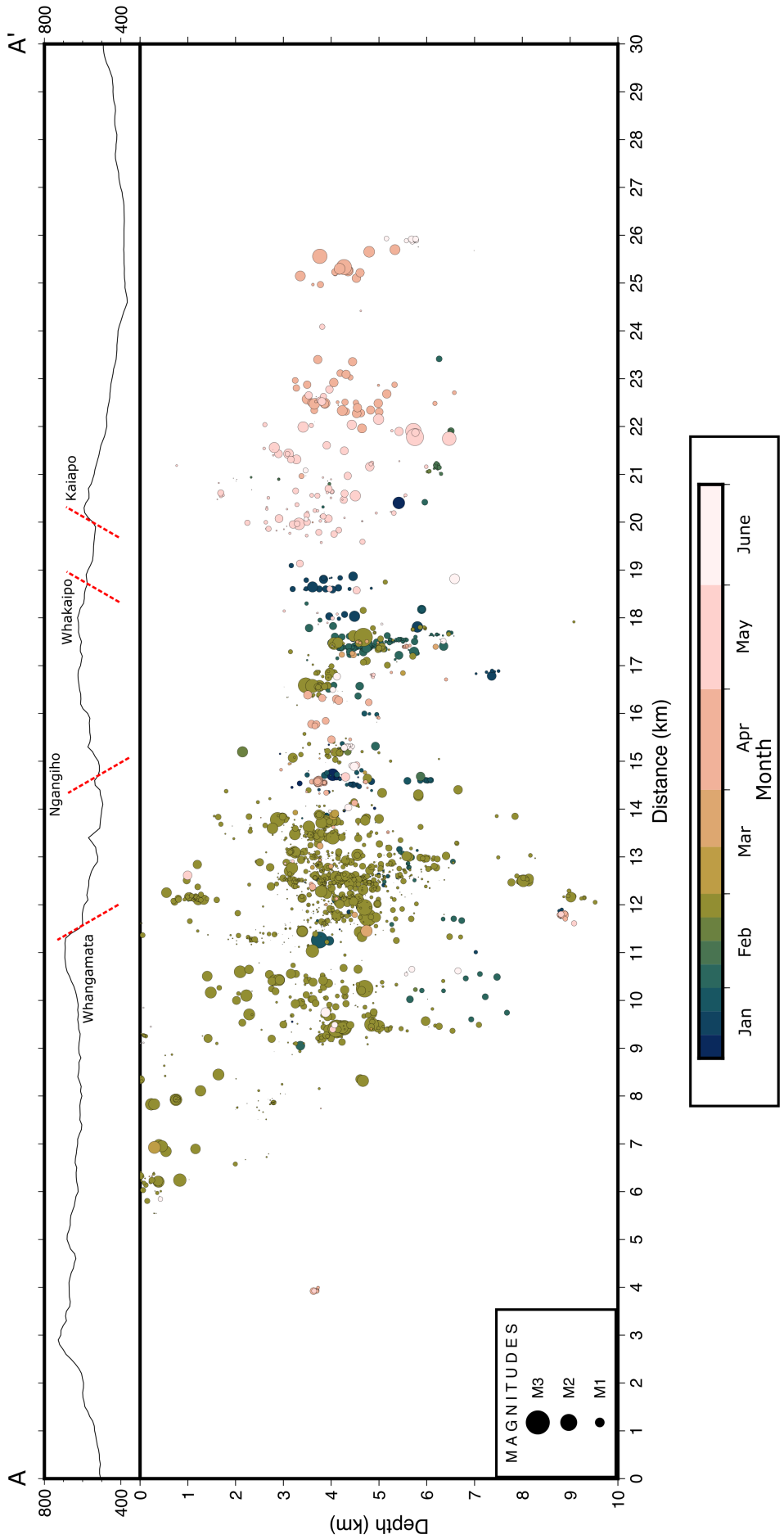

Figure 3.14: Cross-section A from Figure 3.13 showing the events occurring within the Taupō Fault Belt. A magnitude scale is included and topography is overlain (scale in metres). Major faults within the topography have been labelled.

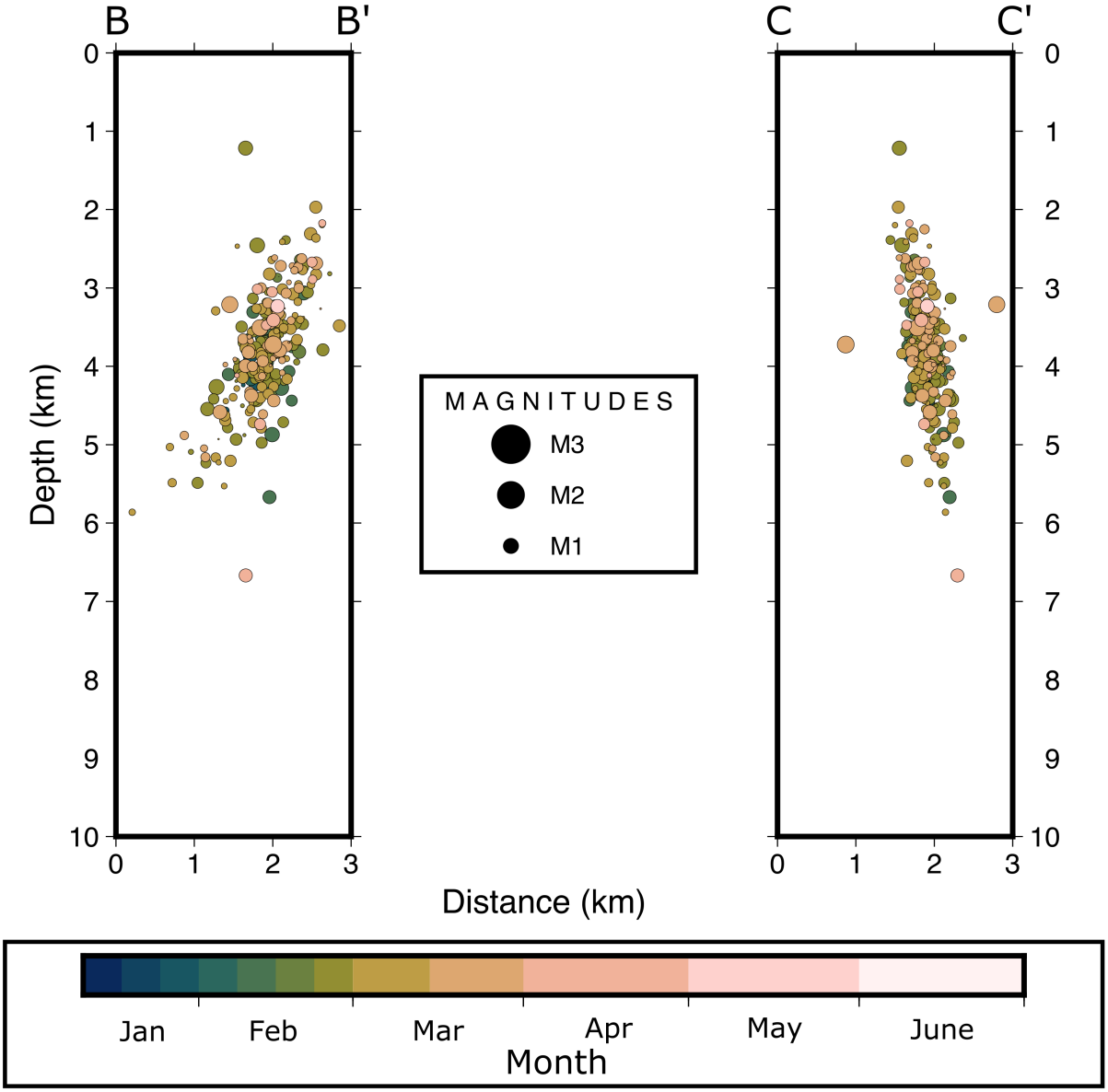

Figure 3.15: Cross-sections B and C from Figure 3.13 showing the events occurring beneath the Western Bay. A magnitude scale is included.

one notable outlier, which is significantly shallower than the majority of events and occurs at approximately 1 km depth. The February earthquakes beneath the lake are uniformly M_L 1.

In contrast to the earthquakes occurring in January and February, the earthquakes detected during March primarily occur outside the Taupō Fault Belt in the Western Bay cluster (Figure 3.13, brown). These events make up around half of this cluster, including the two outliers to the south and north. Events detected in March are uniformly M_L 1, with the largest event being a M_L 1.13 earthquake on the 2nd of March.

Events occurring in April and May have similar distributions, predominantly occurring southeast of the Kaiapo fault (Figure 3.13). The earthquakes occurring in April were relocated in close proximity to Taupō township, although a small number are also seen further northwest. In contrast, earthquakes occurring in May are constrained to the up-thrown side of the Kaiapo Fault. The magnitudes of the earthquakes on the southeastern side of the Kaiapo Fault are consistently between M_L 0.5–1.5, but show increased variation closer to the fault line. Earthquake depths in April are constrained between 3–5 km depth, contrasting with May earthquakes occurring between 1.5–6 km (Figure 3.14). Earthquakes occurring in April and May were also located to a lesser degree in the central and northwestern fault belt, occurring as individual events or as small, tightly constrained clusters. A few individual events are seen in the Western Bay cluster, but these are a significant minority compared to February and March events in this region (Figure 3.15).

The GrowClust relocation process relocated only 68 earthquakes the occurred in June, making it difficult to assess their spatial or temporal distribution. A small cluster of events was located in close proximity to the April cluster beneath Taupō township (Figure 3.14, at 26 km). Apart from this small cluster, earthquakes during June occur as $\leq M_L$ 1 events individually dispersed throughout the fault belt.

3.5 Focal mechanism results

This section displays the results of the focal mechanism calculations achieved using the software package MTfit (Pugh & White, 2018), following the picking of p-wave arrivals for chosen events in snuffler (Heimann et al., 2019). 16 earthquakes from the swarm were chosen based on their magnitude, from which we were able to confidently identify p-wave polarities on multiple stations. Of these 16 earthquakes, ten produced focal

mechanism results beneath the 100,000 sample limit. The magnitudes of these events ranged between a 1.07 M_L earthquake on the 13th of March to a 2.54 M_L event on the 24th of February, with a magnitude cutoff of one. Six earthquakes occurred in February, with the other four split between the months of January and May. The events which occurred in May are notably smaller, recording local magnitudes approximately $\frac{3}{4}$ the size of the others. Six of the ten events produced well constrained focal mechanism solutions which fit the data. The results of the six well constrained or 'successful' focal mechanisms are presented below, along with an explanation of the issues limiting these results.

3.5.1 Well constrained focal mechanisms

Two fault-plane plots have been produced for each of the 'successful' events. The first of these plots shows all potential fault plane orientation pairs for the given event, with the average pair represented by green lines. These plots also display the Kinematic pressure, null and tensile stress axes. The second fault-plane plot shows only the highest-probability orientations of the two possible fault planes associated with this event.

Event 1 occurred on the 30th of January and produced a calculated local magnitude of 2.28 M_L. The earthquake occurred in the northwestern region of the Taupō Fault Belt, close to the Whangamata Fault (Figure 3.16, map). The full focal mechanism plot for event 1 has a large majority of high probability fault plane orientations (darker lines) forming a strike-slip solution with a small normal component, which is supported by the average orientations. This strike-slip solution is further reinforced by the highest-probability pairing of possible fault plane orientations, which shows no overlap between contrasting data points (Figure 3.16, top right). These two plots suggest that strike-slip motion on a fault dipping steeply to either the northwest or northeast best explains the data. Based on the alignment of the focal mechanism with a NE-trending active fault, it is likely the NW-dipping possible plane is the true nodal plane.

A small amount of moderate probability fault plane orientations suggest increased normal motion occurred on a much shallower northwest dipping fault (Figure 3.16, top left). However this solution is less constrained and only contains data in three quadrants, suggesting a more strike-slip solution is appropriate. This result is considered highly reliable, as both extensional and compressional sectors are constrained, increasing our confidence in the resulting plot.

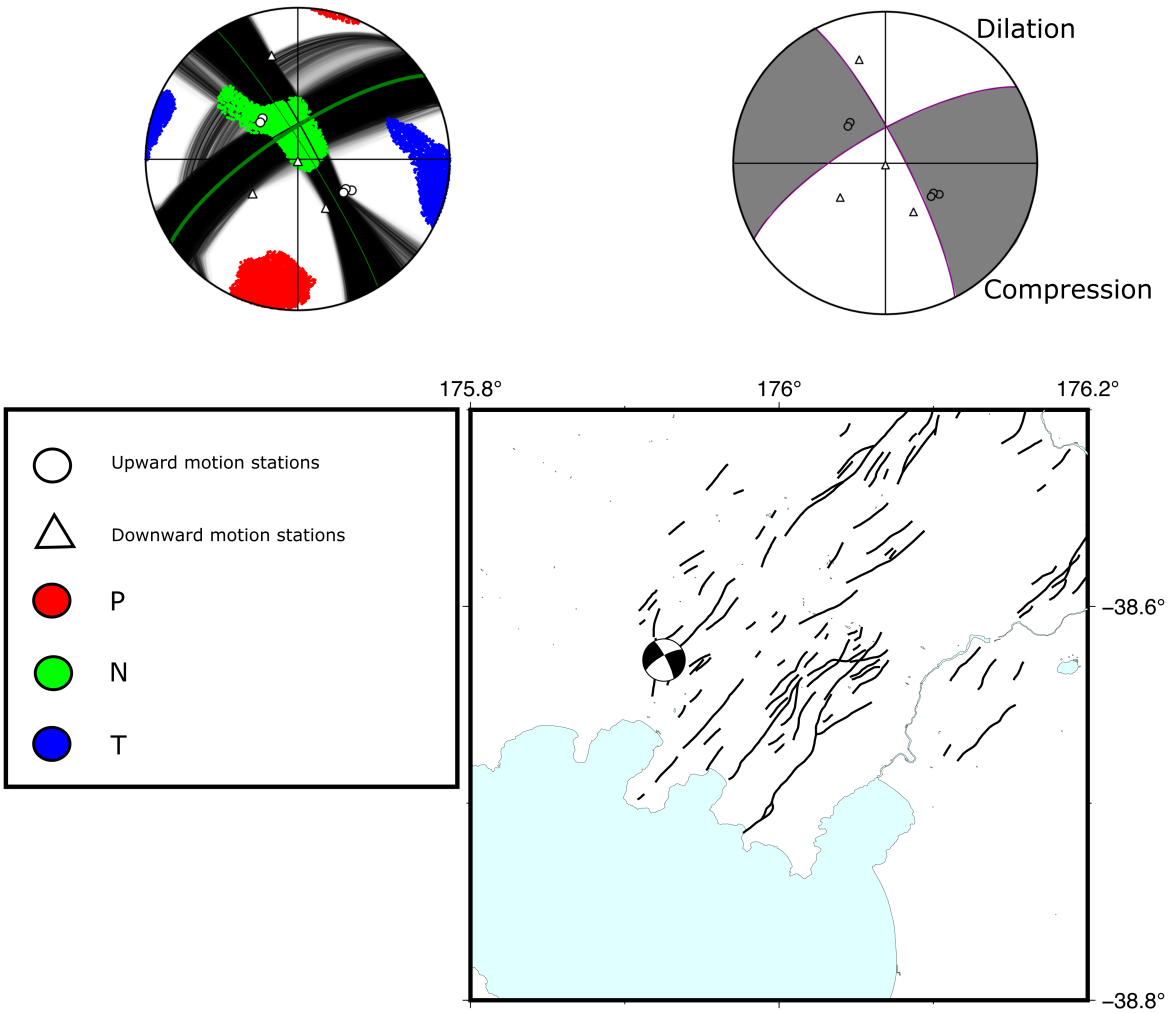

Figure 3.16: This figure consists of three subplots relating to the first focal mechanism result (occurring 01/02/2001). The top left subplot shows all possible fault plane orientations, with darker lines representing higher probability planes and the two green lines marking the average of these. The pressure, null and tensile stress axes are shown in the legend. The top right subplot shows the highest probability pairing of possible fault planes. In both subplots, circles indicate upward first motion at the station, while triangles indicate downward first motion. The bottom subplot is a map view of the focal mechanism, with active faults shown in black.

Event 2 occurred on the 24th of February and produced a calculated local magnitude of 2.54 M_L, making it one of the largest events detected in the entire swarm. This earthquake occurred in the northwestern region of the Taupō Fault Belt, on the northwest side of the Whangamata Fault (Figure 3.17, bottom). Event 2 shows reduced variation in the range of possible fault plane orientations compared to Event 1, with the highest probability orientations suggesting a strike-slip solution with a small reverse component best fits the data (Figure 3.17, top). The average orientation is consistent with the highest probability fault plane orientation, both suggesting oblique strike-slip motion on one of two moderate to steeply dipping faults, dipping either east or south. A small number of potential fault planes suggest the motion could occur on a westward dipping fault rather than eastward, although these are low probability orientations. The higher probability solution also fits the station data available, with most stations recording upward motion occurring in the upper left compressional quadrant. Stations recording downward motion occur in the dilational quadrants to either side, but no data is recorded in the lower right quadrant. This constrains the orientations to slightly oblique rather than true strike-slip. Unlike Event 1, there is some undesirable overlap of stations with opposite motion occurring in the same quadrants. This increases uncertainty in these results, however this overlap is only the case for a small number of stations in close proximity to the nodal plane (Figure 3.17, top-right).

Event 3 is the first of four successful events to have occurred on the 25th of February, during the period of highest seismicity rates in the swarm. Similarly to events 1 and 2, this earthquake occurred in the northwest region of the Taupō Fault Belt in close proximity to the Whangamata Fault and recorded a local magnitude of 2.19 M_L (Figure 3.18, bottom). The average and highest probability fault-plane orientations suggest that oblique normal motion on one of two moderately dipping fault planes, one to the southeast and one to the west, best explains the arrival data associated with this earthquake (Figure 3.18, top). Both fault plane orientations align with nearby active faults so it is difficult to assess which is likely the nodal plane.

There is increased variation in Event 3, with multiple high probability potential fault planes suggesting increasing steepness on the potential west dipping fault. This is reflected in the contrast between the average and highest probability fault plane orientations, in which the latter strongly suggests the motion is normal. Despite variation in the west dipping fault, the southeast dipping potential fault is well constrained across both plots. Additionally, there is increased spread in the pressure, null and tensile stress axes compared to the other focal mechanism results (Figure 3.18, P, N and T).

Event 4 is the third focal mechanism that occurred during the late February cluster,

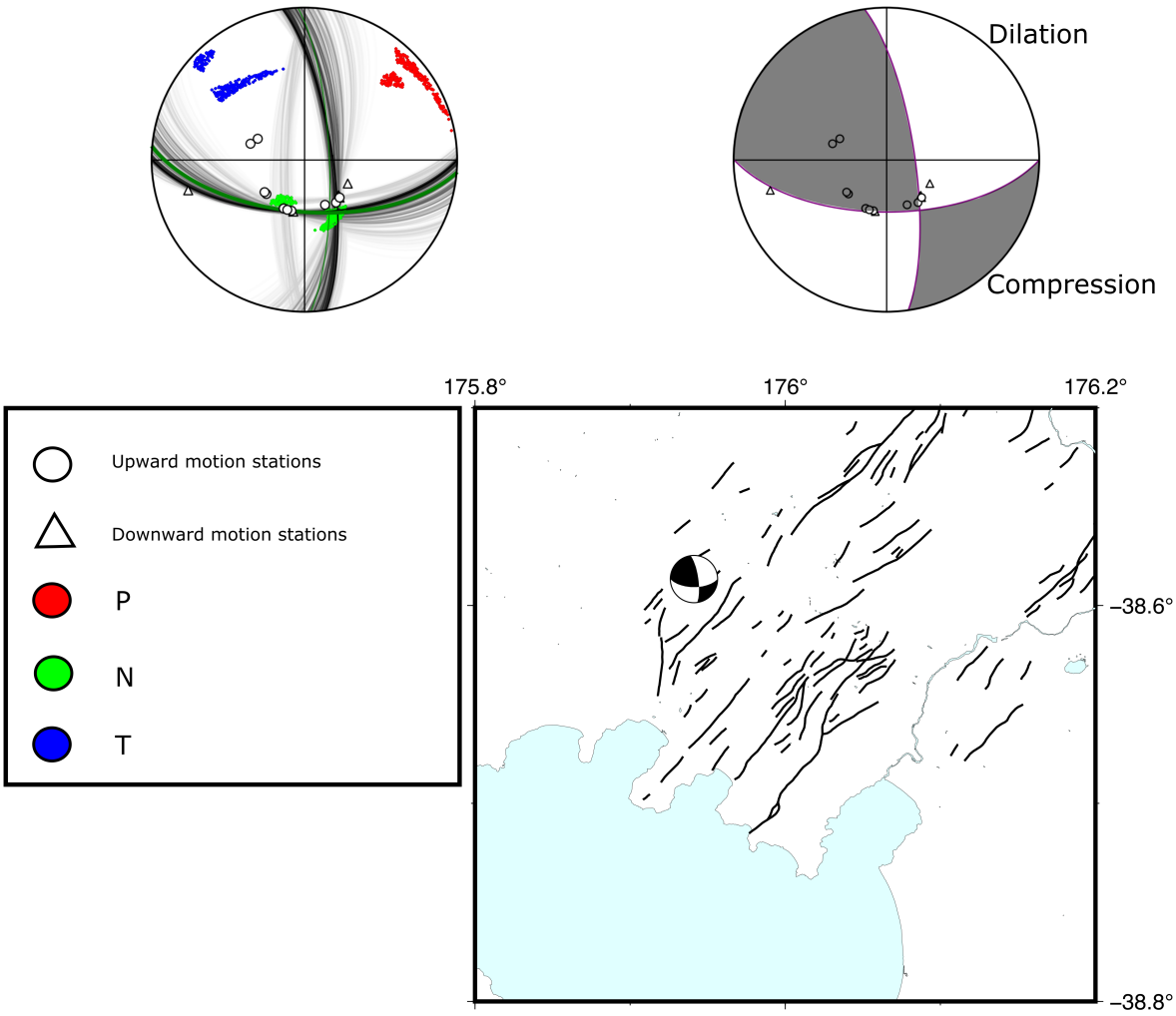

Figure 3.17: This figure consists of three subplots relating to the second focal mechanism result (occurring 24/02/2001), two fault-plane plots above a map of the focal mechanism location. The top left subplot shows all possible fault plane orientations, while the top right subplot shows the highest probability pairing of possible fault planes orientations which could be responsible for this earthquake. The legend is as in Figure 3.16.

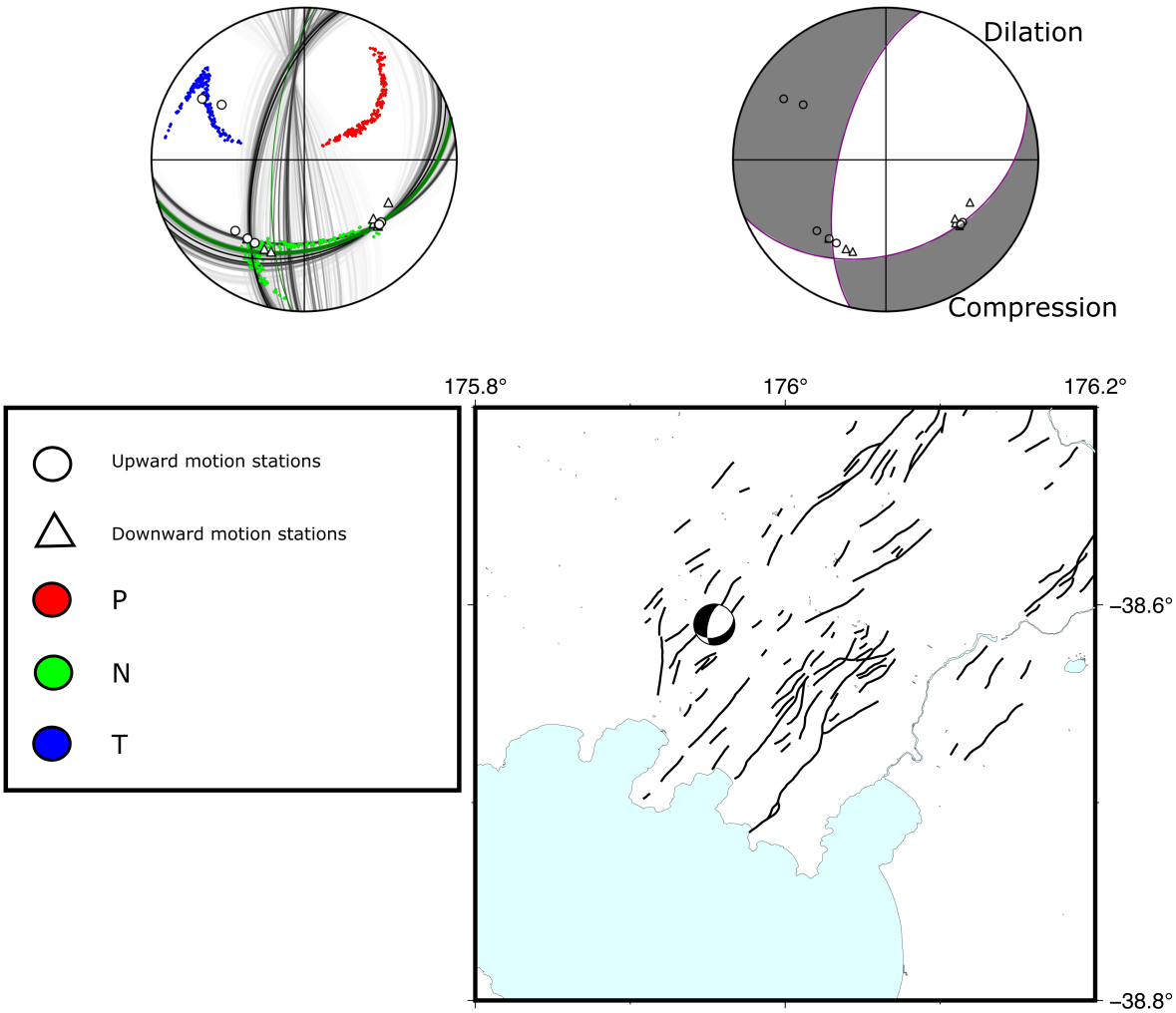

Figure 3.18: This figure consists of three subplots relating to focal mechanism results of the third focal mechanism result (occurring 25/02/2001). Subplots and legends are as in Figures 3.16 & 3.17.

recording a local magnitude of 2.27 M_L and was located adjacent to the Whangamata Fault in the northwestern Taupō Fault Belt (Figure 3.19, bottom). The average and highest probability fault plane orientations are in complete agreement in this case, suggesting that oblique reverse motion on either a moderately northeast dipping or shallowly southwest dipping fault is the best solution for this earthquake (Figure 3.19, top). It should be noted that there is minimal variation in possible fault plane orientations in the full focal mechanism plot, with the arrangement of potential solutions hidden beneath the average. This suggests the solution is well constrained, considering the variation seen in our other focal mechanism results.

However, there is some overlap of station data, with stations recording both upward and downward first motion seen in the upper left quadrant of both fault plane plots. This indicates that the highest probability fault plane orientations still do not explain the station data well. Furthermore, the lower-left dilational quadrant has borderline overlap with a number of upward motion data points, with most station data here occurring near the southwest nodal plane. This is not consistent with the expected arrival locations, which should occur at 45° to the nodal planes. The distribution of the pressure, null and tensile stress axes are also notably reduced in this event.

Event 5 is the final focal mechanism calculated earthquake to occur on the 25th of February, recording a local magnitude of 2.12 M_L. In contrast to previous events, this earthquake was located further southeast in the Taupō Fault Belt (Figure 3.20, map). This is one of the best constrained focal mechanisms, with both the fault plane plots in close agreement. The kinematic axes also have a tight spread, indicating good constraint. These plots suggest that oblique strike-slip motion with a small reverse component on either a steeply east dipping fault or a slightly shallower south dipping fault explains the data (Figure 3.20, top). These steep dips are expected for faults accommodating strike-slip motion.

While this solution explains most of the arrival data well there are some exceptions, most clearly seen in the highest probability fault plane plot (Figure 3.20, top right). Firstly, there are two stations at which compression occurred, close to encroaching on the bottom left dilational quadrant. There is also a single station recording downward dilatational motion (triangle) in the lower-right compressional quadrant. Based on experience picking events in snuffler, this is likely CNIPSE station KIWC, which often displayed the opposite arrival polarity to other nearby CNIPSE stations. This suggests a station error may be responsible for this overlap. Additionally, assuming the top left and bottom right quadrants are accommodating compression, only one of the opposing dilational quadrants actually contains stations with downward first-motion recorded

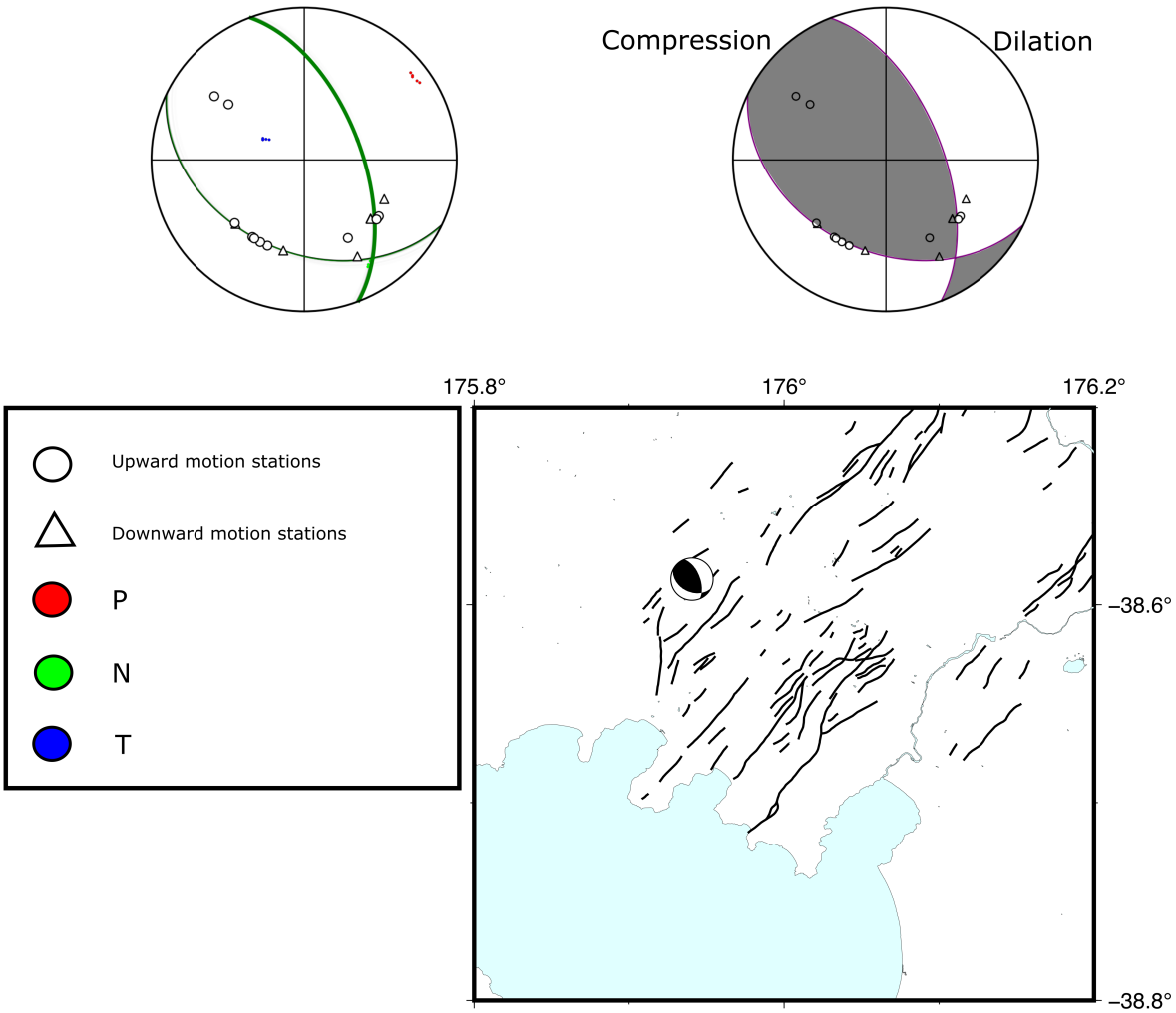

Figure 3.19: This figure consists of three subplots relating to focal mechanism results of the fourth focal mechanism result (occurring 25/02/2001). Subplots and legends are as in Figure 3.16

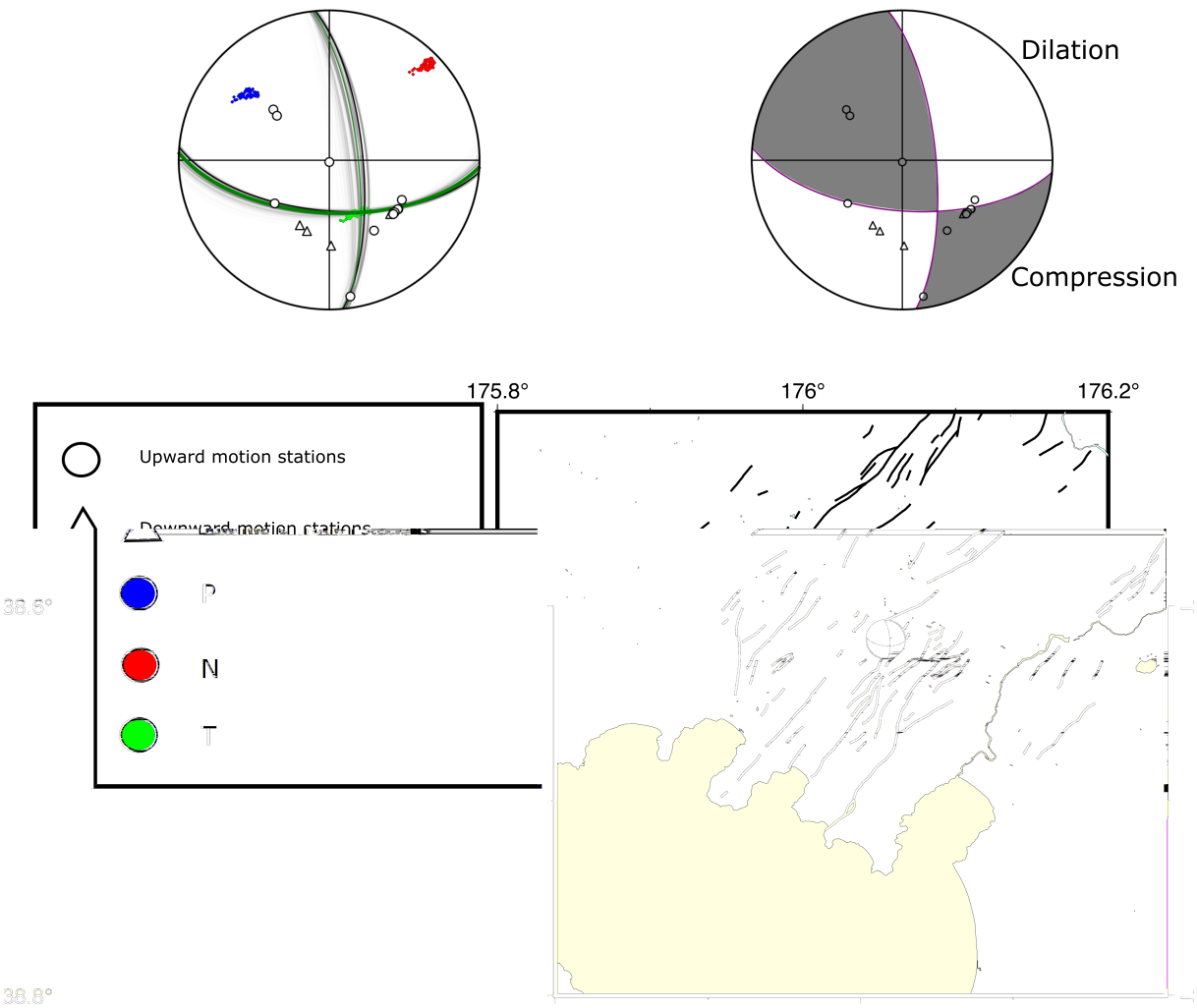

Figure 3.20: This figure consists of three subplots relating to the fifth focal mechanism result (occurring 25/02/2001), two fault-plane plots above a map of the earthquakes location. Subplots and legends are as in Figure 3.16.

(triangles). We would expect to see these stations in the top right quadrant of the fault plane plots, but a lack of data points impacts our ability to constrain the solution.

Event 6 is the final focal mechanism calculation and occurred on the 17th of May, registering a local magnitude value of 1.55 M_L. This earthquake was located in the southeast region of the Taupō Fault Belt, on the down-thrown side of the Kaiapo Fault (Figure 3.21, map). While there is some variation, the majority of possible fault-plane orientations suggest that oblique strike slip motion on either a moderately southeast dipping fault or a steeply dipping northeast dipping fault best explains the arrivals of this earthquake (Figure 3.21, top-left). It is likely the nodal plane corresponds to the southeast dipping fault, as this plane aligns well with the trend of nearby active

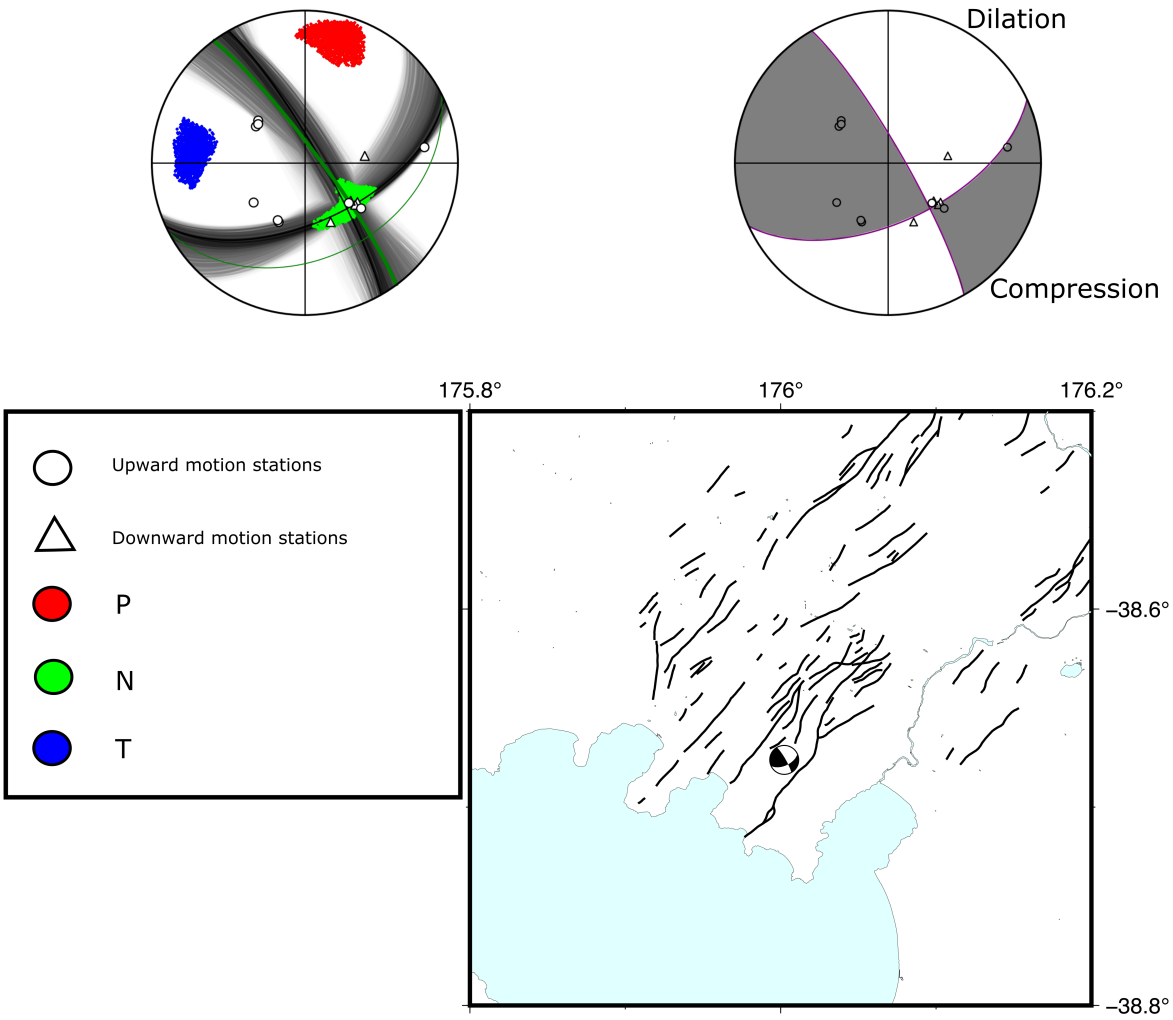

Figure 3.21: This figure consists of three subplots relating to the sixth and final focal mechanism result (occurring 17/05/2001), two fault-plane plots above a map of the earthquakes location. Subplots and legends are as in Figure 3.16

faults. This is in agreement with the highest-probability fault-plane orientation but strangely contrasts with the average, which suggests the possible southeast dipping fault plane is notably shallower. There is a small amount of station overlap seen in the highest probability plot (Figure 3.21, top-right), however this is only the case for two contrasting polarities. The kinematic axes are well constrained in Event 6.

To summarise, we have confidently produced double-couple focal mechanisms for six of the eight highest magnitude events in the swarm. Events 1, 2, 3 and 4 are all located in close proximity, with events 2 and 4 overlapping significantly, centred near the Whangamata Fault in the northwestern region of the Taupō Fault Belt (Figure 3.22, map). Despite their close proximity to the Whangamata Fault, each of these events

are also closely aligned to a number of unidentified active faults. Events 5 and 6 were located further southeast, amongst a cluster of smaller faults bracketed by the Ngangiho and Kaiapo faults. All focal mechanism results suggested some component of strike slip motion could be attributed to these earthquakes. The nature of this component varied, with events 1, 2, 5 and 6 all suggesting fault planes accommodating primarily strike slip motion. Event 1 produced a focal mechanism closest to pure strike-slip, with only a small component of normal motion accompanying this. Event 1 was also the most confidently constrained focal mechanism produced, with no overlap between opposing stations and data points located in every quadrant.

In contrast, events 3 and 4 favoured oblique dip-slip solutions. Interestingly, event 3 suggested oblique normal motion on one of its potential faults was the highest probability solution, while event 4 was the result of oblique reverse motion. There was a small component of strike-slip motion in both these solutions, although this was significantly lower than the other events. Despite the contrasting senses of motion, these events were located in close proximity to events 1 and 2 (Figure 3.22). Generally speaking, there is less variation in potential fault planes in these two events than in the events showing stronger strike-slip components. However, it should be noted that both events 3 and 4 display overlap in their station data, with contrasting data points appearing in the same quadrants. This increases the uncertainty in these results relative to the strike-slip dominated events, which display significantly less overlap. Both also show increased variation in their kinematic axes distribution.

The depth distribution of the successful focal mechanism results is relatively consistent, with all events occurring between 3 and 6 km depth (Figure 3.22, cross-section). The cross-section results also indicate that events 1–4 all occur on the upthrown side of the Whangamata fault, assuming its dip remains consistent at depth. Additionally, Events 2 and 4 are not only located at near identical latitude and longitude values, but also occurred at remarkably close depths. Events 2 and 4 occurred approximately 2.5 hours apart.

3.5.2 Issues with focal mechanism calculation

Of the sixteen earthquakes selected for focal mechanism calculation, only ten produced focal mechanism results within an acceptable sample limit. Only six of these were well constrained. This can be attributed to a number of factors, primarily resulting from the seismometer distribution in 2001. The CNIPSE network was tightly spaced within the Taupō Fault Belt, meaning arrival polarities were easily picked and generally were

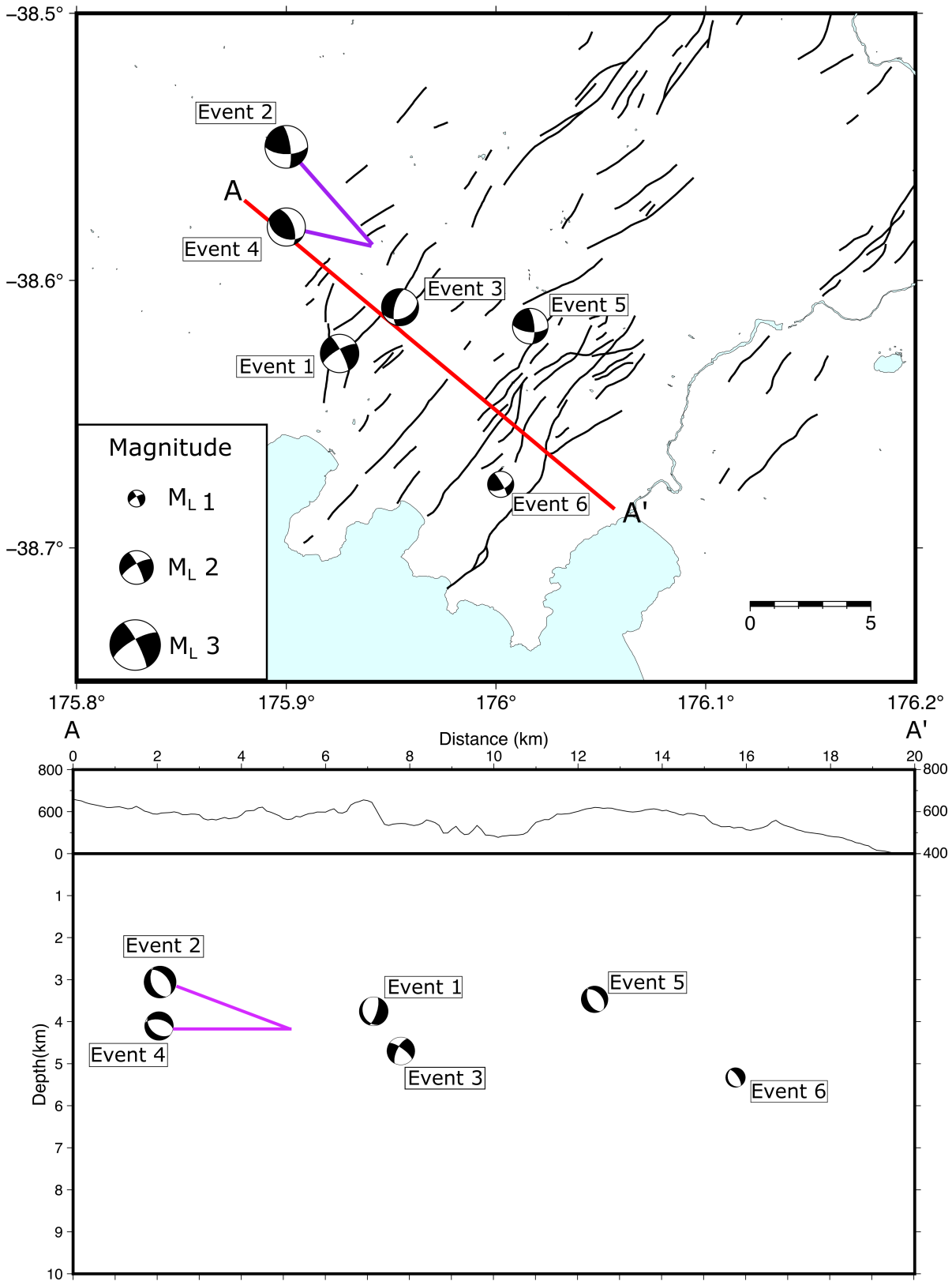

Figure 3.22: Map and cross-sectional view of the six focal mechanism results in the Taupō Fault Belt, with active faults represented in black. Events 2 and 4 overlap so are offset from their original locations via purple lines.

uniform among these stations. Arrival polarities were more difficult to pick on START stations due to distance from the fault belt. With earthquakes of this magnitude, filtered time-series data allows for confident P-arrival picks on START stations for location processes. However, polarities must be determined without any filters applied, as this can alter the waveforms and introduce error (See Section 2.2.6). Removing the bandwidth filter made identifying earthquake first arrivals difficult and very few confident polarity picks could be made on START stations. Confident polarity picks came from the CNIPSE array, in similar areas, and recorded the same sense of motion. A bias towards one sense of motion in our arrival data often made it difficult to accurately constrain the focal mechanism results.

Additionally, CNIPSE and START stations were deployed in two tight groups, perpendicular to the Taupō Fault Belt and around Mt Raupehu (Figure 2.1). This means that the takeoff angles of earthquake rays arriving at these groups of stations, which control their distribution in the fault plane plots, are largely similar and produce clustering of data. This means that even focal mechanisms with an adequate number of data points leave room for further constraint (e.g. Figure 3.19). While we are still confident in these results, especially considering these restrictions, having increased variation in the distribution of seismometers would have likely increased the accuracy of the focal mechanism results.

3.6 Summary of results

Matched-filter detection produced a catalog of 3782 earthquakes over six months in 2001, over 3000 more than GeoNet detected during this time. These events occurred in a step-wise pattern, with a flat, linear trend of ∼200 earthquakes per month interspersed with periods of increased seismicity (Figure 3.8). The most notable of these periods occurred on the 1st and 25th of February and the 17th of May, adding 300, 2000 and 200 earthquakes to the cumulative total respectively. We relocated 2729 of the 3782 detected events in GrowClust and using the relocations, were able to identify a range of earthquake clusters occurring adjacent to active faults within the Taupō Fault Belt. A large elliptical cluster of earthquakes was also identified beneath Taupōs Western Bay (Figure 3.4).

Earthquake distribution in the central and northwestern regions of the fault belt were dominated by earthquakes occurring in February, which form large clusters around the Whangamata Fault. At depth these cluster are nearly vertical, with events ranging

between 1–6 km depth. Interspersed are smaller clusters of events occurring in January, April and May. In contrast to the northwestern fault belt, the southeastern region accommodates very few February events (Figure 3.14) and is dominated by earthquakes occurring in April and May. These events primarily form in clusters, although these are smaller than the earlier ones to the northwest. There is also increased spread in the distribution of April, May and June events in the southeast fault belt, showing less constraint than earlier events to the northwest (Figure 3.9). There is a good amount of magnitude variation in earthquakes occurring through the fault belt, although this reduces moving to the southeast where magnitudes become more uniform. The largest magnitude events in the swarm occur in the central and northwest regions of the fault belt and are closely surrounded by multiple smaller magnitude events.

Events occurring outside the Taupō Fault Belt almost exclusively occur beneath Taupō's Western Bay (Figure 3.4). The spread of earthquakes in this cluster is elliptical and has a depth range of 2–5.5 km (Figure 3.15). This cluster is primarily composed of earthquakes that occurred in February and March, but accommodates a small number of events from January and April too. The magnitude distribution of events in this cluster is relatively consistent, with most events having uniformly $M_L \leq 1$ calculated magnitudes.

We decided to look closer at the three periods of highest seismicity. On the 1st of February, the ∼300 earthquakes form two groupings in the central fault belt, with seismicity resuming after a 45 minute period of quiescence (Figure 3.10). The rift-parallel distribution on this day suggests that events spread from the central fault belt to the southwest (down-rift). The 24th and 25th of February hosted over half the earthquakes in our swarm, with the majority of these events occurring near the Whangamata Fault in the northwest region of the fault belt (Figures 3.13 & 3.11). There were four clusters of seismicity, with the activity starting sequentially and events becoming shallower as clusters become progressively further northwest. The last period of high seismicity was the 17th of May, on which ∼200 earthquakes occurred. Here we see earthquakes occurring in a 2 km band across-rift, in the southeast region of the fault belt (Figure 3.12). There is also evidence in these results to suggest that earthquakes on the 17th were propagating down-rift to the southwest over time.

Following the spatial and temporal results of our relocated earthquakes, we successfully calculated focal mechanisms to represent the moment tensors for six earthquakes within our swarm (Section 3.5). These events were spread throughout the Taupō Fault Belt, with four occurring in the northwest near the Whangamata Fault, one occurring in the centre near the Ngangiho Fault and one occurring in the southeast near the Kaiapo

Fault (Figure 3.22). Four of the six focal mechanism results suggested that oblique strike-slip motion on near vertical faults best explained their arrival data. The other two results suggested oblique normal and oblique reverse motion best explained their data. The events recording normal and reverse motion occurred in the northwestern fault belt, near two other events which produced strike-slip focal mechanisms. The focal mechanisms in the central and southern fault belt both produced oblique strike-slip focal mechanisms. All the focal mechanism results occurred between 3 and 5 km depth regardless of their position across the fault belt.

Chapter 4

Discussion and Conclusions

4.1 Evidence from results at Taupō

We have identified three key areas to address when considering our interpretation. These are the spatial and temporal distribution of the relocated earthquakes and the predominance of strike-slip focal mechanisms.

4.1.1 Western Bay seismicity

An intriguing aspect of the results is the significant number of earthquakes (>200) located beneath Lake Taupō's Western Bay (Figure 3.4). These differ to the majority of swarm earthquake locations, occurring in a historically aseismic area (Potter et al., 2015; Barker et al., 2021). This cluster of low-magnitude ($M_L < 1$) earthquakes occurs at 2–6 km depth and exhibits an elliptical distribution with a ∼2 km spread to the north and south (Figure 3.15). This contrasts with the distribution of the earthquake clusters within the Taupō Fault Belt, which are tightly constrained and aligned with active faults. The elliptical distribution of the Western Bay cluster, it's distance from known active faults and close proximity to the presumed magma reservoir beneath Lake Taupō (Barker et al., 2021; Illsley-Kemp et al., 2021), suggests magmatic unrest may have driven this seismicity.

The Western Bay cluster commenced at the end of January, predating the majority of seismicity occurring within the Taupō Fault Belt (Figure 3.9, top). This is consistent with similar cases at multiple other caldera settings. As discussed in detail in Section 4.2, magmatic intrusions at Yellowstone, Campi Flegrei, Italy, and Cor-

betti caldera in the Main Ethiopian Rift each preceded nearby strike-slip seismicity (La Rocca & Galluzzo, 2019; Lavayssière et al., 2019).

The suggestion of a magmatic intrusion between late January and April at Taupō in 2001 is supported by the results of Peltier et al. (2009). When analysing lake levelling data along the northern shore of Lake Taupō between December 1999 and June 2001, Peltier et al. (2009) argued that an inflating pressure source best explained the deformation patterns seen over this time. However, Peltier et al. (2009) observed minor subsidence (0.005–0.02 m $yr^{-}1$) along the northwestern lake shore, with their preferred model placing the pressure source at ∼11 km beneath the northeastern lake, offshore from the Kaiapo Fault. The lack of uplift recorded at the northwestern lake shore is not inconsistent with our interpretation that a magmatic intrusion occurred in this area.

Firstly, all lake levelling measurements, a proxy for deformation, were taken relative to an origin station on the northeastern shore (Peltier et al., 2009). If this area experiences uplift itself, as in 2001, it can mask uplift at adjacent stations (Otway et al., 2002), possibly obscuring a deformation signal beneath Western Bay. Alternatively, it is possible the intruding body did not produce any observable deformation. Modelling of inflation scenarios at Taupō Volcano indicates that the lake could effectively mask deformation amplitude signals associated with an intruding body (Ellis et al., 2007). We were unable to estimate a volume for the proposed inflating source, but Ellis et al. (2007) estimated that a 35 km^3 intrusion would only produce centimetres of uplift. Given this is the size of the intrusion responsible for the 1.8 ka Taupō Eruption (Ellis et al., 2007), it is likely the suggested Western Bay intrusion was smaller. Hence, a combination of masking by Lake Taupō and uplift in the northeastern region of the lake may have reduced the uplift in the northwestern lake observed by (Peltier et al., 2009). We therefore conclude that the lack of uplift recorded along the western shore of Lake Taupō does not preclude an intrusion being the cause of observed seismicity.

The presence of the Western Bay cluster does not explicitly implicate a magmatic intrusion as opposed to geothermal fluids, although there are no known geothermal fields beneath the Western Bay (Bibby et al., 1995). Therefore, we consider a magmatic intrusion more likely as the cause of the seismicity.

4.1.2 Taupō Fault Belt kinematics and stress field implications

The focal mechanism results we calculated for six earthquakes occurring within the Taupō Fault Belt (Section 3.5) displayed primarily strike-slip mechanisms. As the Taupō Fault Belt is part of the larger Taupō Rift, most identified faults accommodate regional extension through normal, dip-slip motion (Litchfield et al., 2013). This is supported the stress inversion completed by Townend et al. (2012), which defined a predominantly normal stress regime north of Lake Taupō (Massiot et al., 2015; McNamara et al., 2019). Therefore we would expect to produce normal focal mechanisms from earthquakes occurring in this region instead of strike-slip. As mentioned in Section 3.5, due to the low magnitude of the earthquakes during the 2001 swarm and the poor coverage of seismometers at this time, the focal mechanisms produced by MTfit are not as numerous or as well constrained as hoped. Nevertheless, these focal mechanisms can be used to support evidence from the more robust earthquake relocation results.

There is good consistency in the potential fault planes of the strike-slip focal mechanisms, with most producing rift parallel nodal planes. Considering the alignment of the focal mechanisms with active faults, we believe the rift-related nodal planes are the fault planes the focal mechanism earthquakes are occurring on. The strikes of these mechanisms are also in good agreement with the two nodal planes of the normal focal mechanism for Event 3 (Figure 3.22), which strike roughly parallel and antiparallel to the rift.

The type of faulting that predominantly occurs in an area depends on the orientation of crustal stress axes. The principal stress axes, denoted σ^1, σ^2 and σ^3, correspond to the maximum, intermediate and least principle compressive stress directions, respectively (Anderson, 1905, 1951; Simpson, 1997). Related but distinct geometric information is provided by the principal axes of each focal mechanism, which are referred to as the pressure (P, red), null (N, green) and tensile (T, blue) axes. These describe the kinematics of each focal mechanisms, as the pressure and tensile stresses bisect the dilational and compressional quadrants respectively and provide some limited constraint on the geometries of the principal stress axes (McKenzie, 1969; Townend et al., 2006; Arnold & Townend, 2007). In five of the six focal mechanism results we have obtained, the 'T' axis is sub-horizontal and trends northwest to southeast, which broadly coincides with the direction of extensional strain in the Taupō Rift and the orientation of the axis of minimum horizontal compressive stress (σ^3, Townend et al., 2012). Although the 'T' and σ^3 are not equivalent, they are both consistent with the orientation

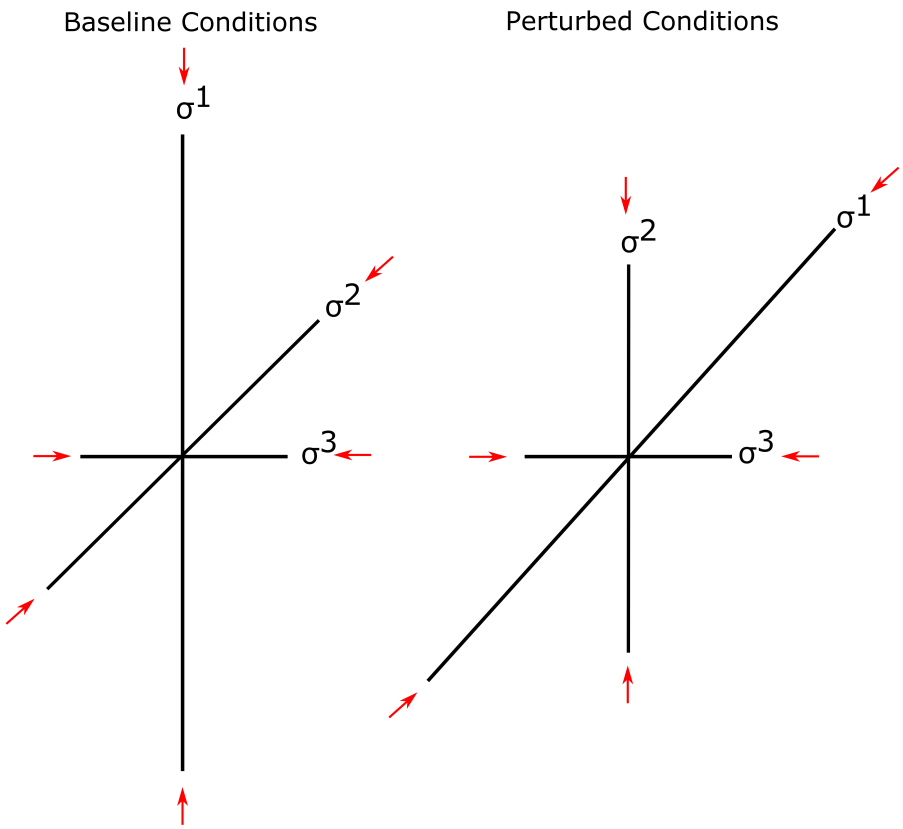

Figure 4.1: A schematic figure showing the proposed temporary rotation of the stress field at Taupō. This shows σ^1 rotating from vertical (left) to horizontal (right) as a result of horizontal pressure. Red arrows indicate compressive stress.

of expected minimum stress within the Taupō Rift.

We do not have enough focal mechanism results to produce a full stress inversion of the area (e.g., Townend et al., 2012). However, the predominance of strike-slip focal mechanisms suggests a vertical σ^2 rather than the vertical σ^1 we would expect to see in a normal stress regime (Anderson, 1905, 1951). Although strike-slip faults can be active in a normal stress field, an alternative interpretation is that the predominance of strike-slip focal mechanisms was the result of a localised change in the stress field, with σ^1 rotating to horizontal (Figure 4.1).

We suggest this stress change is temporal rather than spatial. A spatial change in stress could imply that the Taupō Fault Belt consistently exhibits a locally rotated σ^1, compared to the wider rift. However, this is unlikely due to the kinematics of prominent faults within the Taupō Fault Belt, which accommodate normal motion (Litchfield et al., 2013). Therefore we propose the rotation of σ^1, consistent with our strike-slip focal mechanisms, is a temporal change associated with the intrusion beneath Lake

Taupō's Western Bay. This mirrors similar results at both Campi Flegrei and the Main Ethiopian Rift (Section 4.2), which will be addressed later.

Event 4 (Figure 3.19) is an outlier as the strikes of the two potential fault-planes are rift-perpendicular rather than rift-parallel. Event 4 was located overlying Event 2, matching both the location and depth. Event 2 is a strike-slip focal mechanism, however the strikes of the nodal planes are similar. If the highest probability fault planes in Event 4 were rotated slightly northeast and steepened, these two events would show good agreement as oblique strike-slip focal mechanisms. Additionally, arrival polarities show significant overlap for Event 4, reducing our confidence in the reverse focal mechanism implied. This indicates Event 4 potentially has a larger component of strike-slip motion and may show more consistency with the other focal mechanism results.

To summarise, the focal mechanism results in the Taupō Fault Belt predominantly show strike-slip faulting, consistent with a rotation of σ^1 from vertical to horizontal. The kinematics of faults in this region imply the long-term stress field has a vertical σ^1, suggesting that an external forcing created a local temporal rotation in the principle stress axes, supporting the suggestion of a magmatic intrusion beneath Taupō's Western Bay, first evidenced by seismicity in this area.

4.1.3 Evidence of fluid-based faulting

The spatial and temporal distribution of relocated earthquakes within the Taupō Fault Belt suggest evidence of potential fluid-based faulting, which may have occurred as a product of this intrusion. Fluids can induce faulting by reducing effective normal stress and increasing pore fluid pressure as they propagate along fault planes (Shelly et al., 2013; Russo et al., 2020). Multiple major earthquake swarms in the past have also been associated with fluids escaping from a lithostatically pressured ductile regime into a hydrostatically pressured brittle region (Dzurisin et al., 1994, 2012; Waite & Smith, 2002). Both Yellowstone and the Main Ethiopian Rift show similarities to the proposed Western Bay intrusion and their seismicity was attributed to fluids originated from intruded magma bodies to induce faulting (Shelly et al., 2013; Lavayssière et al., 2019; Russo et al., 2020). These examples will be addressed in Section 4.2.

Earthquakes from 2001 within the Taupō Fault Belt form near-vertical clusters, suggesting they are not representing extension on any of the major four faults. Especially notable is the lack of motion on the Kaiapo Fault during this swarm, despite it being

identified as a strong structural control within the fault belt by Peltier et al. (2009). These four faults, the Whangmata, Ngangiho, Whakaipo and Kaiapo all typically display normal motion and have dips of 60 degrees at the surface (Litchfield et al., 2013). Strike-slip motion is not optimal on dipping faults, but is seen occurring in close proximity to the Whangamata Fault (Figure 3.22). However, this can occur if the dipping fault is sufficiently weak compared to the surrounding rock (Sibson, 1990). This weakening may be the result of increased pore-fluid pressure, caused by the introduction of fluids (Sibson, 1990).

Propagation of seismicity, often indicative of fluids (Shapiro et al., 1997; Parotidis et al., 2003; Hill & Prejean, 2005; Hainzl & Ogata, 2005; Shelly et al., 2013), may have occurred on the 17th of May. Between 17:30 and 18:00, earthquakes initiated in the centre of the Taupō Fault Belt, before moving progressively southwest towards Lake Taupō for approximately 15–20 minutes (Figure 3.12, top). A connection can also be made with the magnitude of these events. May events located near the northeastern portion of the Kaiapo fault are generally $M_L \leq 1$, increasing to $M_L \leq 2$ to the southwest. Near the southwestern terminus of the Kaiapo Fault, at the shore of Lake Taupō, are two of the largest events in the swarm (Figure 3.13), reinforcing this trend. There are some exceptions, with multiple $M_L<1$ earthquakes occurring by the lake, but generally the trend fits our data well.

To summarise, the vertical clustering of Taupō Fault Belt seismicity and alignment with small rift-oriented faults is characteristic of the presence of fluids. This seismicity also shows some evidence of propagation along fault planes, another indicator of possible fluid presence. These observations are given more weight based on their similarities with other examples of fluid based seismicity (Section 4.2).

Temporal evidence of fluid-based faulting

Sustained earthquake rates over time along with a wide spread of earthquake hypocentres are both features indicative of fluid-triggered earthquakes (Sibson, 1996; Hainzl, 2004; Cox, 2005; Wibberley et al., 2008; Ingebritsen & Appold, 2012). While the earthquake count has a step-wise pattern, there is a shallow linear trend of approximately 200 earthquakes per month occurring outside the periods of increased seismicity (Figure 3.8). This indicates seismicity is occurring regularly throughout the first six months of 2001. Furthermore, on days accommodating periods of increased seismicity, earthquakes can be occur continuously for up to 7 hours. Broadly speaking, the relocated earthquakes occur across a large ($\sim 25 \times 20$ km^2) area, a characteristic indicative of

fluid-triggered seismicity (Hainzl, 2004). These distribution characteristics support the spatial evidence of fluid-based faulting.

There is a strong temporal divide either side of the Kaiapo Fault, with earthquakes from the first and second halves of the swarm occurring to the northwest and southeast respectively (Figure 3.14). If seismicity within the Taupō Fault Belt is partially induced by the propagation of fluids, the Kaiapo Fault may be acting as a barrier blocking this propagation during the first half of the swarm.

Evidence of faults acting as barriers to fluid induced seismicity in the Taupō area was displayed in a recent study by Hopp et al. (2020). This seismicity occurred between 2012 and 2015 in the Rotokawa geothermal field, which is compartmentalised by faults blocking inter-compartmental fluid flow (Wallis et al., 2013; Sewell et al., 2015; Addison et al., 2017). Hopp et al. (2020) identified significant variations in calculated b-values for earthquakes in the different 'compartments', with average b-values highest in the compartment closest to the sites of fluid injection. Given pore-fluid pressure is most elevated near the site of injection, this suggests varying amount of fluids in each compartment are causing the disparity in b-values (Hopp et al., 2020). Furthermore, this implies the border faults separating the geothermal field are limiting the fluid propagation into compartments further from the site of fluid injection. Another example of this was seen at an Enhanced Geothermal Systems (EGS) borehole beneath Basel in Switzerland, where b-values increase above 2.0 near the site of injection (C. E. Bachmann et al., 2012; Hopp et al., 2020). Hence, the Kaiapo Fault may be acting as a similar barrier. It has already been identified as a strong structural control in the Taupō Fault Belt and was involved in further deformation in the months following the swarm (Peltier et al., 2009).

4.1.4 Faulting evidence of increased stress

In addition to evidence of fluid propagation, the period of highest seismicity in the swarm shows evidence of stress-induced faulting. Earthquakes that occurred on the 24th and 25th of February show strong spatial segregation, in four distinct locations across the Taupō Fault Belt. The largest cluster occurred adjacent to the Whangamata Fault (Figure 3.13), with three clusters of diminishing size to the northwest (Figure 3.11, middle). There is a clear offset in the initiation of earthquakes at these sites. The largest, central cluster initiates at approximately 23:10, following which seismicity begins 3–4 km northwest approximately 10 minutes later. This is followed by two more earthquake clusters, each occurring 1 km further northwest and initiating

10 minutes after their predecessor.

This creates a progression of earthquake clusters across the fault belt, initiating sequentially to the northwest. The sequential nature of these clusters suggests each one is being triggered by its predecessor. As the initial fault ruptures, stress is transferred onto the adjacent fault, which then ruptures and continues the cycle. This does not adhere to the hallmarks of fluid propagation, where fluids move along the strike of a fault but rarely jump across multiple faults (Shelly et al., 2013). The four clusters are also shallowing from ∼5 to <1 km depth moving northwest (Figure 3.11, middle), which is significantly shallower than the majority of earthquakes occurring in the Taupō Fault Belt. We therefore suggest that the earthquake cluster adjacent to the Whangamata fault is triggering earthquakes on smaller, increasingly shallow fault planes to the northwest. This is consistent with the mapped results of our relocated events, which shows February earthquake clusters align closely with parallel active faults in the northwest region of the Taupō Fault Belt (Figure 3.13).

Stress induced faulting is not unexpected. An intrusion of magma beneath the Western Bay would apply a significant horizontal pressure, indicated by the inferred rotation of σ^1. This pressure can increase differential stress in the overlying rock and drive it towards brittle failure (Rowland et al., 2010). Dike-induced stress changes have been known to encourage fault slip (Rubin & Pollard, 1988). Fluid and stress triggered seismicity can also coexist within the same swarm, both acting as primary processes (Parotidis et al., 2005; Hainzl & Ogata, 2005; Shelly et al., 2013). We believe the spatial distribution of earthquakes displays evidence of this coexistence of faulting mechanisms occurring at Taupō, which is consistent with an intrusive seismicity source.

4.2 Comparing Taupō with analogous calderas

As mentioned in Section 4.1, despite occurring in the actively extending Taupō Fault Belt (Rowland et al., 2010), we see a predominance of strike-slip focal mechanisms and evidence of fluid-driven seismicity. Similar patterns of seismicity have been reported at other calderas elsewhere. We have chosen to focus on periods of seismicity at three of these analogous settings, which support the interpretations we have made for Taupō. These periods of seismicity occur at Yellowstone caldera, Campi Flegrei caldera and the Main Ethiopian Rift (Russo et al., 2020; La Rocca & Galluzzo, 2019; Lavayssière et al., 2019).

4.2.1 Yellowstone

Yellowstone is located in the western United States and is part of the Intermountain Seismic Belt, characterized by high volcanic and seismic activity (Smith & Arabasz, 1991; Farrell et al., 2009). Crucially, seismicity commonly forms swarms showing significant spatial and temporal clustering (Farrell et al., 2009; Massin et al., 2013). Seismicity recorded between 2010 and 2016, including the 2010 Madison Plateau swarm (Figure 4.2), displayed a mixture of strike-slip and normal faulting around the edge of the 0.63 Ma caldera (Russo et al., 2020). The presence of normal faulting is expected here as the volcanic plateau is part of the Basin and Range Province, which is undergoing tectonic extension (Christiansen, 2001). This mirrors the focal mechanisms at Taupō, where strike-slip faulting occurred within a typically normal-faulting stress field. However, the strike of extensional faults in this region is variable (Doser, 1985; Eddington et al., 1986; Zoback, 1992) and does not share the uniformity of the Taupō Rift.

The predominance of strike-slip focal mechanisms at Yellowstone was attributed to an intruding sill, although alignment of earthquake clusters with Quaternary normal faults indicates regional tectonics were also influential (Russo et al., 2020). The intruding sill provided a reservoir of exsolved fluids, which accumulated in horizontal lenses, below the brittle-ductile transition (Fournier, 1999; Smith et al., 2009). The fluids migrated laterally (Figure 4.3), trapped by overlying low-permeability rocks, from a near-lithostatic regime to a near-hydrostatic regime as they cross the brittle-ductile transition (Fournier, 1999; Gudmundsson, 2011; Geshi et al., 2012). This induces faulting by reducing normal stress and increasing pore fluid pressure, as the fluids travel along pre-existing fault planes (Shelly et al., 2013; Russo et al., 2020). Additionally, the fluid over-pressure induces horizontal propagation along existing fractures/faults and in turn creates new fractures accommodating strike-slip motion (Pollard & Holzhausen, 1979; Bonafede & Olivieri, 1995; Russo et al., 2020). This fluid based solution is supported by the diffusive pattern of earthquake distribution, with events migrating up and down-dip from the origin (Shapiro et al., 1997; Parotidis et al., 2003; Hill & Prejean, 2005; Hainzl & Ogata, 2005; Shelly et al., 2013). We see evidence of similar propagation in the southeast region of the Taupō Fault Belt on the 17th of May (Figure 3.12).

The strike-slip earthquakes from the Madison Plateau swarm in 2010 occurred in largely vertical clusters. This is similar to the spatial distribution of seismicity occurring in the Taupō Fault Belt, implicating fluids as a potential driver. We have interpreted

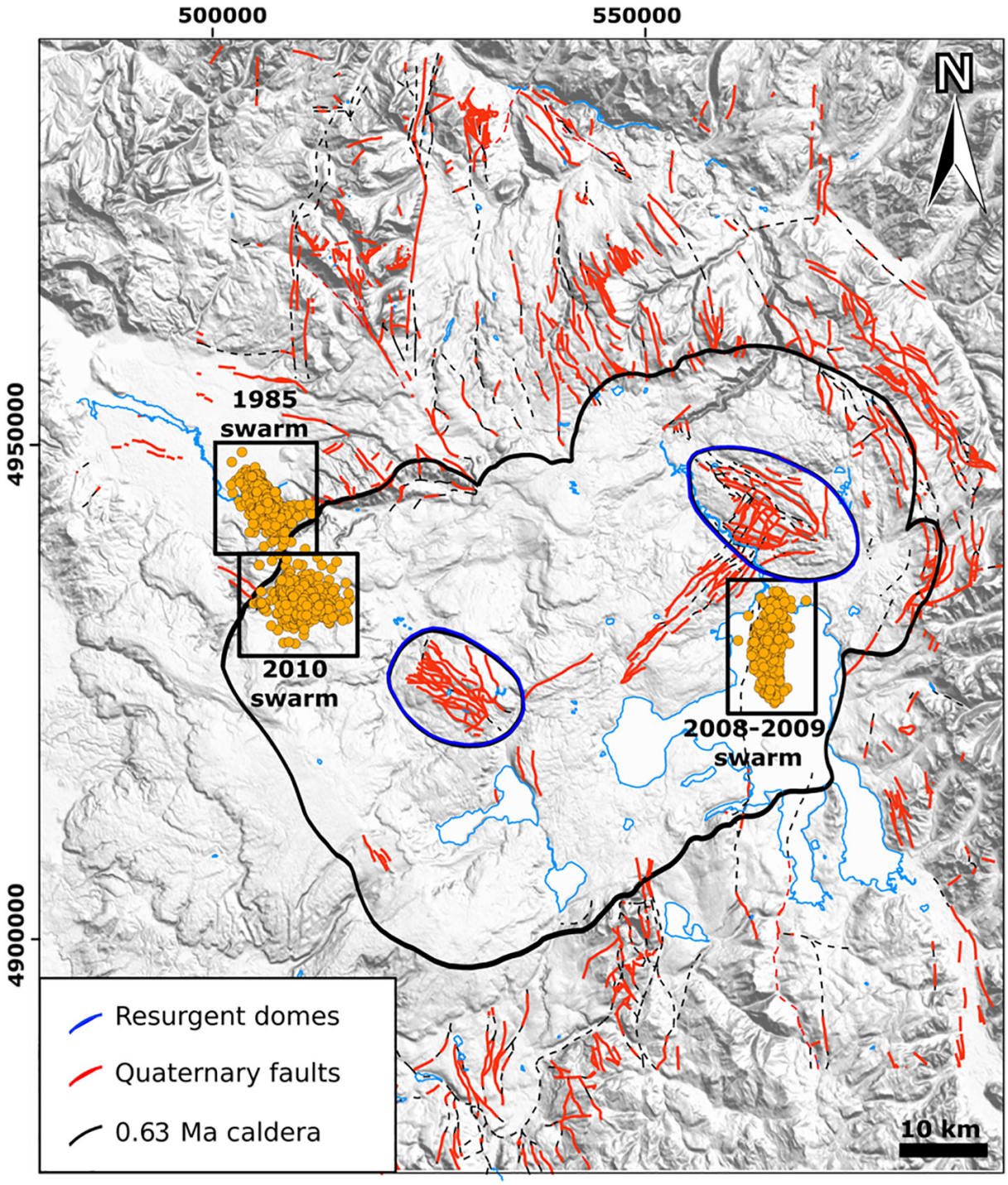

Figure 4.2: Seismic swarms in the Yellowstone volcanic plateau. The 0.63Ma Yellowstone caldera represented in black, with active faults (Christiansen, 2001) in red and resurgent domes in blue. Earthquake catalog is from USGS Earthquake Hazards program. This figure has been taken from Russo et al. (2020).

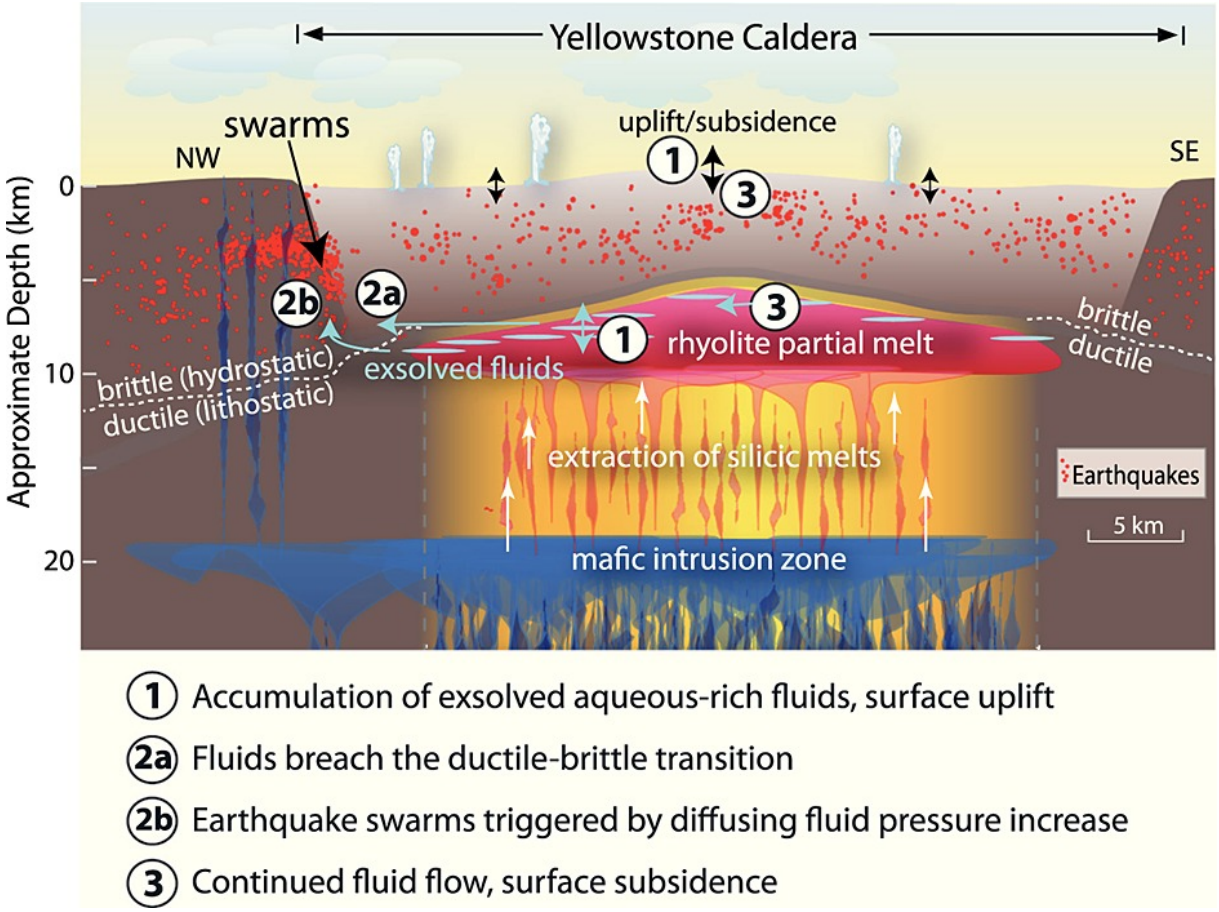

Figure 4.3: Schematic cross-section by Shelly et al. (2013) showing the relationship between fluids and earthquake swarms adjacent to the caldera. Shelly et al. (2013) suggest that fluids become exsolved from the intruding sill before transitioning across the brittle-ductile transition and increasing pore-fluid pressure in the brittle regime. This induces seismicity.

the Western Bay cluster an intrusion, matching the sill intruded prior to the Madison Plateau swarm which provided a source of fluids. Therefore suggest this analogue supports the hypothesis that fluids originating from the Western Bay intrusion induced a significant amount of seismicity in this area in 2001.

4.2.2 Campi Flegrei

Another analogue for Taupō is Campi Flegrei, a partially submerged collapse structure located west of Naples in Italy (D'Auria et al., 2015). Campi Flegrei is situated at the northeastern terminus of the Tyrrhenian back-arc basin, which is actively undergoing extension (Milia et al., 2013). This back-arc basin is home to complex regional tectonic processes, reflected in the diversity of strike distribution amongst earthquakes recorded around Campi Flegrei (La Rocca & Galluzzo, 2019). When investigating seismicity at Campi Flegrei between 2000 and 2019, La Rocca & Galluzzo (2019) found the majority of earthquakes recorded either a high angle normal focal mechanism or a strike-slip mechanism (Figure 4.4).

Earthquakes during this time frame were low magnitude ($< 2.5 M_L$) and aligned with small faults within the central caldera as opposed to the few large identified faults (Vitale & Isaia, 2014; La Rocca & Galluzzo, 2019). We have seen this pattern of seismicity occurring on smaller faults in a zone of established extension in both the long-term seismicity at Yellowstone and at Taupō in 2001. The seismicity at Campi Flegrei was located in the area that recorded the most significant uplift, suggesting that an inflating source is responsible for triggering seismicity on the faults in this area (La Rocca & Galluzzo, 2019). This uplift, adjacent to the seismicity, created a horizontal tensile stress field, increasing horizontal stresses in the area while reducing the normal stress on high angle faults and favouring strike-slip faulting (La Rocca & Galluzzo, 2019). Strike orientations of events at Campi Flegrei were highly variable, showing no preferential direction (La Rocca & Galluzzo, 2019). When determining the stress-field, the stress axes showed similar variation, although there was enough consistency to determine that the primary compressional stress was vertical and the average inclination of tensile stress was horizontal (La Rocca & Galluzzo, 2019). The scattered stress field distribution and strike orientations indicate the regional stress field at Campi Flegrei caldera does not play an important role in the production of seismicity.

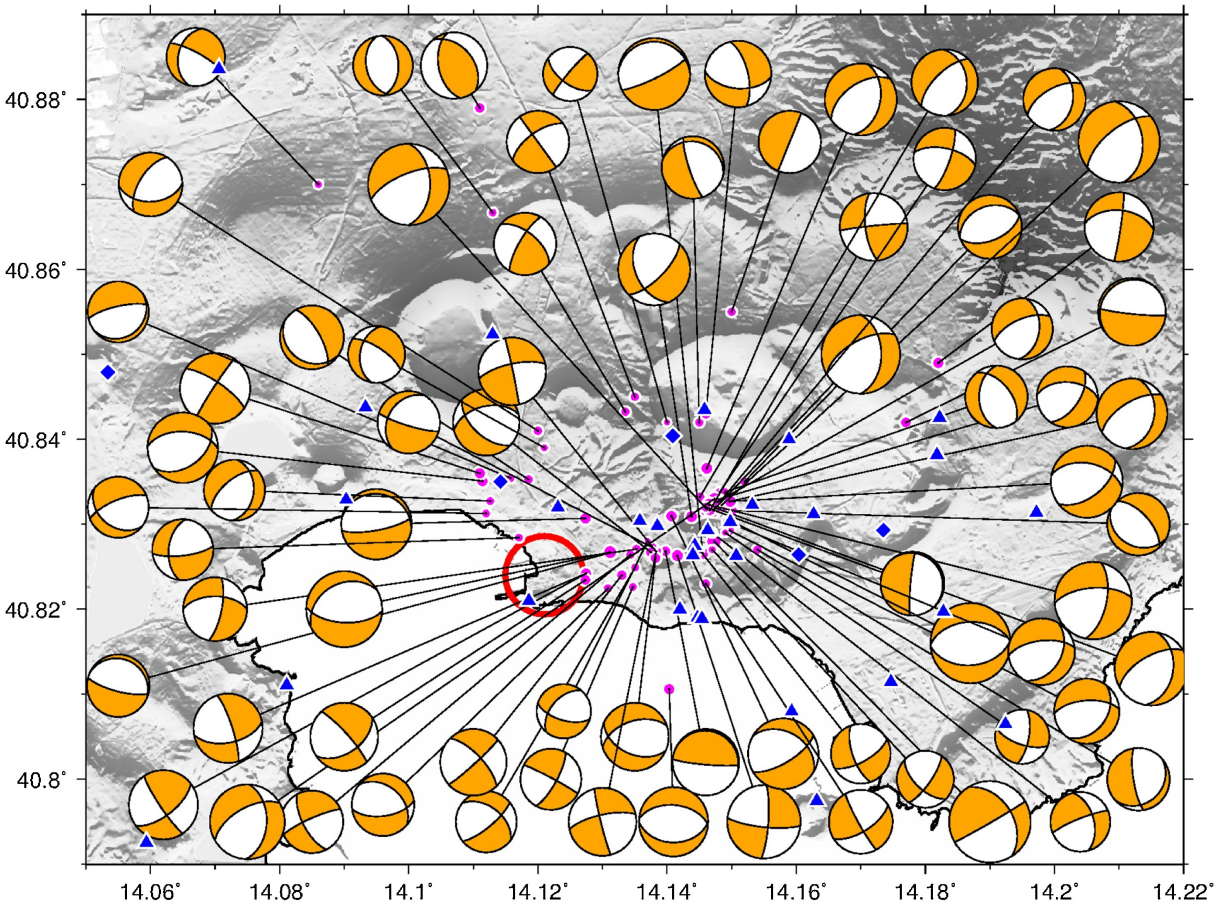

Figure 4.4: Focal mechanism results from seismicity at Campi Flegrei by La Rocca & Galluzzo (2019), indicating a mixture of normal and strike-slip faulting. Seismic stations are shown in blue, while the nearby town of Pozzuoli is circled in red. Figure taken from La Rocca & Galluzzo (2019).

4.2.3 Main Ethiopian Rift

The final analogue for the 2001 seismicity associated with Taupō is the seismicity seen near Corbetti Volcano in the Main Ethiopian Rift (MER). The Main Ethiopian Rift is a magmatically active portion of the East African Rift System lying between the Afar and Turkana depressions to the north and south, respectively (Lavayssière et al., 2019). The MER strikes NNE-SSW and is rifting ∼6 mm/year (Saria et al., 2014; Stamps et al., 2018), similarly to the Taupō Fault Belt (Darby et al., 2000; Wallace et al., 2004). It is seismically active, with normal faulting occurring at border faults and near volcanic centres such as Corbetti caldera (Lavayssière et al., 2019).

Earthquakes were detected at Corbetti volcano over an 18 month period between February 2016 and October 2017 (Lavayssière et al., 2019) and were located between 0–10 km depth (Figure 4.5). There was a range of strike-slip and thrust mechanisms in events both along the caldera rim and in clusters near volcanic vents (Lavayssière et al., 2019), in contrast to the dominant normal dip-slip regional stress. A pre-existing fault structure cross-cuts beneath the Corbetti caldera (Gíslason et al., 2015). Seismicity in the region is situated north of the structure, implicating it as an impermeable barrier directing fluid migration north (Gíslason et al., 2015; Lloyd, Biggs, Wilks, et al., 2018). The distribution of seismicity at Corbetti is therefore consistent with strike-slip motion induced by pore fluid pressure changes resulting from upwelling fluids forced north by this structure.

In addition to an increase in seismicity, the strike of earthquake clusters changes significantly north of the cross-fault structure. It is likely that the original alignment was the result of the rift-related stress field while progression a north-south alignment was due to the north-ward migration of the initiating fluids (Lavayssière et al., 2019). This change in the stress field is supported by seismic anisotropy, which shows a NS orientation north of the cross-rift structure (Lavayssière et al., 2019). This contrast in stress change and the dominance of strike-slip focal mechanisms at Corbetti compared to the rest of the rift indicates that the uplift beneath the caldera was sufficient to modify the stress field. Pressurisation or inflation of a horizontal dislocation or sill is consistent with uplift observations and would locally increase horizontal stress above vertical stress, changing the stress field (Lloyd, Biggs, Birhanu, et al., 2018). This rotates σ^1 to horizontal and produces strike-slip motion on faults, causing slip due to increased pore fluid pressure resulting from fluid upwelling off the inflating source (Lavayssière et al., 2019).

There are strong similarities between the earthquake and focal mechanism distributions

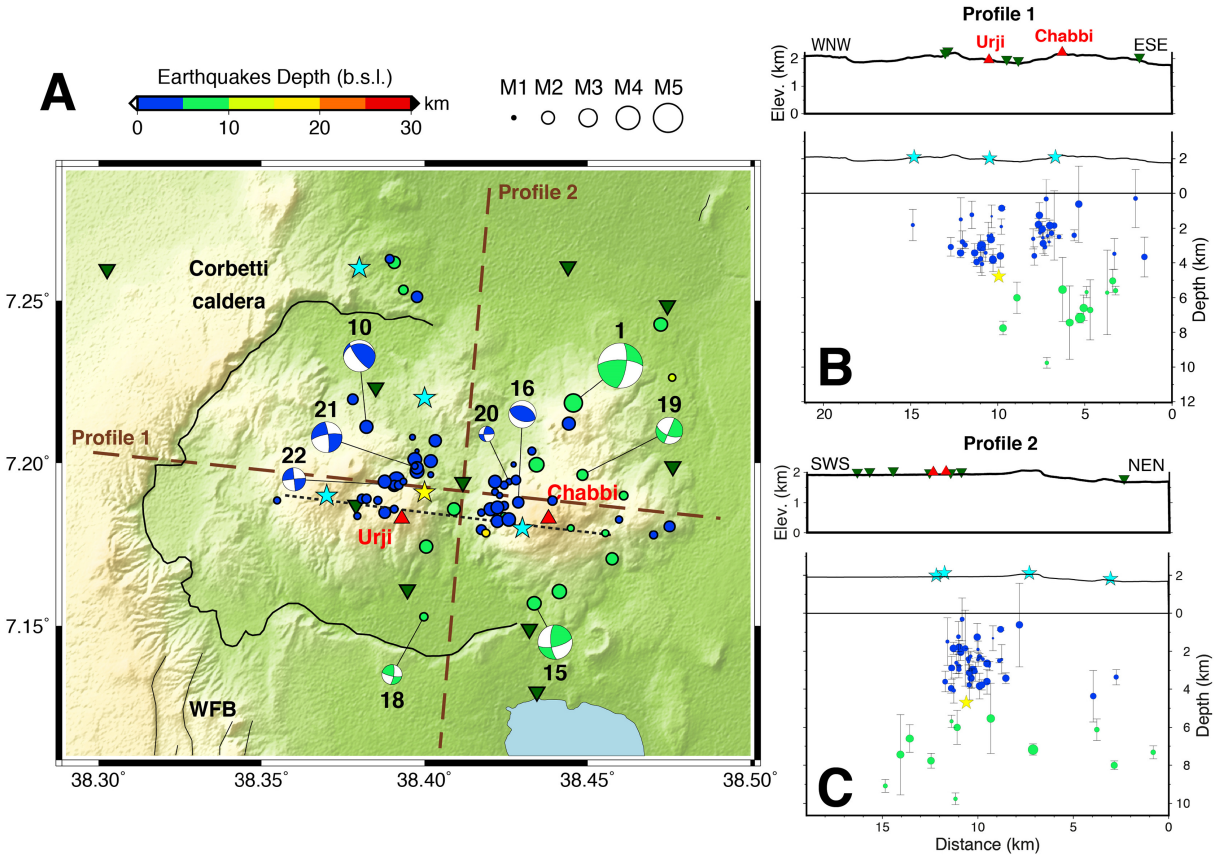

Figure 4.5: Map and cross-sections of seismicity and focal mechanism results from Corbetti caldera in the Main Ethiopian Rift, taken from Lavayssière et al. (2019). Green inverted triangles are seismic stations, red triangles are the two main volcanic centres. The black dashed line shows the cross-rift fault structure identified by Lloyd, Biggs, Wilks, et al. (2018).

to those observed here and at Taupō in 2001. This supports the suggestion that a similarly intrusive source may be the result of the Taupō Fault Belt seismicity.

4.2.4 Summary

Based on the evidence at Taupō and similarities with multiple intrusion events at other calderas, we believe the seismicity beneath Lake Taupō's Western Bay is the result of a magmatic intrusion (Figure 4.6). This inflating body is identified primarily by the relocated elliptical cluster of earthquakes beneath Western Bay. The horizontal pressure from this body caused a temporal rotation in the axis of maximum compressive stress (σ^1) to horizontal, favouring the onset of seismicity with strike-slip focal mechanisms throughout the Taupō Fault Belt. This is consistent with magma-induced stress changes inferred at Campi Flegrei and the Main Ethiopian Rift. At both calderas, the large number of strike-slip focal mechanisms were attributed to a rotation of σ^1 resulting from the increase in horizontal pressure from an intruding source (La Rocca & Galluzzo, 2019; Lavayssière et al., 2019)). The focal mechanism results produced at Taupō are consistent with this pattern.

The increased horizontal pressure from the intrusion likely combined with exsolved fluids to induce the resulting seismicity in the Taupō Fault Belt (Figure 4.6). We have inferred this based on the proposed intrusion and the spatial distribution of the relocated seismicity, which forms vertical clusters aligned with small faults similarly to those seen in fluid-induced swarms at Yellowstone and the Main Ethiopian Rift.

The majority of Taupō Fault Belt seismicity also occurred after the unrest beneath the Western Bay. In each of the three analogous caldera settings, seismicity was preceded by and attributed to intrusion or inflation of a horizontal magmatic body (Russo et al., 2020; La Rocca & Galluzzo, 2019; Lavayssière et al., 2019). This supports magmatic intrusion as the driver of fault belt seismicity at the Taupō Fault Belt in 2001. The spatial distribution of earthquakes and propagation of seismicity both along faults and across the fault belt are similar to patterns observed during the Madison Plateau swarm (Shelly et al., 2013; Russo et al., 2020). This suggests that exsolved fluids from the Western Bay intruded source likely induced some of the fault belt seismicity. Based on the evidence from Taupō and its strong similarities to periods of well constrained, intrusion-induced seismicity, we are confident in attributing the seismicity at Taupō in 2001 to an intrusion beneath the Western Bay (Figure 4.6).

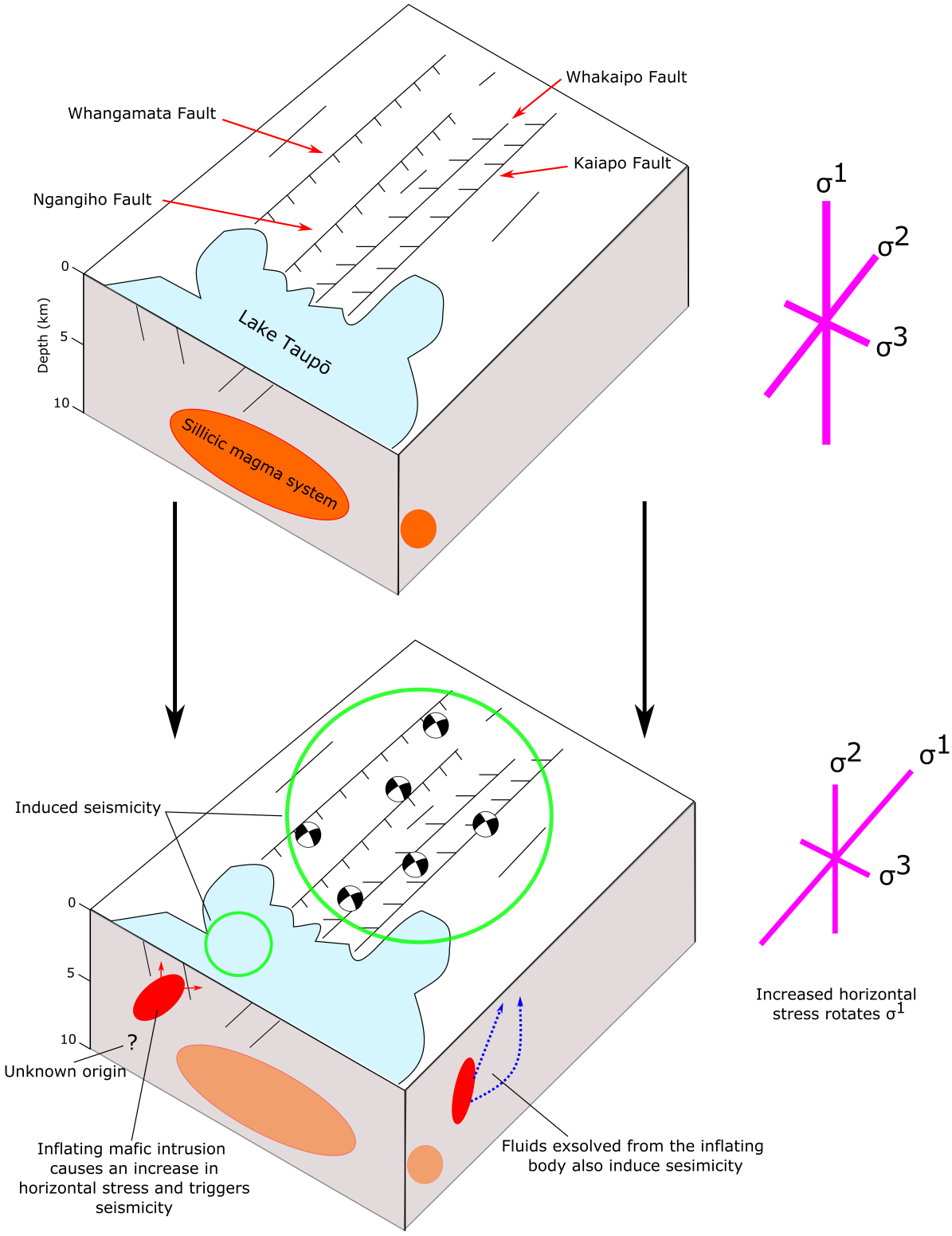

Figure 4.6: Schematic showing the normal stress conditions around Taupō, including a labelled representation of the magma reservoir (top). The bottom plot shows the introduction of the proposed intruding magma body, which increases horizontal pressure and changes the stress axes. Fluids can also be seen exsolving from the intrusion, inducing strike slip seismicity in the fault belt.

4.3 Magma-tectonic interaction

4.3.1 Mafic-tectonic interaction

The results of this research suggest that the Western Bay intrusion had a significant role in triggering seismicity within the Taupō Fault Belt. Interaction between the magmatic and tectonic systems is not uncommon in the central Taupō Volcanic Zone. There is evidence that stress-related diking contributed to the initiation and termination of eruption phases during the Oruanui supereruption in 25.5 ka (Allan et al., 2012). Rowland et al. (2010) also proposed a three-way coupling system, linking the tectonic stress state to the silicic and mafic magmatic systems in the central Taupō Volcanic Zone. This system depends on three variables: mafic magmastatic pressure, differential stress in the crust and the percentage of the shallow silicic 'hot zone' likely to undergo partial melting, which together control the varying methods of accommodating extension in the TVZ (Rowland et al., 2010).

This was further expanded on by the work of Muirhead et al. (2022), who suggest the presence or absence of eruptible melt bodies is critical in dictating the outcome of mafic recharge or tectonic processes. Both mafic recharge and tectonic processes have the potential to trigger the formation and eruption of a melt body within the shallow silicic system (Leonard et al., 2002; Davis et al., 2007; Baer et al., 2008; Allan et al., 2012). Muirhead et al. (2022) outlined six potential outcomes of volcano-tectonic interactions at Taupō Volcano. Outcomes 2 and 5, which envision mafic bodies stalling in the crust having either intruded within or outside the silicic system (Muirhead et al., 2022), are applicable to our results. When a mafic intrusion occurs outside the silicic system but no eruptible silicic melt body in place, the intrusion will result in a change in the stress state around Taupō, unrest and faulting (Muirhead et al., 2022). Examples of this outcome potentially include the faulting and seismicity associated with the 1922 and 1983 swarms within the Taupō Fault Belt (Otway, 1986; Potter et al., 2015; Barker et al., 2021; Muirhead et al., 2022). Outcome 2, where a mafic intrusion occurs within the silicic system, was likened to the 2019 seismicity near Horomatangi Reefs beneath Lake Taupō (Illsley-Kemp et al., 2021; Muirhead et al., 2022). Based on these interpretations, the clear difference between a mafic intrusion within and outside the silicic system is the distribution of seismicity and change in the local stress state.

The extent of the silicic magma system is poorly constrained, ranging from 80 km^3 to upwards of 250 km^3 (Barker et al., 2021; Illsley-Kemp et al., 2021). These estimates limited by the aseismic nature of western Lake Taupō, where no seismicity occurred

during other periods of magmatic unrest, such as the 2008 and 2019 swarms (Fournier et al., 2013; Potter et al., 2015; Barker et al., 2021; Illsley-Kemp et al., 2021). The 2001 Taupō unrest also shows little similarity to 2019, which is a template for the expected outcome of a mafic intrusion into the silicic system (Muirhead et al., 2022). Based on the interpretations of Muirhead et al. (2022), it seems unlikely the intrusion beneath the Western Bay occurred within the silicic system.

The relocation results show similarities with outcome 5, in which a mafic intrusion occurs outside the silicic system (Muirhead et al., 2022). Seismic swarms in 1922 and 1983, which preceded seismometer coverage, both show evidence of deformation and faulting throughout the Taupō Fault Belt and even ruptured the Kaiapo Fault at the same location (Grindley, 1986; Peltier et al., 2009; Barker et al., 2021). This is more consistent with the distribution of seismicity in 2001. Mafic intrusions outside the silicic system can also interact with the tectonic system and force a change in the stress state (Rubin & Pollard, 1988; Rowland et al., 2010; Muirhead et al., 2022). This is consistent with the focal mechanism distribution in 2001, which infers a temporal rotation of σ^1 to horizontal (Figure 3.22). Such a stress change is unlikely to occur from an intrusion within the silicic system, as a system as large as Taupō's would buffer the stress impacts of the intrusion (Muirhead et al., 2022). We believe that the Western Bay intrusion that initiated seismicity during the 2001 swarm was of mafic origin and occurred outside the silicic system. This is consistent with both the distribution of earthquakes within the fault belt, the change in local stress state and the location of the Western Bay earthquake cluster in a previously aseismic area.

If we are correct in suggesting this intrusion occurred outside the silicic magma system, it may help constrain the westward extent of the silicic system. Considering the Western Bay intrusion likely occurred outside the silicic reservoir, this provides a potential limit on the reservoirs extent.

4.3.2 Magma-tectonic hazards

Seismicity has occurred at Taupō on an approximately decadal-scale since the introduction of seismic monitoring stations in 1985 (Barker et al., 2021). Ground shaking reports and surface displacements suggest that during periods of seismicity, hundreds of $<$ M3 earthquakes can occur everyday (Hull & Grindley, 1984). This is corroborated by matched-filter detection, which detected 1825 earthquakes over 48 hours during our swarm. Furthermore, during swarms associated with the Taupō Fault Belt (1922 & 1983), deformation ranging from mm to m scales can occur (Grange, 1932; Hull &

Grindley, 1984; Otway, 1986; Peltier et al., 2009). The previously mentioned major faults within the Taupō Fault Belt have expected recurrence intervals of less than 2000 years and the frequency of damaging earthquakes is an order of magnitude higher at Taupō Volcanoes than eruptions (Villamor & Berryman, 2001; Villamor et al., 2015; Stirling et al., 2012; Muirhead et al., 2022). Given these conditions, it is clear that the main hazards at Taupō on short-term timescales are associated with earthquake seismicity.

Considering this, the 2001 swarm at Taupō presents a rare opportunity to study the affects of magmatic interactions with the Taupō Fault Belt through a hazard perspective. Although this swarm did not include any seismicity larger than M_L3, strong vertical deformation followed the swarm along the northern shore of Lake Taupō (up to 0.2m yr^{-1}) (Peltier et al., 2009). This indicates the power of the interaction between the deeper mafic magmatic system and the regional tectonic system around Taupō, implying a larger intrusion could produce higher magnitude earthquakes. This is consistent with the potential for Taupō Rift faults to produce magnitudes in excess of M_L6, indicated by earthquakes sourced from the Kaingaroa and Edgecumbe faults in 1985 and 1987 (Grapes et al., 1987; Beanland et al., 1990; Villamor & Berryman, 2001; Barker et al., 2021).

Multiple clusters were relocated adjacent to the Whangamata Fault and in close proximity to the township of Kinloch on the northwestern lake shore. Should similar clustering occur again with higher magnitude earthquakes, there could be some significant ground-shaking or deformation impacts on Kinloch and potentially on Taupō township further southeast. In addition to the potential damage to residential areas, there is significant geothermal and hydrological infrastructure around Taupō. During the 2019 seismic swarm, shaking caused the rupturing of a major sewer pipe in Taupō township (Illsley-Kemp et al., 2021), an indication of how shaking can impact local infrastructure. Given there are four geothermal and hydro-power stations within the spread of earthquakes from the relocated 2001 swarm, assessing the hazards posed by the interaction between the Western Bay intrusion and the local tectonic system is critical.

4.4 Conclusions

Based on the results of earthquake relocation and focal mechanism calculation, we suggest that the earthquake swarm which occurred in the Taupō Fault Belt in 2001

was driven by the intrusion of a magmatic body. The intrusion is outlined by a large elliptical cluster of low-magnitude earthquakes occurring beneath Lake Taupō's Western Bay, a historically aseismic area. This conclusion is supported by the dominance of strike-slip focal mechanisms within the Taupō Fault Belt, consistent with a temporal rotation of the maximum compressive stress axes (σ^1) from subvertical to subhorizontal. This is due to increasing horizontal pressure applied by the intrusion, supported by evidence from similar scenarios at Campi Flegrei and the Main Ethiopian Rift. Though we may have expected to see uplift in this region accompanying the intrusion, the overlying lake can mask uplift signals of significantly larger intrusions than ours. Therefore we believe there is strong earthquake location and focal mechanism evidence for the presence of a magmatic intrusion beneath Lake Taupō's Western Bay.

The spatial and temporal distributions of seismicity within the Taupō Fault Belt also support this conclusion. The high rates of seismicity are consistent with fluid based origins, likely exsolved from the intruding source (Dzurisin et al., 1994, 2012; Waite & Smith, 2002; Russo et al., 2020). Furthermore, the majority of Taupō Fault Belt seismicity occurred after the initiation of the Western Bay cluster, consistent with the intrusion driving seismicity here. The temporal distribution of relocated events also suggests the Kaiapo Fault may be acting as a barrier to fluid propagation, supporting previous claims that it acts as a strong structural control within the Taupō Fault Belt. Similar effects from faults were seen in the nearby Rotokawa geothermal field, indicating this is not uncommon in the Taupō Volcanic Zone.

Taupō Fault Belt earthquakes primarily occurred in vertical clusters, aligned with small rift related fault planes and show signs of both fluid propagation and stress-induced faulting. This mirrors swarm seismicity distributions seen at Yellowstone in 2010, which was induced by exsolved fluids source from an inflating sill beneath the caldera. Hence the spatial earthquake distribution also supports an magmatic intrusion as the seismicity source.

We further conclude that these results indicate the 2001 swarm is an example of a mafic intrusion occurring outside the shallow silicic system at Taupō. The 2001 swarm displays similar distribution characteristics to previous swarms induced via this mechanism. Additionally, a change in stress state appears to be a key identifier and is reflected in our focal mechanism data, which is consistent with a horizontally rotated σ^1 axis during the time of intrusion. If a mafic intrusion did occur outside the silicic system, then the Western Bay cluster may indicate an outer limit of the silicic system. This is a primitive constraint, but could be used to inform more direct studies on the extent of the shallow magma system.

We recommend additional research be undertaken on the seismic nature of Taupō's Western Bay. These results suggest the area is not as aseismic as previously thought and likely had a major role in inducing nearly 4000 earthquakes over six months in 2001. Deformation relating to this intrusion was masked by the overlying lake, although more comprehensive modern monitoring of the area should help mitigate this from reoccurring. Despite low magnitude earthquakes within the Western Bay cluster, earthquakes $> M_L 2.5$ occurred within the Taupō Fault Belt. Considering the close proximity of both Kinloch and Taupō town to the Taupō Fault Belt and the potential of faults within it to produce $M_L 6$ earthquakes, further understanding this relationship is critical to hazard assessment at Taupō. Finally, if the Western Bay cluster has occurred outside the silicic system as inferred, this could provide a key constraint on the extent of the modern silicic system. This has been the focus of many geophysical studies and we hope this research can be used to further inform this topic.

Bibliography

Acocella, V., Di Lorenzo, R., Newhall, C., & Scandone, R. (2015). An overview of recent (1988 to 2014) caldera unrest: Knowledge and perspectives. *Reviews of Geophysics*, *53*(3), 896–955.

Addison, S., Azwar, L., Clearwater, J., Hernandez, D., Mountain, B., Blair, A., & Siratovich, P. (2017). Improving the Conceptual Understanding Through a Recent Injection of 200 GBq of Iodine-125 at the Rotokawa Geothermal Field, New Zealand. In *42nd Workshop on Geothermal Reservoir Engineering.*

Allan, A. S. R., Barker, S. J., Millet, M.-A., Morgan, D. J., Rooyakkers, S. M., Schipper, C. I., & Wilson, C. J. N. (2017). A cascade of magmatic events during the assembly and eruption of a super-sized magma body. *Contributions to Mineralogy and Petrology*, *172*(7), 1–34.

Allan, A. S. R., Morgan, D. J., Wilson, C. J. N., & Millet, M.-A. (2013). From mush to eruption in centuries: assembly of the super-sized Oruanui magma body. *Contributions to Mineralogy and Petrology*, *166*(1), 143–164.

Allan, A. S. R., Wilson, C. J. N., Millet, M.-A., & Wysoczanski, R. J. (2012). The invisible hand: Tectonic triggering and modulation of a rhyolitic supereruption. *Geology*, *40*(6), 563–566.

Anderson, E. M. (1905). The dynamics of faulting. *Transactions of the Edinburgh Geological Society*, *8*(3), 387–402.

Anderson, E. M. (1951). The dynamics of faulting and dyke formation with applications to Britain: Edinburgh. *Oliver and Boyd*, *206*.

Arnold, R., & Townend, J. (2007). A Bayesian approach to estimating tectonic stress from seismological data. *Geophysical Journal International*, *170*(3), 1336–1356.

Astiz, L., & Shearer, P. M. (2000). Earthquake locations in the inner Continental Borderland, offshore southern California. *Bulletin of the Seismological Society of America*, *90*(2), 425–449.

Avni, Y., Segev, A., & Ginat, H. (2012). Oligocene regional denudation of the northern Afar dome: Pre-and syn-breakup stages of the Afro-Arabian plate. *Geological Society of America Bulletin*, *124*(11-12), 1871–1897.

Ayele, A., Jacques, E., Kassim, M., Kidane, T., Omar, A., Tait, S., ... King, G. (2007). The volcano–seismic crisis in Afar, Ethiopia, starting September 2005. *Earth and Planetary Science Letters*, *255*(1-2), 177–187.

Bachmann, C. E., Wiemer, S., Goertz-Allmann, B. P., & Woessner, J. (2012). Influence of pore-pressure on the event-size distribution of induced earthquakes. *Geophysical Research Letters*, *39*(9).

Bachmann, O., & Huber, C. (2016). Silicic magma reservoirs in the Earth's crust. *American Mineralogist*, *101*(11), 2377–2404.

Baer, G., Hamiel, Y., Shamir, G., & Nof, R. (2008). Evolution of a magma-driven earthquake swarm and triggering of the nearby Oldoinyo Lengai eruption, as resolved by InSAR, ground observations and elastic modeling, East African Rift, 2007. *Earth and Planetary Science Letters*, *272*(1-2), 339–352.

Bain, A. A., Jellinek, A. M., & Wiebe, R. A. (2013). Quantitative field constraints on the dynamics of silicic magma chamber rejuvenation and overturn. *Contributions to Mineralogy and Petrology*, *165*(6), 1275–1294.

Bannister, S. (1992). Seismic exploration in geothermal areas—effect of the surface layer. In *Proceedings of the 14th New Zealand geothermal workshop* (pp. 231–235).

Bannister, S., Sherburn, S., & Bourguignon, S. (2016). Earthquake swarm activity highlights crustal faulting associated with the Waimangu–Rotomahana–Mt Tarawera geothermal field, Taupo Volcanic Zone. *Journal of Volcanology and Geothermal Research*, *314*, 49–56.

Barker, S. J., Rowe, M. C., Wilson, C. J. N., Gamble, J. A., Rooyakkers, S. M., Wysoczanski, R. J., ... Kenworthy, C. C. (2020). What lies beneath? Reconstructing the primitive magmas fueling voluminous silicic volcanism using olivine-hosted melt inclusions. *Geology*, *48*(5), 504–508.

Barker, S. J., Wilson, C. J. N., Allan, A. S. R., & Schipper, C. I. (2015). Fine-scale temporal recovery, reconstruction and evolution of a post-supereruption magmatic system. *Contributions to Mineralogy and Petrology*, *170*(1), 1–40.

Barker, S. J., Wilson, C. J. N., Illsley-Kemp, F., Leonard, G. S., Mestel, E. R. H., Mauriohooho, K., & Charlier, B. L. A. (2021). Taupō: an overview of New Zealand's youngest supervolcano. *New Zealand Journal of Geology and Geophysics*, *64*(2-3), 320–346.

Barker, S. J., Wilson, C. J. N., Morgan, D. J., & Rowland, J. V. (2016). Rapid priming, accumulation, and recharge of magma driving recent eruptions at a hyperactive caldera volcano. *Geology*, *44*(4), 323–326.

Barker, S. J., Wilson, C. J. N., Smith, E. G. C., Charlier, B. L. A., Wooden, J. L., Hiess, J., & Ireland, T. R. (2014). Post-supereruption magmatic reconstruction of Taupo volcano (New Zealand), as reflected in zircon ages and trace elements. *Journal of Petrology*, *55*(8), 1511–1533.

Bayes, T. (1763). An essay towards solving a problem in the doctrine of chances. By the late Rev. Mr. Bayes, FRS communicated by Mr. Price, in a letter to John Canton, AMFR S. *Philosophical transactions of the Royal Society of London*(53), 370–418.

Beanland, S., Blick, G. H., & Darby, D. J. (1990). Normal faulting in a back arc basin: geological and geodetic characteristics of the 1987 Edgecumbe earthquake, New Zealand. *Journal of Geophysical Research: Solid Earth*, *95*(B4), 4693–4707.

Belachew, M., Ebinger, C., Coté, D., Keir, D., Rowland, J. V., Hammond, J. O. S., & Ayele, A. (2011). Comparison of dike intrusions in an incipient seafloor-spreading segment in Afar, Ethiopia: Seismicity perspectives. *Journal of Geophysical Research: Solid Earth*, *116*(B6).

Berryman, K. (1992). A stratigraphic age of Rotoehu Ash and late Pleistocene climate interpretation based on marine terrace chronology, Mahia Peninsula, North Island, New Zealand. *New Zealand Journal of Geology and Geophysics*, *35*(1), 1–7.

Beyreuther, M., Barsch, R., Krischer, L., Megies, T., Behr, Y., & Wassermann, J. (2010). ObsPy: A python toolbox for seismology, a data center perspective. In *EGU General Assembly Conference Abstracts* (p. 4576).

Bibby, H. M., Caldwell, T. G., Davey, F. J., & Webb, T. H. (1995). Geophysical evidence on the structure of the Taupo Volcanic Zone and its hydrothermal circulation. *Journal of Volcanology and Geothermal Research*, *68*(1-3), 29–58.

Biggs, J., Bastow, I. D., Keir, D., & Lewi, E. (2011). Pulses of deformation reveal frequently recurring shallow magmatic activity beneath the Main Ethiopian Rift. *Geochemistry, Geophysics, Geosystems*, *12*(9).

Bonafede, M., & Olivieri, M. (1995). Displacement and gravity anomaly produced by a shallow vertical dyke in a cohesionless medium. *Geophysical Journal International*, *123*(3), 639–652.

Bosworth, W., & McClay, K. (2001). Structural and stratigraphic evolution of the Gulf of Suez rift, Egypt: a synthesis. *Mémoires du Muséum national d'histoire naturelle (1993)*, *186*, 567–606.

Briggs, R. M., Houghton, B. F., McWilliams, M., & Wilson, C. J. N. (2005). 40Ar/39Ar ages of silicic volcanic rocks in the Tauranga-Kaimai area, New Zealand: Dating the transition between volcanism in the Coromandel Arc and the Taupo Volcanic Zone. *New Zealand Journal of Geology and Geophysics*, *48*(3), 459–469.

Buck, W. R. (2004). Consequences of Asthenospheric Variability on Continental Rifting. In *Rheology and Deformation of the Lithosphere at Continental Margins* (pp. 1–30). Columbia University Press.

Buck, W. R., Einarsson, P., & Brandsdóttir, B. (2006). The influence of magma chamber properties and tectonic stress on dike propagation at divergent plate boundaries:

constraints from the 1974-1989 Krafla volcanic-tectonic episode. *Journal of Geophysical Research: Solid Earth*, *111*.

Bursik, M., Renshaw, C., McCalpin, J., & Berry, M. (2003). A volcanotectonic cascade: Activation of range front faulting and eruptions by dike intrusion, Mono Basin-Long Valley Caldera, California. *Journal of Geophysical Research: Solid Earth*, *108*(B8).

Carletti, F., & Gasperini, P. (2003). Lateral variations of seismic intensity attenuation in Italy. *Geophysical Journal International*, *155*(3), 839–856.

Cassidy, J., Ingham, M., Locke, C. A., & Bibby, H. (2009). Subsurface structure across the axis of the Tongariro Volcanic Centre, New Zealand. *Journal of Volcanology and Geothermal Research*, *179*(3-4), 233–240.

Chambefort, I., Lewis, B., Wilson, C. J. N., Rae, A. J., Coutts, C., Bignall, G., & Ireland, T. R. (2014). Stratigraphy and structure of the Ngatamariki geothermal system from new zircon U–Pb geochronology: Implications for Taupo Volcanic Zone evolution. *Journal of Volcanology and Geothermal Research*, *274*, 51–70.

Chamberlain, C. J., Hopp, C. J., Boese, C. M., Warren-Smith, E., Chambers, D., Chu, S. X., ... Townend, J. (2018). EQcorrscan: Repeating and near-repeating earthquake detection and analysis in Python. *Seismological Research Letters*, *89*(1), 173–181.

Chapman, C., & Leaney, W. (2012). A new moment-tensor decomposition for seismic events in anisotropic media. *Geophysical Journal International*, *188*(1), 343–370.

Charlier, B. L. A., Wilson, C. J. N., Lowenstern, J. B., Blake, S., Van Calsteren, P. W., & Davidson, J. P. (2005). Magma generation at a large, hyperactive silicic volcano (Taupo, New Zealand) revealed by U–Th and U–Pb systematics in zircons. *Journal of Petrology*, *46*(1), 3–32.

Charlier, B. L. A., Wilson, C. J. N., & Mortimer, N. (2010). Evidence from zircon U-Pb age spectra for crustal structure and felsic magma genesis at Taupo volcano, New Zealand. *Geology*, *38*(10), 915–918.

Charlton, D., Kilburn, C., & Edwards, S. (2020). Volcanic unrest scenarios and impact assessment at Campi Flegrei caldera, Southern Italy. *Journal of Applied Volcanology*, *9*(1), 1–26.

Christiansen, R. L. (2001). *The quaternary and pliocene Yellowstone Plateau volcanic field of Wyoming, Idaho, and Montana* (Vol. 729). US Department of the Interior, US Geological Survey.

Clarke, J., Adam, L., Sarout, J., van Wijk, K., Kennedy, B., & Dautriat, J. (2019). The relation between viscosity and acoustic emissions as a laboratory analogue for volcano seismicity. *Geology*, *47*(6), 499–503.

Cole, J. W., & Lewis, K. B. (1981). Evolution of the Taupo-Hikurangi subduction system. *Tectonophysics*, *72*(1-2), 1–21.

Cole, J. W., Milner, D. M., & Spinks, K. D. (2005). Calderas and caldera structures: a review. *Earth-Science Reviews*, *69*(1-2), 1–26.

Cole, J. W., & Spinks, K. D. (2009). Caldera volcanism and rift structure in the Taupo Volcanic Zone, New Zealand. *Geological Society, London, Special Publications*, *327*(1), 9–29.

Cole, J. W., Thordarson, T., & Burt, R. M. (2000). Magma origin and evolution of White Island (Whakaari) volcano, Bay of plenty, New Zealand. *Journal of Petrology*, *41*(6), 867–895.

Corti, G., Bonini, M., Conticelli, S., Innocenti, F., Manetti, P., & Sokoutis, D. (2003). Analogue modelling of continental extension: a review focused on the relations between the patterns of deformation and the presence of magma. *Earth-Science Reviews*, *63*(3-4), 169–247.

Corti, G., Ranalli, G., Agostini, A., & Sokoutis, D. (2013). Inward migration of faulting during continental rifting: Effects of pre-existing lithospheric structure and extension rate. *Tectonophysics*, *594*, 137–148.

Costa, A., Gottsmann, J., Melnik, O., & Sparks, R. S. J. (2011). A stress-controlled mechanism for the intensity of very large magnitude explosive eruptions. *Earth and Planetary Science Letters*, *310*(1-2), 161–166.

Cox, S. F. (2005). Coupling between deformation, fluid pressures, and fluid flow in ore-producing hydrothermal systems at depth in the crust. *Economic Geology*, *100th Anniversary Volume*, 39–75.

Darby, D. J., Hodgkinson, K. M., & Blick, G. H. (2000). Geodetic measurement of deformation in the Taupo Volcanic Zone, New Zealand: the north Taupo network revisited. *New Zealand Journal of Geology and Geophysics*, *43*(2), 157–170.

D'Auria, L., Massa, B., Cristiano, E., Del Gaudio, C., Giudicepietro, F., Ricciardi, G., & Ricco, C. (2015). Retrieving the stress field within the Campi Flegrei caldera (Southern Italy) through an integrated geodetical and seismological approach. *Pure and Applied Geophysics*, *172*(11), 3247–3263.

Davis, M., Koenders, M. A., & Petford, N. (2007). Vibro-agitation of chambered magma. *Journal of Volcanology and Geothermal Research*, *167*(1-4), 24–36.

Davy, B. W., & Caldwell, T. G. (1998). Gravity, magnetic and seismic surveys of the caldera complex, Lake Taupo, North Island, New Zealand. *Journal of Volcanology and Geothermal Research*, *81*(1-2), 69–89.

Anderson, J. A., & Wood, H. O. (1925). Description and theory of the torsion seismometer. *Bulletin of the Seismological Society of America*, *15*(1), 1–72.

Fournier, R. O. (1999). Hydrothermal processes related to movement of fluid from plastic into brittle rock in the magmatic-epithermal environment. *Economic Geology*, *94*(8), 1193–1211.

Potter, S. H., Scott, B. J., Jolly, G. E., Johnston, D. M., & Neall, V. E. (2015). A catalogue of caldera unrest at Taupo Volcanic Centre, New Zealand, using the volcanic unrest index (VUI). *Bulletin of Volcanology*, *77*(77), 1–28.

Seebeck, H., Nicol, A., Villamor, P., Ristau, J., & Pettinga, J. (2014). Structure and kinematics of the Taupo Rift, New Zealand. *Tectonics*, *33*(6), 1178–1199.

Doser, D. I. (1985). Source parameters and faulting processes of the 1959 Hebgen Lake, Montana, earthquake sequence. *Journal of Geophysical Research: Solid Earth*, *90*(B6), 4537–4555.

Downs, D. T., Rowland, J. V., Wilson, C. J. N., Rosenberg, M. D., Leonard, G. S., & Calvert, A. T. (2014). Evolution of the intra-arc Taupo-Reporoa basin within the Taupo Volcanic Zone of New Zealand. *Geosphere*, *10*(1), 185–206.

Dowrick, D. (2007). Effects of attenuation in the Taupo Volcanic Zone on patterns of spatial distribution of ground shaking in New Zealand earthquakes. *New Zealand Journal of Geology and Geophysics*, *50*(4), 315–325.

Dunbar, N. W., Kyle, P. R., & Wilson, C. J. N. (1989). Evidence for limited zonation in silicic magma systems, Taupo Volcanic Zone, New Zealand. *Geology*, *17*(3), 234–236.

Duputel, Z., Rivera, L., Kanamori, H., & Hayes, G. (2012). W phase source inversion for moderate to large earthquakes (1990–2010). *Geophysical Journal International*, *189*(2), 1125–1147.

Dzurisin, D., Wicks, C. W., & Poland, M. P. (2012). History of surface displacements at the Yellowstone Caldera, Wyoming, from leveling surveys and InSAR observations, 1923–2008. *US Geological Survey professional paper*, *1*, 68.

Dzurisin, D., Yamashita, K. M., & Kleinman, J. W. (1994). Mechanisms of crustal uplift and subsidence at the Yellowstone caldera, Wyoming. *Bulletin of Volcanology*, *56*(4), 261–270.

Eberhart-Phillips, D., Bannister, S., & Reyners, M. (2020). Attenuation in the mantle wedge beneath super-volcanoes of the Taupo Volcanic Zone, New Zealand. *Geophysical Journal International*, *220*(1), 703–723.

Eddington, P. K., Smith, R. B., & Renggli, C. (1986). *A study of tectonic activity in the Basin-Range Province and on the San Andreas Fault. No. 1: Kinematics of Basin-Range intraplate extension* (Tech. Rep.).

Eiby, G. A. (1966). Earthquake swarms and volcanism in New Zealand. *Bulletin Volcanologique*, *29*(1), 61–73.

Ellis, S., Heise, W., Kissling, W., Villamor, P., & Schreurs, G. (2014). The effect of crustal melt on rift dynamics: case study of the Taupo Volcanic Zone. *New Zealand Journal of Geology and Geophysics*, *57*(4), 453–458.

Ellis, S., Wilson, C. J. N., Bannister, S., Bibby, H. M., Heise, W., Wallace, L., & Patterson, N. (2007). A future magma inflation event under the rhyolitic Taupo volcano, New Zealand: Numerical models based on constraints from geochemical, geological, and geophysical data. *Journal of Volcanology and Geothermal Research*, *168*(1-4), 1–27.

Farrell, J., Husen, S., & Smith, R. B. (2009). Earthquake swarm and b-value characterization of the Yellowstone volcano-tectonic system. *Journal of Volcanology and Geothermal Research*, *188*(1-3), 260–276.

Fournier, N., Williams, C. A., Wallace, L., Sherburn, S., Jolly, A. D., Chardot, L., ... others (2013). From subduction processes to volcanic unrest: unraveling domino effects at Lake Taupo caldera, New Zealand. In *American Geophysical Union Fall Meeting Abstracts* (Vol. 2013, pp. V44C–01).

Froggatt, P. C. (1981). Stratigraphy and nature of Taupo Pumice formation. *New Zealand Journal of Geology and Geophysics*, *24*(2), 231–248.

Geller, R. J., & Mueller, C. S. (1980). Four similar earthquakes in central California. *Geophysical Research Letters*, *7*(10), 821–824.

Geshi, N., Kusumoto, S., & Gudmundsson, A. (2012). Effects of mechanical layering of host rocks on dike growth and arrest. *Journal of Volcanology and Geothermal Research*, *223*, 74–82.

Gibbons, S. J., & Ringdal, F. (2006). The detection of low magnitude seismic events using array-based waveform correlation. *Geophysical Journal International*, *165*(1), 149–166.

Gíslason, G., Eysteinsson, H., Björnsson, G., & Harðardóttir, V. (2015). Results of surface exploration in the Corbetti Geothermal Area, Ethiopia. In *World Geothermal Congress, Melbourne, Australia* (pp. 19–25).

Grange, L. I. (1932). Taupo earthquakes, 1922. Rents and Faults formed during earthquake of 1922 in Taupo District. *New Zealand Journal of Science and Technology*, *3*, 139–141.

Grapes, R. H., Sissons, B. A., & Wellman, H. W. (1987). Widening of the Taupo volcanic zone, New Zealand, and the Edgecumbe earthquake of March 1987. *Geology*, *15*(12), 1123–1125.

Gravley, D. M., Wilson, C. J. N., Rosenberg, M. D., & Leonard, G. S. (2006). The nature and age of Ohakuri Formation and Ohakuri Group rocks in surface exposures and geothermal drillhole sequences in the central Taupo Volcanic Zone, New Zealand. *New Zealand Journal of Geology and Geophysics*, *49*(3), 305–308.

Grindley, G. W. (1986). Historical Taupo earthquakes and earth deformation. *Royal Society of New Zealand Bulletin*, *24*, 173–186.

Gudmundsson, A. (2011). Deflection of dykes into sills at discontinuities and magma-chamber formation. *Tectonophysics*, *500*(1-4), 50–64.

Hainzl, S. (2004). Seismicity patterns of earthquake swarms due to fluid intrusion and stress triggering. *Geophysical Journal International*, *159*(3), 1090–1096.

Hainzl, S., & Ogata, Y. (2005). Detecting fluid signals in seismicity data through statistical earthquake modeling. *Journal of Geophysical Research: Solid Earth*, *110*(B5).

Hardebeck, J. L., & Shearer, P. M. (2002). A new method for determining first-motion focal mechanisms. *Bulletin of the Seismological Society of America*, *92*(6), 2264–2276.

Hardebeck, J. L., & Shearer, P. M. (2003). Using S/P amplitude ratios to constrain the focal mechanisms of small earthquakes. *Bulletin of the Seismological Society of America*, *93*(6), 2434–2444.

Harrison, A., & White, R. S. (2006). Lithospheric structure of an active backarc basin: the Taupo Volcanic Zone, New Zealand. *Geophysical Journal International*, *167*(2), 968–990.

Hauksson, E., Yang, W., & Shearer, P. M. (2012). Waveform relocated earthquake catalog for southern California (1981 to June 2011). *Bulletin of the Seismological Society of America*, *102*(5), 2239–2244.

Hayes, G., Reyners, M., & Stuart, G. (2004). The Waiouru, New Zealand, earthquake swarm: persistent mid crustal activity near an active volcano. *Geophysical Research Letters*, *31*(19).

Healy, J. (1964). Stratigraphy and chronology of late Quaternary volcanic ash in Taupo, Rotorua and Gisborne districts. *New Zealand Geological Survey Bulletin*, *73*.

Heimann, S. (2011). *A robust method to estimate kinematic earthquake source parameters* (Unpublished doctoral dissertation). Staats-und Universitätsbibliothek Hamburg Carl von Ossietzky.

Heimann, S., Kriegerowski, M., Isken, M., Nooshiri, N., Steinberg, A., Sudhaus, H., ... Dahm, T. (2019). Pyrocko - a versatile software framework for seismology. In *Geophysical Research Abstracts* (Vol. 21).

Helffrich, G., Wookey, J., & Bastow, I. (2013). *The seismic analysis code: A primer and user's guide*. Cambridge University Press.

Henrys, S. A., & Hochstein, M. P. (1990). Geophysical structure of the Broadlandsohaaki geothermal field (New Zealand). *Geothermics*, *19*(2), 129–150.

Henrys, S. A., Reyners, M., & Bibby, H. (2003). Exploring the plate boundary structure of the North Island, New Zealand. *EOS: Transactions American Geophysical Union*, *84*(31), 289–295.

Hill, D. P., & Prejean, S. (2005). Magmatic unrest beneath Mammoth mountain, California. *Journal of Volcanology and Geothermal Research*, *146*(4), 257–283.

Hogg, A., Lowe, D. J., Palmer, J., Boswijk, G., & Ramsey, C. B. (2012). Revised calendar date for the Taupo eruption derived by 14C wiggle-matching using a New Zealand kauri 14C calibration data set. *The Holocene*, *22*(4), 439–449.

Hogg, A., Wilson, C. J. N., Lowe, D. J., Turney, C. S. M., White, P., Lorrey, A., ... Brown, J. (2019). Correspondence: The Taupo eruption occurred in 232±10 CE, and not later. *Non-peer reviewed preprint submitted to Nature Communications on 28 December 2018*.

Hopp, C., Sewell, S., Mroczek, S., Savage, M., & Townend, J. (2020). Seismic response to evolving injection at the Rotokawa geothermal field, New Zealand. *Geothermics*, *85*, 101750.

Houghton, B. F., Wilson, C. J. N., Lloyd, E. F., Gamble, J. A., & Kolelaar, B. P. (1987). A catalogue of basaltic deposits within the central Taupo Volcanic Zone. *New Zealand Geological Survey*(18), 95-101.

Houghton, B. F., Wilson, C. J. N., McWilliams, M. O., Lanphere, M. A., Weaver, S. D., Briggs, R. M., & Pringle, M. S. (1995). Chronology and dynamics of a large silicic magmatic system: Central Taupo Volcanic Zone, New Zealand. *Geology*, *23*(1), 13–16.

Hudson, J. A., Pearce, R. G., & Rogers, R. M. (1989). Source type plot for inversion of the moment tensor. *Journal of Geophysical Research: Solid Earth*, *94*(B1), 765–774.

Hull, A. G., & Grindley, G. W. (1984). Active faulting near Taupo. *EOS: Transactions American Geophysical Union*.

Hutton, L. K., & Boore, D. M. (1987). The ML scale in southern California. *Bulletin of the Seismological Society of America*, *77*(6), 2074–2094.

Illsley-Kemp, F., Barker, S. J., Wilson, C. J. N., Chamberlain, C. J., Hreinsdóttir, S., Ellis, S., ... Wadsworth, F. B. (2021). Volcanic unrest at Taupō volcano in 2019: Causes, mechanisms and implications. *Geochemistry, Geophysics, Geosystems*, *22*, e2021GC009803.

Illsley-Kemp, F., Keir, D., Bull, J. M., Ayele, A., Hammond, J. O. S., Kendall, J.-M., ... Goitom, B. (2017). Local earthquake magnitude scale and b-value for the Danakil region of northern Afar. *Bulletin of the Seismological Society of America*, *107*(2), 521–531.

Illsley-Kemp, F., Savage, M. K., Wilson, C. J. N., & Bannister, S. (2019). Mapping stress and structure from subducting slab to magmatic rift: crustal seismic anisotropy of the North Island, New Zealand. *Geochemistry, Geophysics, Geosystems*, *20*(11), 5038–5056.

Ingebritsen, S. E., & Appold, M. S. (2012). The physical hydrogeology of ore deposits. *Economic Geology*, *107*(4), 559–584.

Kanamori, H., & Jennings, P. C. (1978). Determination of local magnitude, ML, from strong-motion accelerograms. *Bulletin of the Seismological Society of America*, *68*(2), 471–485.

Keir, D., Ebinger, C. J., Stuart, G. W., Daly, E., & Ayele, A. (2006). Strain accommodation by magmatism and faulting as rifting proceeds to breakup: Seismicity of the northern Ethiopian rift. *Journal of Geophysical Research: Solid Earth*, *111*(B5).

Laplace, P.-S. d. (1812). *Théorie analytique des probabilités; Par M. le comte Laplace,....* Mme Ve Courcier, imprimeur-libraire pour les mathématiques et la marine ....

La Rocca, M., & Galluzzo, D. (2019). Focal mechanisms of recent seismicity at Campi Flegrei, Italy. *Journal of Volcanology and Geothermal Research*, *388*, 106687.

Latorre, D., Mirabella, F., Chiaraluce, L., Trippetta, F., & Lomax, A. (2016). Assessment of earthquake locations in 3-D deterministic velocity models: A case study from the Altotiberina Near Fault Observatory (Italy). *Journal of Geophysical Research: Solid Earth*, *121*(11), 8113–8135.

Lavayssière, A., Greenfield, T., Keir, D., Ayele, A., & Kendall, J.-M. (2019). Local seismicity near the actively deforming Corbetti volcano in the Main Ethiopian Rift. *Journal of Volcanology and Geothermal Research*, *381*, 227–237.

Leonard, G. S., Begg, J. G., & Wilson, C. J. N. (2010). *Geology of the Rotorua Area.* GNS Science.

Leonard, G. S., Cole, J. W., Nairn, I. A., & Self, S. (2002). Basalt triggering of the c. AD 1305 Kaharoa rhyolite eruption, Tarawera volcanic complex, New Zealand. *Journal of Volcanology and Geothermal Research*, *115*(3-4), 461–486.

Litchfield, N. J., Van Dissen, R. J., Sutherland, R., M, B. P., Cox, S. C., Norris, R., ... Clark, K. (2013). *A model of active faulting in New Zealand: fault zone parameter descriptions, GNS Science Report 2012/19.* GNS Science.

Lloyd, R., Biggs, J., Birhanu, Y., Wilks, M., Gottsmann, J., Kendall, J.-M., ... Eysteinsson, H. (2018). Sustained uplift at a continental rift caldera. *Journal of Geophysical Research: Solid Earth*, *123*(6), 5209–5226.

Lloyd, R., Biggs, J., Wilks, M., Nowacki, A., Kendall, J.-M., Ayele, A., ... Eysteinsson, H. (2018). Evidence for cross rift structural controls on deformation and seismicity at a continental rift caldera. *Earth and Planetary Science Letters*, *487*, 190–200.

Lomax, A., Virieux, J., Volant, P., & Berge-Thierry, C. (2000). Probabilistic earthquake location in 3D and layered models. In *Advances in Seismic Event Location* (pp. 101–134). Springer.

Manning, D. A. (1996). Middle-late Pleistocene tephrostratigraphy of the eastern Bay of Plenty, New Zealand. *Quaternary International*, *34*, 3–12.

Manville, V. (2002). Sedimentary and geomorphic responses to ignimbrite emplacement: readjustment of the Waikato River after the AD 181 Taupo eruption, New Zealand. *The Journal of Geology*, *110*(5), 519–541.

Manville, V., White, J. D. L., Houghton, B. F., & Wilson, C. J. N. (1999). Paleohydrology and sedimentology of a post–1.8 ka breakout flood from intracaldera Lake Taupo, North Island, New Zealand. *Geological Society of America Bulletin*, *111*(10), 1435–1447.

Manville, V., & Wilson, C. J. N. (2003). Interactions between volcanism, rifting and subsidence: implications of intracaldera palaeoshorelines at Taupo volcano, New Zealand. *Journal of the Geological Society*, *160*(1), 3–6.

Massin, F., Farrell, J., & Smith, R. B. (2013). Repeating earthquakes in the Yellowstone volcanic field: Implications for rupture dynamics, ground deformation, and migration in earthquake swarms. *Journal of Volcanology and Geothermal Research*, *257*, 159–173.

Massiot, C., McNamara, D. D., & Lewis, B. (2015). Processing and analysis of high temperature geothermal acoustic borehole image logs in the Taupo Volcanic Zone, New Zealand. *Geothermics*, *53*, 190–201.

Mastin, L. G., & Pollard, D. D. (1988). Surface deformation and shallow dike intrusion processes at Inyo Craters, Long Valley, California. *Journal of Geophysical Research: Solid Earth*, *93*(B11), 13221–13235.

McKenzie, D. P. (1969). The relation between fault plane solutions for earthquakes and the directions of the principal stresses. *Bulletin of the Seismological Society of America*, *59*(2), 591–601.

McNamara, D. D., Milicich, S. D., Massiot, C., Villamor, P., McLean, K., Sépulveda, F., & Ries, W. F. (2019). Tectonic controls on Taupo Volcanic Zone geothermal expression: insights from Te Mihi, Wairakei geothermal field. *Tectonics*, *38*(8), 3011–3033.

Milia, A., Torrente, M. M., Massa, B., & Iannace, P. (2013). Progressive changes in rifting directions in the Campania margin (Italy): new constrains for the Tyrrhenian Sea opening. *Global and Planetary Change*, *109*, 3–17.

Milicich, S. D., Wilson, C. J. N., Bignall, G., Pezaro, B., & Bardsley, C. (2013). Reconstructing the geological and structural history of an active geothermal field: A case study from New Zealand. *Journal of Volcanology and Geothermal Research*, *262*, 7–24.

Minson, S., Simons, M., & Beck, J. L. (2013). Bayesian inversion for finite fault earthquake source models I–Theory and algorithm. *Geophysical Journal International*, *194*(3), 1701–1726.

Mouslopoulou, V., Nicol, A., Walsh, J. J., Beetham, D., & Stagpoole, V. (2008). Quaternary temporal stability of a regional strike-slip and rift fault intersection. *Journal of Structural Geology*, *30*(4), 451–463.

Muirhead, J. D., Illsley-Kemp, F., Barker, S. J., Villamor, P., Wilson, C. J. N., Otway, P. M., ... Shalla, Y. (2022). Stretching, Shaking, Inflating: Volcanic-Tectonic Interactions at a Rifting Silicic Caldera. *Frontiers in Earth Science*, *10*(835841).

Myers, M. L., Wallace, P. J., & Wilson, C. J. N. (2019). Inferring magma ascent timescales and reconstructing conduit processes in explosive rhyolitic eruptions using diffusive losses of hydrogen from melt inclusions. *Journal of Volcanology and Geothermal Research*, *369*, 95–112.

Myers, M. L., Wallace, P. J., Wilson, C. J. N., Morter, B. K., & Swallow, E. J. (2016). Prolonged ascent and episodic venting of discrete magma batches at the onset of the Huckleberry Ridge supereruption, Yellowstone. *Earth and Planetary Science Letters*, *451*, 285–297.

Myers, M. L., Wallace, P. J., Wilson, C. J. N., Watkins, J. M., & Liu, Y. (2018). Ascent rates of rhyolitic magma at the onset of three caldera-forming eruptions. *American Mineralogist: Journal of Earth and Planetary Materials*, *103*(6), 952–965.

Nairn, I. A. (1972). Rotoehu Ash and the Rotoiti Breccia Formation, Taupo Volcanic Zone, New Zealand. *New Zealand Journal of Geology and Geophysics*, *15*(2), 251–261.

Nairn, I. A., Self, S., Cole, J. W., Leonard, G. S., & Scutter, C. (2001). Distribution, stratigraphy, and history of proximal deposits from the c. AD 1305 Kaharoa eruptive episode at Tarawera Volcano, New Zealand. *New Zealand Journal of Geology and Geophysics*, *44*(3), 467–484.

Otway, P. M. (1980). Taupo lake level survey. *New Zealand Volcanology Record*, *9*, 21–22.

Otway, P. M. (1986). Vertical deformation associated with the Taupo earthquake swarm, June 1983. *Royal Society of New Zealand Bulletin*, *24*, 187–200.

Otway, P. M. (1989). Vertical deformation monitoring by periodic water level observations, Lake Taupo, New Zealand. In *Volcanic Hazards* (pp. 561–574). Springer.

Otway, P. M., Blick, G. H., & Scott, B. J. (2002). Vertical deformation at Lake Taupo, New Zealand, from lake levelling surveys, 1979–99. *New Zealand Journal of Geology and Geophysics*, *45*(1), 121–132.

Otway, P. M., Grindley, G. W., & Hull, A. G. (1984). Earthquakes active fault displacement and associated vertical deformation near Lake Taupo, Taupo volcanic zone. *New Zealand Geotechnical Society*(110).

Otway, P. M., & Sherburn, S. (1994). Vertical deformation and shallow seismicity around Lake Taupo, New Zealand, 1985–90. *New Zealand Journal of Geology and Geophysics*, *37*(2), 195–200.

Parotidis, M., Rothert, E., & Shapiro, S. A. (2003). Pore-pressure diffusion: A possible triggering mechanism for the earthquake swarms 2000 in Vogtland/NW-Bohemia, central Europe. *Geophysical Research Letters*, *30*(20).

Parotidis, M., Shapiro, S. A., & Rothert, E. (2005). Evidence for triggering of the Vogtland swarms 2000 by pore pressure diffusion. *Journal of Geophysical Research: Solid Earth*, *110*(B5).

Parson, L. M., & Wright, I. C. (1996). The Lau-Havre-Taupo back-arc basin: A southward-propagating, multi-stage evolution from rifting to spreading. *Tectonophysics*, *263*(1-4), 1–22.

Peltier, A., Hurst, T., Scott, B., & Cayol, V. (2009). Structures involved in the vertical deformation at Lake Taupo (New Zealand) between 1979 and 2007: New insights from numerical modelling. *Journal of Volcanology and Geothermal Research*, *181*(3-4), 173–184.

Podvin, P., & Lecomte, I. (1991). Finite difference computation of traveltimes in very contrasted velocity models: a massively parallel approach and its associated tools. *Geophysical Journal International*, *105*(1), 271–284.

Pollard, D. D., & Holzhausen, G. (1979). On the mechanical interaction between a fluid-filled fracture and the Earth's surface. *Tectonophysics*, *53*(1-2), 27–57.

Potter, S. H., Jolly, G. E., Neall, V. E., Johnston, D. M., & Scott, B. J. (2014). Communicating the status of volcanic activity: revising New Zealand's volcanic alert level system. *Journal of Applied Volcanology*, *3*(1), 1–16.

Potter, S. H., Scott, B. J., Jolly, G. E., Neall, V. E., & Johnston, D. M. (2015). Introducing the Volcanic Unrest Index (VUI): a tool to quantify and communicate the intensity of volcanic unrest. *Bulletin of Volcanology*, *77*(78), 1–15.

Poupinet, G., Ellsworth, W. L., & Frechet, J. (1984). Monitoring velocity variations in the crust using earthquake doublets: An application to the Calaveras Fault, California. *Journal of Geophysical Research: Solid Earth*, *89*(B7), 5719–5731.

Pugh, D. J., & White, R. S. (2018). MTfit: A Bayesian approach to seismic moment tensor inversion. *Seismological Research Letters*, *89*(4), 1507–1513.

Pugh, D. J., White, R. S., & Christie, P. A. F. (2016). A Bayesian method for microseismic source inversion. *Geophysical Journal International*, *206*(2), 1009–1038.

Reasenberg, P. A. (1985). FPFIT, FPPLOT, and FPPAGE: Fortran computer programs for calculating and displaying earthquake fault-plane solutions. *US Geological Survey Open-File Representative*, 85–739.

Reyners, M., Eberhart-Phillips, D., & Stuart, G. (2007). The role of fluids in lower-crustal earthquakes near continental rifts. *Nature*, *446*(7139), 1075–1078.

Reyners, M., & Stuart, G. (2002). *The Central North Island Passive Seismic Experiment.* Institute of Geological & Nuclear Sciences.

Richter, C. F. (1935). An instrumental earthquake magnitude scale. *Bulletin of the Seismological Society of America*, *25*(1), 1–32.

Richter, C. F. (1958). *Elementary Seismology.* W.H. Freeman, San Francisco, 768.

Riedesel, M. A., & Jordan, T. H. (1989). Display and assessment of seismic moment tensors. *Bulletin of the Seismological Society of America*, *79*(1), 85–100.

Rowland, J. V., & Sibson, R. H. (2001). Extensional fault kinematics within the Taupo Volcanic Zone, New Zealand: Soft-linked segmentation of a continental rift system. *New Zealand Journal of Geology and Geophysics*, *44*(2), 271–283.

Rowland, J. V., Wilson, C. J. N., & Gravley, D. M. (2010). Spatial and temporal variations in magma-assisted rifting, Taupo Volcanic Zone, New Zealand. *Journal of Volcanology and Geothermal Research*, *190*(1-2), 89–108.

Rubin, A. M., Gillard, D., & Got, J.-L. (1999). Streaks of microearthquakes along creeping faults. *Nature*, *400*(6745), 635–641.

Rubin, A. M., & Pollard, D. D. (1988). Dike-induced faulting in rift zones of Iceland and Afar. *Geology*, *16*(5), 413–417.

Russo, E., Tibaldi, A., Waite, G. P., Bonali, F. L., Massin, F., & Farrell, J. (2020). Unraveling the complex deformation pattern at Yellowstone plateau through seismicity and fracture analysis. *Tectonophysics*, *778*, 228352.

Sable, J. E., Houghton, B. F., Wilson, C. J. N., & Carey, R. J. (2006). Complex proximal sedimentation from Plinian plumes: the example of Tarawera 1886. *Bulletin of Volcanology*, *69*(1), 89–103.

Saria, E., Calais, E., Stamps, D. S., Delvaux, D., & Hartnady, C. J. H. (2014). Present-day kinematics of the East African Rift. *Journal of Geophysical Research: Solid Earth*, *119*(4), 3584–3600.

Schlotterbeck, B. A., & Abers, G. A. (2001). Three-dimensional attenuation variations in southern California. *Journal of Geophysical Research: Solid Earth*, *106*(B12), 30719–30735.

Seebeck, H., & Nicol, A. (2009). Dike intrusion and displacement accumulation at the intersection of the Okataina Volcanic Centre and Paeroa Fault zone, Taupo Rift, New Zealand. *Tectonophysics*, *475*(3-4), 575–585.

Seebeck, H., Nicol, A., Giba, M., Pettinga, J., & Walsh, J. (2014). Geometry of the subducting Pacific plate since 20 Ma, Hikurangi margin, New Zealand. *Journal of the Geological Society*, *171*(1), 131–143.

Self, S. (1983). Large-scale phreatomagmatic silicic volcanism: a case study from New Zealand. *Journal of Volcanology and Geothermal Research*, *17*(1-4), 433–469.

Sewell, S. M., Addison, S. J., Hernandez, D., Azwar, L., & Barnes, M. L. (2015). Rotokawa conceptual model update 5 years after commissioning of the 138 MWe NAP plant. In *New Zealand Geothermal Workshop: 2015 Proceedings.*

Shane, P. A. R., & Froggatt, P. C. (1991). Glass chemistry, paleomagnetism, and correlation of middle Pleistocene tuffs in southern North Island, New Zealand, and Western Pacific. *New Zealand Journal of Geology and Geophysics*, *34*(2), 203–211.

Shapiro, S. A., Huenges, E., & Borm, G. (1997). Estimating the crust permeability from fluid-injection-induced seismic emission at the KTB site. *Geophysical Journal International*, *131*(2), F15–F18.

Shearer, P. M. (1997). Improving local earthquake locations using the L1 norm and waveform cross correlation: Application to the Whittier Narrows, California, aftershock sequence. *Journal of Geophysical Research: Solid Earth*, *102*(B4), 8269–8283.

Shearer, P. M. (2002). Parallel fault strands at 9-km depth resolved on the Imperial fault, southern California. *Geophysical Research Letters*, *29*(14), 19–1.

Shelly, D. R., Hill, D. P., Massin, F., Farrell, J., Smith, R. B., & Taira, T. (2013). A fluid-driven earthquake swarm on the margin of the Yellowstone caldera. *Journal of Geophysical Research: Solid Earth*, *118*(9), 4872–4886.

Sherburn, S. (1992a). Characteristics of earthquake sequences in the central volcanic region, New Zealand. *New Zealand Journal of Geology and Geophysics*, *35*(1), 57–68.

Sherburn, S. (1992b). Seismicity of the Lake Taupo region, New Zealand, 1985–90. *New Zealand Journal of Geology and Geophysics*, *35*(3), 331–335.

Sibson, R. H. (1990). Rupture nucleation on unfavorably oriented faults. *Bulletin of the Seismological Society of America*, *80*(6A), 1580–1604.

Sibson, R. H. (1996). Structural permeability of fluid-driven fault-fracture meshes. *Journal of Structural Geology*, *18*(8), 1031–1042.

Simakin, A. G., & Ghassemi, A. (2010). The role of magma chamber-fault interaction in caldera forming eruptions. *Bulletin of Volcanology*, *72*(1), 85–101.

Simpson, R. W. (1997). Quantifying Anderson's fault types. *Journal of Geophysical Research: Solid Earth*, *102*(B8), 17909–17919.

Sivia, D., & Skilling, J. (2006). *Data analysis: a Bayesian tutorial.* OUP Oxford.

Slinkard, M. E., Carr, D. B., & Young, C. J. (2013). Applying waveform correlation to three aftershock sequences. *Bulletin of the Seismological Society of America*, *103*(2A), 675–693.

Smith, R. B., & Arabasz, W. J. (1991). Seismicity of the intermountain seismic belt. *Geological Society of America Continent Scale Map (CSM).*

Smith, R. B., Jordan, M., Steinberger, B., Puskas, C. M., Farrell, J., Waite, G. P., ... O'Connell, R. (2009). Geodynamics of the Yellowstone hotspot and mantle plume: Seismic and GPS imaging, kinematics, and mantle flow. *Journal of Volcanology and Geothermal Research*, *188*(1-3), 26–56.

Snoke, J. A., Lee, W. H. K., Kanamori, H., Jennings, P., & Kisslinger, C. (2003). FOCMEC: Focal mechanism determinations. *International Handbook of Earthquake and Engineering Seismology*, *85*, 1629–1630.

Stagpoole, V., Miller, C., Caratori Tontini, F., Brakenrig, T., & Macdonald, N. (2021). A two million-year history of rifting and caldera volcanism imprinted in new gravity anomaly compilation of the Taupō Volcanic Zone, New Zealand. *New Zealand Journal of Geology and Geophysics*, *64*(2-3), 358–371.

Stamps, D. S., Saria, E., & Kreemer, C. (2018). A geodetic strain rate model for the East African Rift System. *Scientific Reports*, *8*(1), 1–9.

Stern, T. A., & Benson, A. (2011). Wide-angle seismic imaging beneath an andesitic arc: Central North Island, New Zealand. *Journal of Geophysical Research: Solid Earth*, *116*(B9).

Stern, T. A., Stratford, W. R., & Salmon, M. L. (2006). Subduction at a continental margin: kinematics and dynamics of the central North Island, New Zealand. *Reviews of Geophysics*, *44*, RG4002.

Stirling, M., McVerry, G., Gerstenberger, M., Litchfield, N., Van Dissen, R., Berryman, K., ... others (2012). National seismic hazard model for New Zealand: 2010 update. *Bulletin of the Seismological Society of America*, *102*(4), 1514–1542.

Sutton, A. N., Blake, S., & Wilson, C. J. N. (1995). An outline geochemistry of rhyolite eruptives from Taupō volcanic centre, New Zealand. *Journal of Volcanology and Geothermal Research*, *68*(1-3), 153–175.

Svartman Dias, A. E., Lavier, L. L., & Hayman, N. W. (2015). Conjugate rifted margins width and asymmetry: The interplay between lithospheric strength and thermomechanical processes. *Journal of Geophysical Research: Solid Earth*, *120*(12), 8672–8700.

Tape, W., & Tape, C. (2012). A geometric setting for moment tensors. *Geophysical Journal International*, *190*(1), 476–498.

Tarantola, A., Valette, B., et al. (1982). Inverse problems = quest for information. *Journal of Geophysics*, *50*(1), 159–170.

Thurber, C. H. (1983). Earthquake locations and three-dimensional crustal structure in the Coyote Lake area, central California. *Journal of Geophysical Research: Solid Earth*, *88*(B10), 8226–8236.

Thurber, C. H. (1992). Hypocenter-velocity structure coupling in local earthquake tomography. *Physics of the Earth and Planetary Interiors*, *75*(1-3), 55–62.

Thurber, C. H., & Eberhart-Phillips, D. (1999). Local earthquake tomography with flexible gridding. *Computers & Geosciences*, *25*(7), 809–818.

Townend, J., Abercrombie, R., & McGarr, A. (2006). What do faults feel? Observational constraints on the stresses acting on seismogenic faults. *Geophysical Monograph - American Geophysical Union*, *170*, 313.

Townend, J., Sherburn, S., Arnold, R., Boese, C., & Woods, L. (2012). Three-dimensional variations in present-day tectonic stress along the Australia–Pacific plate boundary in New Zealand. *Earth and Planetary Science Letters*, *353*, 47–59.

Trugman, D. T., & Shearer, P. M. (2017). GrowClust: A hierarchical clustering algorithm for relative earthquake relocation, with application to the Spanish Springs and Sheldon, Nevada, earthquake sequences. *Seismological Research Letters*, *88*(2A), 379–391.

Venegas, A. L. M. (2011). Building a 2-D velocity model with Vel2Grid using polygons. Puerto Rico Seismic Network. [Computer software manual].

Villamor, P., & Berryman, K. R. (2001). A late Quaternary extension rate in the Taupo Volcanic Zone, New Zealand, derived from fault slip data. *New Zealand Journal of Geology and Geophysics*, *44*(2), 243–269.

Villamor, P., & Berryman, K. R. (2006a). Evolution of the southern termination of the Taupo Rift, New Zealand. *New Zealand Journal of Geology and Geophysics*, *49*(1), 23–37.

Villamor, P., & Berryman, K. R. (2006b). Late Quaternary geometry and kinematics of faults at the southern termination of the Taupo Volcanic Zone, New Zealand. *New Zealand Journal of Geology and Geophysics*, *49*(1), 1–21.

Villamor, P., Berryman, K. R., Ellis, S. M., Schreurs, G., Wallace, L. M., Leonard, G. S., ... Ries, W. F. (2017). Rapid evolution of subduction-related continental intraarc rifts: The Taupo Rift, New Zealand. *Tectonics*, *36*(10), 2250–2272.

Villamor, P., Berryman, K. R., Nairn, I. A., Wilson, K., Litchfield, N., & Ries, W. (2011). Associations between volcanic eruptions from Okataina volcanic center and surface rupture of nearby active faults, Taupo rift, New Zealand: Insights into the nature of volcano-tectonic interactions. *Geology Society of America Bulletin*, *123*(7-8), 1383–1405.

Villamor, P., Clark, K., Watson, M., Rosenberg, M., Lukovic, B., Ries, W., ... others (2015). New Zealand geothermal power plants as critical facilities: an active fault avoidance study in the Wairakei Geothermal Field, New Zealand. In *World Geothermal Congress 2015.*

Vitale, S., & Isaia, R. (2014). Fractures and faults in volcanic rocks (Campi Flegrei, southern Italy): insight into volcano-tectonic processes. *International Journal of Earth Sciences*, *103*(3), 801–819.

Vucetich, C. G., & Howorth, R. (1976). Late Pleistocene tephrostratigraphy in the Taupo district, New Zealand. *New Zealand Journal of Geology and Geophysics*, *19*(1), 51–69.

Waite, G. P., & Smith, R. B. (2002). Seismic evidence for fluid migration accompanying subsidence of the Yellowstone caldera. *Journal of Geophysical Research: Solid Earth*, *107*(B9), ESE–1.

Waldhauser, F., & Ellsworth, W. L. (2000). A double-difference earthquake location algorithm: Method and application to the northern Hayward fault, California. *Bulletin of the Seismological Society of America*, *90*(6), 1353–1368.

Waldhauser, F., Ellsworth, W. L., & Cole, A. (1999). Slip-parallel seismic lineations on the northern Hayward fault, California. *Geophysical Research Letters*, *26*(23), 3525–3528.

Waldhauser, F., & Schaff, D. P. (2008). Large-scale relocation of two decades of Northern California seismicity using cross-correlation and double-difference methods. *Journal of Geophysical Research: Solid Earth*, *113*(B8).

Wallace, L. M., Beavan, J., McCaffrey, R., Berryman, K. R., & Denys, P. (2007). Balancing the plate motion budget in the South Island, New Zealand using GPS, geological and seismological data. *Geophysical Journal International*, *168*(1), 332–352.

Wallace, L. M., Beavan, J., McCaffrey, R., & Darby, D. (2004). Subduction zone coupling and tectonic block rotations in the North Island, New Zealand. *Journal of Geophysical Research: Solid Earth*, *109*(B12).

Wallis, I. C., Bardsley, C. J., Powell, T., Rowland, J. V., & O'Brien, J. M. (2013). A structural model for the Rotokawa geothermal field, New Zealand. In *35th New Zealand Geothermal Workshop: 2013 Proceedings* (pp. 17–20).

Wang, Y., Forsyth, D. W., & Savage, B. (2009). Convective upwelling in the mantle beneath the Gulf of California. *Nature*, *462*(7272), 499–501.

Warren-Smith, E., Chamberlain, C. J., Lamb, S., & Townend, J. (2017). High-precision analysis of an aftershock sequence using matched-filter detection: The 4 May 2015 ML 6 Wanaka earthquake, Southern Alps, New Zealand. *Seismological Research Letters*, *88*(4), 1065–1077.

Webb, T. H., Ferris, B. G., & Harris, J. S. (1986). The Lake Taupo, New Zealand, earthquake swarms of 1983. *New Zealand Journal of Geology and Geophysics*, *29*(4), 377–389.

Wibberley, C. A. J., Yielding, G., & Di Toro, G. (2008). Recent advances in the understanding of fault zone internal structure: a review. *Geological Society, London, Special Publications*, *299*(1), 5–33.

Wilson, C. J. N. (1985). The Taupo eruption, New Zealand. II. The Taupo ignimbrite. *Philosophical Transactions of the Royal Society of London. Series A, Mathematical and Physical Sciences*, *314*(1529), 229–310.

Wilson, C. J. N. (1993). Stratigraphy, chronology, styles and dynamics of late Quaternary eruptions from Taupo volcano, New Zealand. *Philosophical Transactions of the Royal Society of London. Series A: Physical and Engineering Sciences*, *343*(1668), 205–306.

Wilson, C. J. N., Blake, S., Charlier, B. L. A., & Sutton, A. N. (2006). The 26.5 ka Oruanui eruption, Taupo volcano, New Zealand: development, characteristics and evacuation of a large rhyolitic magma body. *Journal of Petrology*, *47*(1), 35–69.

Wilson, C. J. N., & Charlier, B. L. A. (2009). Rapid rates of magma generation at contemporaneous magma systems, Taupo Volcano, New Zealand: insights from U–Th model-age spectra in zircons. *Journal of Petrology*, *50*(5), 875–907.

Wilson, C. J. N., & Charlier, B. L. A. (2016). The life and times of silicic volcanic systems. *Elements*, *12*(2), 103–108.

Wilson, C. J. N., Gravley, D. M., Leonard, G. S., & Rowland, J. V. (2009). Volcanism in the central Taupo Volcanic Zone, New Zealand: tempo, styles and controls. *Studies in Volcanology: the legacy of George Walker. Special Publications of IAVCEI*, *2*, 225–247.

Wilson, C. J. N., Houghton, B. F., & Lloyd, E. F. (1986). Volcanic history and evolution of the Maroa-Taupo area, central North Island. *Late Cenozoic Volcanism in New Zealand*, *23*, 194–223.

Wilson, C. J. N., Houghton, B. F., McWilliams, M. O., Lanphere, M. A., Weaver, S. D., & Briggs, R. M. (1995). Volcanic and structural evolution of Taupo Volcanic Zone, New Zealand: a review. *Journal of Volcanology and Geothermal Research*, *68*(1-3), 1–28.

Wilson, C. J. N., Rogan, A. M., Smith, I. E. M., Northey, D. J., Nairn, I. A., & Houghton, B. F. (1984). Caldera volcanoes of the Taupo volcanic zone, New Zealand. *Journal of Geophysical Research: Solid Earth*, *89*(B10), 8463–8484.

Wilson, C. J. N., & Rowland, J. V. (2016). The volcanic, magmatic and tectonic setting of the Taupo Volcanic Zone, New Zealand, reviewed from a geothermal perspective. *Geothermics*, *59*, 168–187.

Wilson, C. J. N., & Walker, G. P. L. (1985). The Taupo eruption, New Zealand I. General aspects. *Philosophical Transactions of the Royal Society of London. Series A, Mathematical and Physical Sciences*, *314*(1529), 199–228.

Wolfenden, E., Ebinger, C., Yirgu, G., Renne, P. R., & Kelley, S. P. (2005). Evolution of a volcanic rifted margin: Southern Red Sea, Ethiopia. *Geological Society of America Bulletin*, *117*(7-8), 846–864.

Wright, I. C., & Ballance, P. F. (1993). Southern Havre Trough–Bay of Plenty (New Zealand): structure and seismic stratigraphy of an active back-arc basin complex. *South Pacific Sedimentary Basins*, *2*, 196–211.

Zoback, M. L. (1992). First and second-order patterns of stress in the lithosphere: The World Stress Map Project. *Journal of Geophysical Research: Solid Earth*, *97*(B8), 11703–11728.

Zollo, A., & Bernard, P. (1991). Fault mechanisms from near-source data: joint inversion of S polarizations and P polarities. *Geophysical Journal International*, *104*(3), 441–451.

Zwaan, F., Schreurs, G., Naliboff, J., & Buiter, S. J. (2016). Insights into the effects of oblique extension on continental rift interaction from 3D analogue and numerical models. *Tectonophysics*, *693*, 239–260.